Tractable Performance Analysis for Outdoor and Indoor 3D Small-cell Networks

Chen Chen

Department of Electronic and Electrical Engineering

University of Sheffield

Supervisors: Prof. Jie Zhang, Prof. Xiaoli Chu

This thesis is submitted for the approval of the

Doctor of Philosophy

April 2022

This thesis is dedicated to my beloved family. Without their unconditional love, encouragement and support, I would not be the person I am today.

Acknowledgements

First and foremost, I'd like to thank my supervisor Professor Jie Zhang for providing me with the opportunity to undertake this research. His enthusiasm and rigorous attitude towards academic research have inspired and encouraged me all the time during my Ph.D. studies. His experience and knowledge have guided my research direction and inspired me to create meaningful and impactful work. I'd like to thank also my co-supervisor Professor Xiaoli Chu for the guidance through this journey. Her detailed comments, continuous encouragement and unfailing patience have enlightened and shaped me to be an independent researcher.

I'd like to acknowledge the financial support from the European Union Horizon 2020 research and innovation program under the Marie Sklodowska-Curie grant agreement No. 766231 WAVE-COMBE H2020-MSCA-ITN-2017. The training and network opportunities provided by WAVE-COMBE project are important to my development as a researcher. I am deeply grateful to my supervisor Frederik Naessens during my virtual secondment with Televic Conference, and my supervisor Francisco Hurtado during my secondment at Axion in Spain, for sharing with me their experience in the industry. I'd like to extend my sincere thanks to all the members of WAVE-COMBE project for our discussions with regard to both academic research and daily life.

I'd like to express my gratitude to the collaborators of the work during my Ph.D. studies, Dr. Jiliang Zhang, Dr. Zitian Zhang, Yixin Zhang, Mengxin Zhou, Songjiang Yang, Yan Jiang, Yunbai Wang and Hui Zheng. Special thanks to Dr. Jiliang Zhang for his unwavering support and guidance during the past two years, and Dr. Zitian Zhang for his insightful comments and suggestions during our weekly discussions. I'd like to thank all the colleagues and friends in the Wireless Group of University of Sheffield for their help in many aspects of my Ph.D. life.

Above all, I'd like to express my gratitude to my parents for their unconditional love and support. I'd like to thank my girlfriend, Siyu Chen, for her long-term company, encouragement and love, which has brought me happiness and motivation. I'd like to thank all my family, teachers and friends. I would not be where I am today without them.

Abstract

In order to cope with the exponential growth in wireless capacity demands, network operators will deploy a large number of small cells to improve spatial spectrum reuse. Compared with conventional sparse cellular networks, small-cell networks (SCNs) have much shorter transmission links, and therefore the height difference between base stations (BSs) and users has a significant impact on the network performance with respect to coverage and capacity. However, most existing works have modelled SCNs on a two-dimensional plane, which may be highly inaccurate. Moreover, the coexisting of small cells and regular macrocells, and the application of emerging technologies such as large antenna arrays and millimeter wave (mmWave) communications have brought new research challenges in the deployment of small cells. To address these challenges, this thesis develops new tractable models using stochastic geometry for three three-dimensional (3D) SCN scenarios: 3D mmWave SCNs, 3D heterogeneous networks (HetNets) and indoor multi-storey SCNs.

Communication in mmWave spectrum is one key enabler to provide high data rates. In the first paper, we propose a 3D system model for outdoor mmWave SCNs, capturing the 3D nature of the deployment environment and characterizing antenna array gains in both elevation and azimuth dimensions. We analytically derive the downlink (DL) coverage probability and area spectral efficiency (ASE). Our results reveal that when other network parameters are fixed, the joint optimization of BS height and BS antenna downtilt can maximize the DL coverage probability and ASE.

In the second paper, we model and analyze an outdoor K-tier 3D HetNet where different tiers have potential different BS density, BS height, transmit power, number of antennas per BS, path loss exponent and cell association bias. Based on the proposed model, the expressions of

the DL ergodic rate, ASE and energy efficiency are derived under both the strongest received signal and the closest BS cell-association strategies. We observe that in an ultra-dense HetNet, under both cell-association strategies, SBSs should be deployed at the same height as users' antennas to achieve high ergodic rate, ASE and energy efficiency.

Finally, in the third paper, we develop an indoor multi-storey SCN model, incorporating the storey height and ceiling penetration loss. We analytically derive the DL coverage probability, spectral efficiency and ASE. Simulation results show that there exist certain values of storey height and BS density that degrade the DL coverage probability. The results can shed new insights into the deployment of indoor small cells and the design of a new multi-storey building from the perspective of enhancing indoor wireless coverage.

The analytical and numerical results presented in this thesis provide guidelines for the planning and deployment of 3D mmWave SCNs, 3D HetNets and indoor multi-storey SCNs, and the proposed analytical frameworks based on stochastic geometry can be extended to the modelling and analysis of other 3D cellular network scenarios.

Table of contents

List of Abbreviations

μWave microwave

2D two-dimensional

3D three-dimensional

3GPP 3rd Generation Partnership Project

5G fifth generation cellular networks

6G sixth generation cellular networks

AoD angles of departure

ASE area spectral efficiency

BPP binomial point process

BS base station

CoMP coordinated multipoint

D2D device-to-device

DL downlink

EE energy efficiency

HetNet heterogeneous network

IoT internet of things

IRS intelligent reflective surface

LOS line-of-sight

MAC medium access control

MBS macrocell BS

MIMO multiple-input-multiple-output

MISO multiple-input single-output

MLP Manhattan line processes

mmWave millimeter wave

NLOS non-line-of-sight

PDF probability density function

PGFL probability generating functional

PHCP Poisson hard-core process

QoS quality-of-service

ROP random object process

SBS small-cell BS

SCN small-cell network

SINR signal-to-interference-plus-noise-ratio

SIR signal-to-interference-ratio

SP Strauss process

TDD time-division duplex

UAV unmanned aerial vehicle

UL uplink

WLAN wireless local area network

WPAN wireless personal area network

Part I

Introduction and Overview

Chapter 1

Introduction

1.1 Background

1.1.1 Small-cell Networks

Based on recent predictions of Cisco [1], the number of global mobile subscribers will grow to 5.7 billion and the number of global mobile devices will grow to 13.1 billion by 2023. Along with the tremendous increase of connections, mobile data traffic demand is surging exponentially due to the emergence of data-hungry applications such as remote surgery, internet of things (IoT), virtual and augmented reality, and autonomous vehicles [2]. It is expected that the traffic demand will keep increasing at an annual rate of 47 percent by 2030 [3]. To accommodate this galloping demand for data traffic, a large quantity of small cells are required to be deployed to improve network capacity and save energy consumption. In accordance with [4], from 1950 to 2000, a 2700 $\times$ network capacity gain was achieved from network densification, while only 15 $\times$ gain from a larger bandwidth, 5 $\times$ gain from the medium access control (MAC) and modulation schemes, and 5 $\times$ gain through better coding techniques. From this data, we can see that the deployment of small-cells is the most promising approach towards the 1000 $\times$ increase of network throughput required by the fifth generation cellular networks (5G) and beyond. The current 5G network standardization efforts also suggest that small-cell deployment will remain the main driving force of cellular networks in the coming years [5].

1.1.2 Millimeter-wave Small-cell Networks

Millimeter wave (mmWave) communication has been regarded to be a promising solution to provide ultra-high data rates up to several Gbps owing to the large bandwidth of mmWave bands (from 30 GHz to 300 GHz) [6]. It has found wide applications in scenarios with short-range transmission and low mobility, such as wireless local area network (WLAN) and wireless personal area network (WPAN) [7]. Moreover, it can also be applied in scenarios with high mobility, such as cellular networks and industrial IoT scenarios. For instance, 3rd Generation Partnership Project (3GPP) has initiated 5G new radio standardization operating at mmWave frequency bands [8].

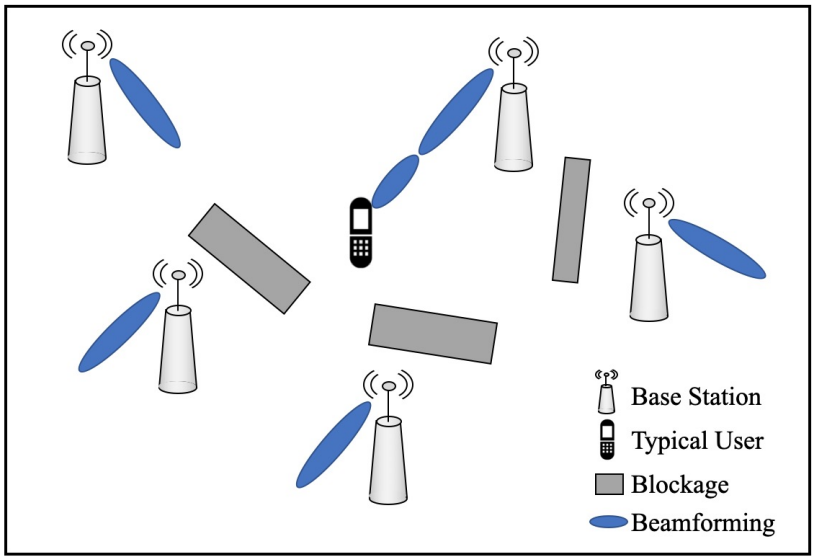

Fig. 1.1 An illustration of a typical mmWave SCN.

However, the deployment of mmWave base stations (BSs) requires new strategies that take into account the distinguished features of mmWave bands. In accordance with the channel measurements [9], mmWave frequency bands are vulnerable to high free space path loss and atmosphere absorption, and poor penetration through blockages such as walls, vehicles and pedestrians. One feasible solution is the deployment of small-cell network (SCN) which reduces the transmission distance between BSs and users, and increases the line-of-sight (LOS) probability of communication links [10]. Although the increase of BS density improves the spatial reuse, it may lead to excessive interference and deteriorate the performance of

the networks. Fortunately, the very short wavelength of mmWave enables the deployment of massive antenna arrays, which can be employed to generate directional beamforming to augment the received power and mitigate the inter-cell interference [11]. A typical mmWave SCN is shown in Fig. 1.1.

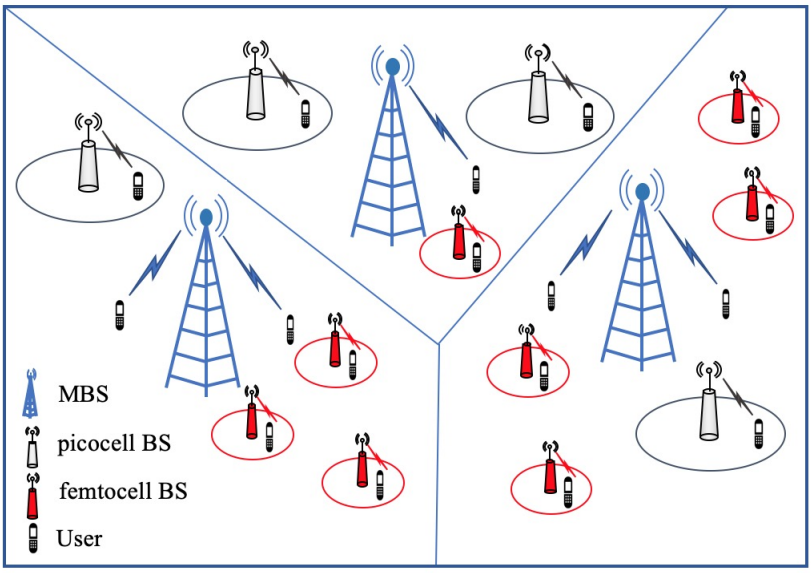

Fig. 1.2 An illustration of a typical HetNet.

1.1.3 Heterogeneous Networks

The deployment of small cells brings about the heterogeneity of cellular networks, inevitably. As shown in Fig. 1.2, a typical HetNet comprises the macrocells overlaid with small cells, where the macrocells provide an umbrella coverage for the users and the small cells contribute most of the capacity as well as complement the dead zones. The macrocell BSs (MBSs) and small-cell BSs (SBSs) may differ in transmit power, BS height and BS density, and the macrocell tier and small-cell tier may differ in cell association bias and path loss exponent. To be specific, MBSs provides a wide area coverage in range of few kilometers with a transmit power up to 46 dBm. Small cells feature BSs with a low transmit power and a small coverage area, e.g., picocells and femtocells [12]. Generally, picocells are deployed in indoor and outdoor hotspots, e.g., shopping malls, stadiums and airports, with a coverage area in range of 100 meters and a transmit power between 23 and 30 dBm; while femtocells are installed for

indoor coverage within tens of meters, with a transmit power no more than 23 dBm. Due to the diversity of BS types, the network performance of the HetNets with regard to coverage and capacity, may be different from the single-tier macrocell network or small-cell network [13], calling for a different SBS deployment strategy. Moreover, the per-tier association bias, which can control the offloading of users from the macrocells to small cells, needs to be designed for a better quality-of-service (QoS).

1.1.4 Indoor Small-cell Networks

In accordance with [14], approximately 80 percent of the data-traffic is generated indoors, indicating the importance of indoor wireless coverage. Nevertheless, outdoor-to-indoor communication suffers from high penetration losses through building walls. It is therefore anticipated that indoor mobile traffic demands are mainly served by indoor deployed small-cell network. Over the years, indoor small cells have largely been deployed for residential, and have been expanded to cover enterprise scenarios [5]. Conventionally, indoor small cells, e.g., femtocells, have been user-deployed following a "plug-and-play" way. However, the unplanned deployment may lead to severe inter-cell interference, as the number of small cells increases rapidly. In line of this, some studies have suggested a more centralized deployment by network operator to maximize the overall network performance [15]. Different from outdoor SCN deployment, when deploying indoor SCNs, the effects of blockages such as interior walls and ceilings need to be taken into account.

1.1.5 3D Small-cell Networks

For convenient deployment, SBSs are usually deployed on the walls, lampposts and trees abutting the street, with an height higher than the user height. However, most of the previous work has not considered the height difference between the SBSs and the users [16–19]. Recently, the authors in [20][21] have involved the height difference into their network model and found that there exists a limit of network densification: when the user density is sufficiently larger than the BS density, both the coverage and capacity degrade towards zero with the increase of BS

density, even if directional antennas are employed. This indicates that there exist densification limits for 3D SCNs and that it is important to incorporate the heights of BSs, users, or even blockages into the network modeling.

As far as we know, the systematical performance analysis of 3D mmWave SCNs, 3D HetNets and indoor multi-storey SCNs has not been carried out yet, which will be the main topics in the three papers presented in this thesis.

1.2 Motivation and Objectives

The previous work has largely modelled SCNs on a 2D plane, ignoring the heights of BSs and users, which may lead to inaccurate results of network performance analysis. The aim of the thesis is to model 3D SCNs and analytically derive tractable expressions of network performance metrics, e.g., coverage probability and spectral efficiency. The analytical results can provide insight into the deployment strategy of 3D SCNs. We focus on the following three application scenarios: 3D mmWave SCNs, 3D HetNets and indoor multi-storey SCNs. With the aforementioned aim, the following research questions are investigated:

Q1: How to model 3D SCNs and evaluate their network performance e.g., coverage probability and ASE, in a tractable way?

Q2: What are the crucial network parameters that mostly affect the performance of 3D SCNs?

Q3: How to optimize the crucial network parameters to enhance the network coverage and capacity in 3D SCNs?

Q4: What is the impact of network densification on the network coverage and capacity in 3D SCNs? Can network capacity gains always be obtained by network densification?

1.3 Contributions

1.3.1 Papers Included in the Thesis

Paper I: Performance Analysis for 3D Millimeter-wave Small-cell Networks, co-authored with M. Zhou, J. Zhang, X. Chu, F. Naessens and J. Zhang. This paper has been submitted to IEEE Transactions on Wireless Communications.

Paper II: On the Deployment of Small Cells in 3D Heterogeneous Networks, co-authored with J. Zhang, X. Chu and J. Zhang. This paper has been submitted to IEEE Transactions on Wireless Communications.

Paper III: On the Performance of Indoor Multi-Story Small-Cell Networks, co-authored with Y. Zhang, J. Zhang, X. Chu and J. Zhang. This paper has been published on IEEE Transactions on Wireless Communications, 2021.

1.3.2 Papers not Included in the Thesis

- C. Chen, S. Yang, J. Zhang, X. Chu and J. Zhang, "Tractable performance analysis of small-cell networks with a novel bounded path loss model," *Electron. Lett.*, vol. 56, no. 2, pp. 105-107, Jan. 2020.

- C. Chen, Y. Jiang, J. Zhang, X. Chu and J. Zhang, "Parameter optimization for energy efficient indoor massive MIMO small cell networks", *2020 IEEE 91st Vehicular Technology Conference (VTC2020-Spring)*, 2020, pp. 1-5.

- C. Chen, J. Zhang, X. Chu and J. Zhang, "On the optimal base-station height in small-cell networks considering blockage effects," *IEEE Trans. Veh. Technol.*, accepted as a correspondence with minor revisions.

- C. Chen, Z. Zhang, J. Zhang, X. Chu and J. Zhang, "Multi-agent deep reinforcement learning-based trajectory optimization for energy efficient UAV CoMP," under preparation for submitting to IEEE Transactions.

- Y. Zhang, C. Chen, S. Yang, J. Zhang, X. Chu and J. Zhang, "How friendly are building materials as reflectors to indoor LOS MIMO communications?," *IEEE Internet Things J.,* vol. 7, no. 9, pp. 9116-9127, Sept. 2020.

- Y. Wang, H. Zheng, C. Chen and X. Chu, "The effect of wall blockages on indoor small cell networks with LOS/NLOS user association strategies," *2021 IEEE 93rd Vehicular Technology Conference (VTC2021-Spring)*, 2021, pp. 1-6.

1.3.3 Contributions of the Thesis

The thesis models 3D SCNs and analyzes their network performance using stochastic geometry. In each paper, we address research questions Q1-Q4 for a specific 3D SCN scenario. The main contributions of this thesis are summarized as follows:

- In the first paper, we propose an outdoor 3D mmWave SCN model which characterizes the 3D BS antenna radiation pattern and the effects of blockages in 3D space. We consider different heights of BSs, users and blockages, and model the horizontal locations of mmWave BSs and blockages as two independent Poisson point processes (PPPs). We decompose the 3D antenna gain into the BS antenna downtilt gain and beamforming gain, and propose a simple exponential expression to approximate the BS antenna downtilt gain with a high level of accuracy. Based on the proposed model, we derive the 3D LOS probability and provide rigorous mathematical derivations of the DL coverage probability and ASE. Subsequently, we analyze the effects of BS antenna downtilt, BS height and BS density on the coverage and capacity, and shed novel insights into the actual deployment of mmWave small cells and the configuration of BS antenna parameters.

- In the second paper, we extend the single-tier 3D SCN model in the first paper to an outdoor K-tier 3D HetNet, taking into account potentially different BS density, BS height, number of antennas per BS, transmit power, path loss exponent and cell association bias for each tier. We derive the per-tier LOS probability and the expressions of the per-tier association probability, DL ergodic rate, ASE and energy efficiency under both the strongest received signal and the closest BS cell-association strategies. We focus on

sub-6GHz frequencies and adopt digital beamforming for multi-antenna transmission. The numerical results show the effects of SBS height, SBS density, number of antennas per BS and small-cell bias on various performance metrics, and can shed novel light on the actual small cell deployment and the optimal offloading strategy in a 3D HetNet.

- Finally, in the third paper, we turn our attention to indoor networks and develop a 3D SCN model for a multi-storey building where single-antenna BSs on each storey are distributed following a PPP and BSs on the same storey have the same height. This SCN can be considered as a special 3D HetNet where the transmission link from a user to each tier experiences a specific ceiling penetration loss. We analytically derive the expressions of the DL coverage probability, spectral efficiency and ASE for a building with $2M$+1 storeys, which are simplified to numerically tractable integral expressions for the $M = 1$ case. We show that the $M = 1$ case has similar coverage probability as the $M > 1$ cases, and thus can be used to evaluate the SCN performance in a multi-storey building. The numerical results show the effects of the BS density per storey, storey height and ceiling penetration loss on the indoor wireless coverage performance, and provide guidelines for the indoor small cell deployment and the design of a new building for a better indoor wireless coverage.

1.4 Structure of the Thesis

The thesis is composed of two parts. In Part I, we provide a general introduction to the concepts of various SCNs including mmWave SCNs, HetNets, indoor SCNs and 3D SCNs. In Chapter 2, we introduce the main mathematical tool used in this thesis: stochastic geometry, and its application in modeling SCNs. In Chapter 3, we draw the conclusions and identify some potential future research directions. In Part II, we present three research papers on 3D mmWave SCNs, 3D HetNets and indoor multi-storey SCNs, respectively.

Chapter 2

Mathematical Modeling and Analytical Tools

2.1 Stochastic Geometry

Stochastic geometry based modeling for SCNs is extensively employed by both academia and industry owing to its tractability and its ability to capture the random distribution of SBSs [16, 18]. Stochastic geometry models the locations of BSs in the Euclidean space by a stochastic point process, e.g., PPP, Poisson hard-core process (PHCP), and binomial point process (BPP) [16]. It has been shown in [19] that compared to the actual BS distribution, the PPP model and the grid model provide lower and upper bounds of the coverage probability, respectively, with the same accuracy. More sophisticated point processes, i.e., PHCP and Strauss process (SP) can better model the locations of actual BSs than PPP [17]. Compared to the grid model, stochastic geometry enables more tractable derivations of mathematical expressions for network performance with regard to the coverage probability, ASE, error probability, delay, etc. In some special cases, even closed-form expressions are available. These tractable mathematical expressions can be used to study the effects of crucial network parameters, thereby shedding insights on the deployment of SCNs and the design of network parameters, which are quite time-consuming to obtain in Monte Carlo simulations.

In the modeling with point process, there is a tradeoff between realism and tractability. A point process capturing the actual BS locations may impair the tractability of derivations. In this thesis, we adopt homogeneous PPP due to its higher tractability compared with other point processes [19]. PPP is a kind of point process that in an arbitrary bounded region of the process's underlying space, the point number is a Poisson random variable, and that in disjoint bounded subregions, the point numbers are completely independent [22]. According to Slivnyak's theorem[23], the statistical characteristics observed in a homogeneous PPP is location-independent, and therefore the network performance metrics of an arbitrary user can represent the average network performance metrics of all users.

2.2 Modeling Small-cell Networks Using Stochastic Geometry

2.2.1 Modeling of Small-cell Networks

We adopt a baseline 2D single-tier downlink (DL) SCN to introduce basic stochastic geometry analysis. The locations of BSs and users are modelled as two independent homogeneous PPPs Φ_{B} and Φ_{U} with densities λ_{B} and λ_{U}, respectively. All the BSs and users are equipped with single antenna. Each user is connected to its nearest BS providing the strongest average received signal strength in the considered single-tier SCN. We adopt orthogonal resource partitioning to eliminate intra-cell interference. Therefore, interference comes from the received powers of all other BSs other than the serving BS.

Denoting the distance between a BS and the typical user by d and the path loss exponent by α, the path loss of the link between the BS and the typical user is computed by [24]

$$l(d) = \beta d^{-\alpha}, \tag{2.1}$$

where β is the path loss at reference distance. Note that $l(d)$ can also be called a path gain, but is less than unity. Moreover, LOS and NLOS links may have different path loss exponents,

and the path loss model can be expressed as $l_{\mathrm{L/N}}(d) = \begin{cases} \beta d^{-\alpha^{\mathrm{L}}}, & \text{with prob. } P_{\mathrm{L}}(d) \\ \beta d^{-\alpha^{\mathrm{NL}}}, & \text{with prob. } P_{\mathrm{NL}}(d) \end{cases}$, where α^{L} and α^{NL} are the path loss exponents of LOS and NLOS links, respectively, and $P_{\mathrm{L}}(d)$ and $P_{\mathrm{NL}}(d)$ are the LOS and NLOS probabilities, respectively. In this chapter, we use $l(d)$ for clearer clarification. We adopt Rayleigh fading to model the small-scale fading, and denote its power gain by g, which is exponentially distributed with unit power, i.e., $g \sim \exp(1)$.

Denoting the distance between the serving BS and the typical user by x, the signal-to-interference-plus-noise (SINR) of the typical user is expressed as

$$\mathrm{SINR}(x) = \frac{P g_0 l(x)}{\sum_{\mathrm{B}_i \in \Phi_{\mathrm{B}} \setminus \mathrm{B}_0} P g_i l(R_i) + \delta^2}, \tag{2.2}$$

where P is the BS transmit power, g_0 is the small scale fading power gain between the serving BS B_0 and the typical user, g_i is the small scale fading power gain between the interfering BS B_i and the typical user, R_i is the distance between the interfering BS B_i and the typical user, and δ^2 is the power of additive white Gaussian noise. Then we derive the coverage probability of the typical user, which is defined as the probability that the SINR of the typical user is higher than a given threshold T in the following Lemma.

Lemma 1. *The coverage probability of the typical user is given by*

$$P_c(\lambda_{\mathrm{B}}, T, \alpha) = 2\pi\lambda_{\mathrm{B}} \int_0^{\infty} x \exp\left\{ -\frac{T\delta^2}{Pl(x)} - \pi\lambda_{\mathrm{B}} (K+1) x^2 \right\} \mathrm{d}x, \tag{2.3}$$

where $K = \frac{2T}{\alpha-2}\, {}_2F_1\left[1, 1-\frac{2}{\alpha}; 2-\frac{2}{\alpha}; -T\right]$, ${}_2F_1[\cdot]$ *denotes the Gauss hypergeometric function.*

Proof.

$$
\begin{aligned}
P_c(\lambda_{\mathrm{B}}, T, \alpha) &= \mathbb{P}\left[\mathrm{SINR}(x) > T\right] \\
&= \mathbb{P}\left[g_0 > \sum_{\mathrm{B}_i \in \Phi_{\mathrm{BS}} \setminus \mathrm{B}_0} \frac{T g_i l(R_i)}{l(x)} + \frac{T\delta^2}{Pl(x)}\right] \\
&\overset{(a)}{=} \mathbb{E}_{x,\Phi_{\mathrm{BS}}}\left[\exp(-\frac{T\delta^2}{Pl(x)}) \prod_{\mathrm{B}_i \in \Phi_{\mathrm{BS}} \setminus \mathrm{B}_0} \mathbb{E}_g\left[\exp\{-\frac{T g_i l(R_i)}{l(x)}\}\right]\right] \\
&\overset{(b)}{=} \mathbb{E}_x\left[\exp\left\{-\frac{T\delta^2}{Pl(x)} - 2\pi\lambda_{\mathrm{B}} \int_x^{\infty} t\left(1 - \frac{1}{1+sl(t)}\right)\mathrm{d}t\right\}\right] \\
&\overset{(c)}{=} \mathbb{E}_x\left[\exp\left\{-\frac{T\delta^2}{Pl(x)} - \pi\lambda_{\mathrm{B}} x^2 T^{\frac{2}{\alpha}} \int_{T^{-\frac{2}{\alpha}}}^{\infty} \frac{1}{1+u^{\frac{\alpha}{2}}}\mathrm{d}u\right\}\right] \\
&= \int_0^{\infty} \exp\left\{-\frac{T\delta^2}{Pl(x)} - \pi\lambda_{\mathrm{B}} K x^2\right\} f(x)\mathrm{d}x \\
&= 2\pi\lambda_{\mathrm{B}} \int_0^{\infty} x \exp\left\{-\frac{T\delta^2}{Pl(x)} - \pi\lambda_{\mathrm{B}}(K+1)x^2\right\}\mathrm{d}x,
\end{aligned}
$$

where $f(x) = 2\pi\lambda_{\mathrm{B}}\exp(-\pi\lambda_{\mathrm{B}}x^2)$ is the probability density function (PDF) of x, (a) is due to $g_0 \sim \exp(1)$, (b) is obtained from the probability generating functional (PGFL) of homogeneous PPP, and (c) comes from a variable transition $u = \frac{T^{-\frac{2}{\alpha}}t}{x^2}$. □

In a dense SCN, the impact of noise on the network coverage performance can be ignored [19], and (2.3) can be simplified as

$$
\overline{P}_c(T, \alpha) = 2\pi\lambda \int_0^{\infty} x \exp\left\{-\pi\lambda(K+1)x^2\right\}\mathrm{d}x = \frac{1}{K+1}. \tag{2.4}
$$

From (2.4), we can see that the network coverage performance in an interference-limited network does not depend on λ_{B}. This conclusion explains the linear increase of network throughput during the past decades obtained by the deployment of SBSs. However, more practical factors needs to be further integrated, which are introduced in the following works.

In [25], the authors revisited the path loss model, especially the near-field path loss. In accordance with the practical channel measurement that the path loss in proximity with the receiver is lower than that of other slopes. Based on this observation a multi-slope path loss model was proposed. The distribution of BSs was modelled as a PPP and the numerical results

showed that the network coverage performance first grows and then degrades with the increasing BS intensity. The increase of coverage probability is attributed to the improved desired signal power, while the coverage probability decay results from the higher near-field interference. In addition, it was observed that as long as the near-field path loss exponent is smaller than 2, both the network coverage and capacity degrade to zero when the BS density increases to infinity. This result means an end of the linear scaling of network capacity, indicating that the dense small-cell network need to be designed considering the practical channel models.

For the modeling of dense small-cell networks, another type of channel model, i.e, the bounded channel model, was investigated in [26][27]. To address the energy non-conservation problem at short transmission distances smaller than 1 m, the authors in [26] used the bounded path loss models to analyze the network performance with regard to coverage and capacity. The results showed that for a interference-limited network, the coverage probability monotonically degrades with the BS density, and that the ASE first grows to a peak and then degrades towards zero. In [27], a simplified bounded model was proposed, with which both the coverage probability and ASE were derived in closed-form. Moreover, the expression of the optimal BS density that maximizes the ASE was obtained.

In [28], the authors integrated the non-line-of-sight (NLOS) transmission into the channel modeling, in which a LOS probability function was employed to distinguish between LOS and NLOS links. The NLOS links were assumed to experience higher path loss than the LOS links. Moreover, the multi-slope path loss model was adopted to make the channel model more practical. It was revealed that network coverage performance first grows to a peak value and then degrades with the BS intensity. This is because the BSs in proximity are more likely to be LOS BSs, a denser network brings more LOS BSs, but on the other hand increases the Interference. The increase of ASE will also undertake a slowdown after a particular BS density.

To investigate the blockage effects of practical buildings, stochastic geometry was used to model urban buildings in [29] where the distribution of BSs and blockages were modelled as two independent PPPs. The shapes of buildings were modelled to be rectangles with random sizes and orientations and the LOS probability was derived as a distance dependent function. Subsequently, the expressions of connectivity and coverage probability were derived and the

numerical results showed that the network coverage performance first grows and then degrades with the BS intensity, indicating that an appropriate density of blockages is beneficial through reducing part of the interference. However, excessive blockages will degrade the coverage probability since the closest transmission BS may be blocked. This work can also be extended to 3D networks considering the heights of BSs and buildings.

2.2.2 Modeling of Millimeter-wave Small-cell Networks

MmWave SCNs are different with conventional networks in terms of channel characteristics and antenna patterns, which need to be incorporated into the analysis of coverage and capacity. Firstly, mmWave channels are sparse with regard to multipath components due to the poor scattering environments [30]. Therefore, the modeling of small-scale fading by Rayleigh fading, which is widely used in sub-6 GHz systems, is no longer applicable. Instead, Nakagami-m fading is commonly adopted to model small-scale fading in mmWave channels. Secondly, since signals at mmWave frequencies experience severe penetration loss through a variety of materials, e.g., concrete, bricks, and even human bodies, the effects of blockages have to be considered. A feasible way is to model the locations of blockages by PPP, and the shape, size, and orientation of blockages using random shape theory. The LOS probability of a link, i.e., the probability that no blockage lies across a link, is a monotonically decreasing function of the transmission distance [29]. A simplified LOS-ball model was proposed to approximate the LOS probability function in [31], where a link is considered to be LOS within a fixed distance R_{L}, and NLOS outside the distance, as shown in Fig. 2.1. This model enables tractable analysis of network performance and has been widely adopted in the previous work [32, 33]. Last but not least, it is not practical to have one RF chain per antenna element due to the excessive power consumption of RF chain components at mmWave frequencies [31]. Therefore, most work adopts analog beamforming architectures where analog phase shifters are used to control the phase of each antenna element. A simplified sectored pattern was proposed to approximate the actual analog beamforming pattern [31], where the antenna gains of the main-lobe direction and side-lobe direction are characterized by two constants G_{M} and G_{m}, respectively, as shown

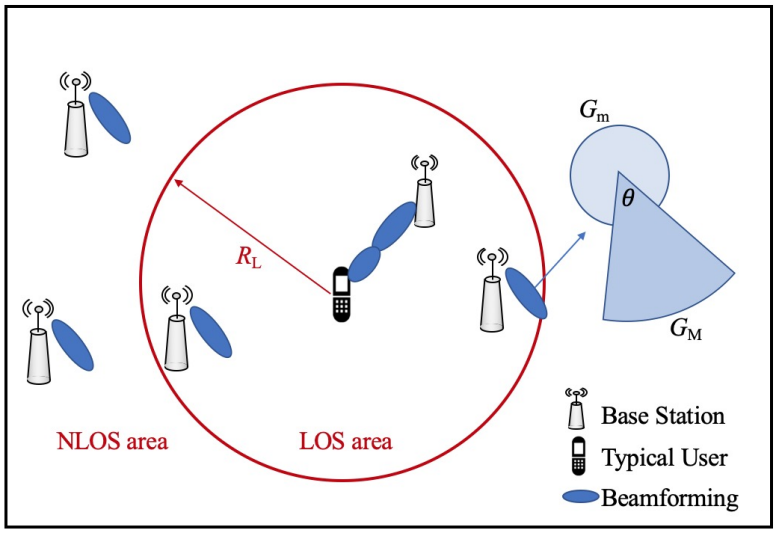

Fig. 2.1 An illustration of LOS-ball model and beamforming pattern.

in Fig. 2.1. The main-lobe gain can only be achieved when the user is located in the main-lobe area with half-power beam width θ.

There has been some work investigating more practical modeling of analog beamforming. In [34], a multi-lobe model was proposed to provide a step-wise approximation of the actual antenna radiation pattern, which is an extended version of the sectored model. This model was proved to be accurate by performing numerical simulations. However, the impact of the number of antennas on the antenna radiation pattern was not characterized. In [32], the actual antenna pattern when aligning the beam direction exactly with the angles of departure (AoD) was characterized as a function of the number of antennas, and was approximated by a sinc function and a cosine function. These two approximated antenna patterns were tractable for the analysis of coverage probability with a high level of accuracy. In [35], the authors adopted the approximated antenna patterns proposed by [32] to analyze the coverage of a mmWave device-to-device (D2D) network where different devices may have different number of antennas. In [35], the authors compared multiuser multiple-input multiple-output (MIMO) enabled by hybrid beamforming with single-user analog beamforming, and showed that hybrid beamforming performs better regarding coverage and rate.

Nevertheless, all the aforementioned works modelled and analysed mmWave SCNs on a 2D plane.

2.2.3 Modeling of Heterogeneous Networks

HetNets are usually modelled as multi-tier networks where the network parameters are mutually independent across tiers. Consider a K-tier HetNet, in which the locations of BSs in the kth tier follow a PPP Φ_k with density λ_k. The transmit power of BSs, path loss at the reference distance and path loss exponent in the kth tier are P_k, β_k and α_k, respectively. Each tier is allocated with an association bias for traffic offloading, and the association bias for the kth tier is denoted by B_k. It is usually assumed that each user connects to the BS offering the strongest biased received signal strength. Denoting the distance between the nearest BS in the kth tier and the typical user by r_k, the index of the tier the typical user connected to is $\underset{k}{\operatorname{argmax}}\, P_k B_k \beta_k r_k^{-\alpha_k}$. The coverage probability of the typical user in the HetNet is given by $P_c^H = A_k P_{c,k}$, where A_k denotes the probability that the typical user connects to the kth tier, and $P_{c,k}$ is the coverage probability when the typical user connects to the kth tier. More details of derivations with regard to coverage and rate can be found in [36], and more issues in the modeling of HetNets are introduced in the following works.

The synergy of multi-antenna transmission and HetNet was modelled and the optimal per-tier bias that maximises the DL coverage was given in [37]. This work assumed Multiple-input single-output (MISO) transmission, where the BSs have multiple antennas and the users have a single antenna. The number of antennas and number of users served per-BS may differ across tiers. The numerical results revealed that the number of antennas can serve as a kind of bias that offloads the macrocell users to small cells, reducing the artificial design of cell association bias.

Considering the multi-slope path loss model and directional antenna gain, the authors in [38] extended the HetNet model to millimeter wave networks and analysed the DL coverage performance. More specifically, the multi-slope path loss model was employed to analyze the effects of NLOS links and an approximated sectored model was used to model the directional antenna gain. Moreover, the energy efficiency (EE) was derived and the results showed that there exists an optimal cell association bias maximizing the EE. This work can also be extended to the modeling of the microwave (μWave)-mmWave hybrid network.

In [39], a framework was given for the modeling of a device-to-device (D2D) enabled HetNet with dynamic time-division duplex (TDD). The network performance regarding coverage probability and capacity were evaluated and the effects of network parameters, e.g., the BS density, per-tier bias and uplink (UL)/DL configuration were analysed. Based on the numerical results, the authors proposed a guideline for the optimal design of D2D networks.

In [40], the authors investigated coordinated multipoint (CoMP) transmission in HetNets, in which each user is simultaneously served by a set of BSs selected on the basis of their average received signal strength levels. The joint transmission reduces the interference level, and hence enhances the coverage and rate. It was shown that the network coverage performance does not depend on the transmit power and BS intensity when the HetNet becomes interference-limited.

However, all of these works modelled the HetNets on a 2D plane.

2.2.4 Modeling of Indoor Small-cell Networks

Due to the complex built environment, there is little literature found on tractable modeling of indoor wireless networks using stochastic geometry. In [41], the authors investigated the performance of an urban cellular network. A two-tier HetNet with indoor SBSs and outdoor MBSs was modelled to analyze the coverage performance of indoor users, where the outdoor-to-indoor penetration loss was considered. However, this work assumed that one building is served by only one BS, which may not be sufficient to handle high indoor traffic demands.

Several works have studied the effects of interior walls. In [42], the authors modelled the interior walls by random object process (ROP), where the center points of walls are PPP distributed, and each wall has uniformly distributed length and orientation. The locations of BSs were modelled by PPP and the coverage probability and ASE were derived. The results revealed that more walls and higher penetration loss of walls enhance the network performance since more interference is blocked. However, this work adopted the closest BS association strategy, which underestimated the indoor network performance. In [43], we modelled the interior walls following the assumptions in [42] and derived the expression of the coverage probability under the condition that each user is connected to its nearest LOS BS. The results revealed that there is an optimal BS intensity maximizing the network coverage performance.

Nevertheless, the random assumption of walls in terms of length and orientation in the above two studies is not practical in general. In [44], the authors analyzed different wall generation models: ROP, Manhattan grid model where the walls modelled as two Manhattan line processes (MLP), and regular wall model where the walls are oriented perpendicular to the coordinate axes with infinite length and the distance between arbitrary two walls is fixed. These tractable wall generation models were compared with the walls generated according to practical floor plans regarding signal-to-interference-ratio (SIR) performance. The results showed that the Manhattan grid model best matches the practical floor plan.

However, these works focused on the modeling of buildings or walls on a 2D plane.

2.2.5 Modeling of 3D Small-cell Networks

In dense SCNs, BSs and users communicate in proximity, and hence the BS height significantly affects the network performance regarding coverage and rate. Assume that the height of all BSs is H_{B}, the height of all users is H_{U} and the height difference between BSs and users is $H = H_{\mathrm{B}} - H_{\mathrm{U}}$. Out of practical considerations, it is assumed that $H \geq 0$. Following the steps in Lemma 1, the DL coverage probability of a one-tier 3D SCN is computed by

$$\begin{aligned} P_c^{3D}(\lambda_{\mathrm{B}}, T, \alpha, H) &= \mathbb{E}_x \left[\exp\left\{ -\frac{T\delta^2}{Pl_{3D}(x)} - 2\pi\lambda_{\mathrm{B}} \int_x^{\infty} t \left(1 - \frac{1}{1+sl_{3D}(t)}\right) \mathrm{d}t \right\} \right] \\ &= \mathbb{E}_x \left[\exp\left\{ -\frac{T\delta^2}{Pl_{3D}(x)} - \pi\lambda_{\mathrm{B}} \left(x^2+H^2\right) T^{\frac{2}{\alpha}} \int_{T^{-\frac{2}{\alpha}}}^{\infty} \frac{1}{1+v^{\frac{\alpha}{2}}} \mathrm{d}u \right\} \right] \\ &= \int_0^{\infty} \exp\left\{ -\frac{T\delta^2}{Pl_{3D}(x)} - \pi\lambda_{\mathrm{B}} K x^2 \right\} f(x) \mathrm{d}x \\ &= 2\pi\lambda_{\mathrm{B}} \int_0^{\infty} x \exp\left\{ -\frac{T\delta^2}{Pl_{3D}(x)} - \pi\lambda_{\mathrm{B}} \left[K\left(x^2+H^2\right) + x^2 \right] \right\} \mathrm{d}x, \end{aligned} \tag{2.5}$$

where $l_{3D}(x) = \beta \left(x^2+H^2\right)^{-\frac{\alpha}{2}}$ and $v = \frac{T^{-\frac{2}{\alpha}}\left(t+H^2\right)}{\left(x^2+H^2\right)}$. In an interference-limited SCN, (2.5) can be simplified as

$$\overline{P}_c^{3D}(\lambda_{\mathrm{B}}, T, \alpha, H) = 2\pi\lambda_{\mathrm{B}} \int_0^{\infty} x \exp\left\{ -\pi\lambda_{\mathrm{B}} \left[K\left(x^2+H^2\right) + x^2 \right] \right\} \mathrm{d}x = \frac{e^{-\pi\lambda_{\mathrm{B}} H^2}}{K+1}. \tag{2.6}$$

It is observed from (2.6) that the coverage probability monotonically degrades with λ_B and H, and that the coverage probability decays to zero when λ_B goes to infinity. For more issues in the modeling of 3D SCNs, please refer to the following works.

The effects of blockages and BS height on the network coverage and throughput were studied in [21]. The results revealed that the coverage probability first grows to a peak and then degrades with the BS height in a sparse network. This is because an approximate BS height improves the LOS probability of the desired signals, while an excessive BS height leads to severe interference. Moreover, it was shown that if the BS height exceeds the user height, both the network coverage and capacity degrade to zero when the BS density increases to infinity. In [45], a multi-slope path loss model was employed to analyze the effect of the height difference between BSs and users on the ASE. It was shown that even if the directional antennas are equipped, the ASE decrease to zero when the BS density increases to infinity.

Some studies have employed 3D PPP to model the distribution of BSs with density in BSs/m^3 in high-rise buildings. The authors of [46] adopted the free space path loss channel model to analyze the coverage probability of a SCN where the BSs are 3D PPP distributed. The results showed that the coverage probability will degrade to zero if the path loss exponent is lower than 3. In [47], the dual-slope path loss model was adopted in a SCN modelled by a 3D PPP. When the density of BSs tends to infinity, the asymptotic analysis revealed that the network coverage would degrade to zero. However, despite its tractability, 3D PPP assumes a Poisson distributed random BS height. This assumption cannot be applied to outdoor SCNs, where BSs in the same tier are usually deployed at similar heights. Even in indoor SCNs, BSs on the same floor are usually deployed at similar heights as well. Therefore, in this thesis, we assume that BSs in the same tier or on the same floor have the same height.

Chapter 3

Conclusions and Future Research

3.1 Concluding Remarks

In this thesis, we have proposed novel and tractable stochastic geometry frameworks for the performance evaluation of 3D mmWave SCNs, 3D HetNets and indoor multi-storey SCNs. For each SCN scenario, we have analytically derived the expressions of network performance metrics, e.g., coverage probability and ASE, the accuracy of which is verified by simulations.

In outdoor 3D mmWave SCNs, we have shown that a larger antenna array leads to a higher DL coverage probability, and that the DL coverage probability first grows to a peak and then degrades with the BS antenna downtilt. Thanks to the BS antenna downtilt gain, 3D mmWave SCNs can provide higher coverage probability than 2D mmWave SCNs where BSs have the same height as users. The optimal BS antenna downtilt corresponding to the maximum DL coverage probability is higher when the BS density and BS height increase. Furthermore, for given BS density and blockage distribution, the BS height and BS antenna downtilt can be jointly optimized to maximize the DL coverage probability and ASE. The ASE can increase linearly with the BS density when BSs have the same height as users, and can be further improved when the BS height and BS antenna downtilt are jointly optimized.

In outdoor 3D HetNets, we have shown that for given MBS deployment, at low to medium SBS densities, the closest BS cell-association strategy leads to low DL ergodic rate when no bias is used; while the closest BS cell-association strategy can achieve similar ergodic rate as

the strongest received signal cell-association strategy by properly tuning the small-cell bias. At high SBS densities, under both cell-association strategies, SBSs should be deployed at the same height as users to achieve high ergodic rate, ASE and energy efficiency. Different from single-tier SCNs, the ergodic rate monotonically decreases with the SBS density since the HetNet is interference-limited in the presence of MBSs. Since antennas are deployed in horizontal linear arrays, the ergodic rate decreases with the SBS height at high SBS densities. Moreover, in the absence of vertical beamforming, the ASE increases linearly with the SBS density only when SBSs have the same height as users. Therefore, it is necessary to deploy vertical antenna arrays at high SBS densities. Although deploying more antennas always leads to a higher ergodic rate, it impairs the energy efficiency when excessive antennas are deployed. It has been observed that when other system parameters are fixed, the energy efficiency can be maximized by a joint optimization of the number of antennas per SBS and the SBS density. It will be of interest to investigate 3D HetNets with 2D antenna arrays in the future.

In indoor multi-storey SCNs, we have shown that the single-storey indoor SCN overestimates the DL coverage probability of an actual multi-storey SCN, ignoring the interference from other storeys. A novel theoretical discovery has been presented, i.e., the problem of *Coverage Probability Valley*. The coverage probability first decreases and then increases with the increase of the storey height and the BS density. Due to the *Coverage Probability Valley*, certain values of storey height and BS density should be avoided for a high coverage probability. Furthermore, we have shown that a higher penetration loss of the ceiling leads to a higher DL coverage probability by reducing the interference of BSs on other storeys. These numerical results demonstrate that the indoor small cell deployment and the building structure can be jointly optimized for a better indoor wireless coverage. Similar to the observations in 3D HetNets, we have observed that in the presence of single-antenna BSs, the maximum coverage probability in multi-storey SCNs is achieved when the BS height is the same as the user height. This conclusion may be different when vertical antenna arrays are deployed on BSs.

3.2 Future Research Directions

The potential areas for future research are summarized as follows:

- User mobility and blockage mobility are critical issues in mmWave network as the transmission links are sensitive to blockages and the narrow antenna beams rely on efficient beam alignment. It is more challenging to handle mobility in 3D space due to higher overhead in channel estimation and beam training for 3D beamforming. Thus, it would be interesting to analyze the impact of mobility on 3D mmWave SCNs.

- The coexisting of mmWave and conventional microwave networks makes it necessary to systematically evaluate the performance of multiband 3D heterogeneous SCNs, where BSs in different tiers may have potentially different antenna array sizes and beamforming techniques. Moreover, the beam misalignment due to the imperfect channel state information can be incorporated into the analysis.

- The proliferation of the number and use cases of unmanned aerial vehicles (UAVs) requires reliable and high-throughput links. It is of interest to examine the network performance of UAVs served by 3D SCNS, taking into account the coexisting of UAVs and ground users, and different propagation conditions for these two types of users.

- Indoor mmWave SCN equipped with massive MIMO is a promising solution to address high indoor traffic demands. The deployment of indoor mmWave small cells and the configuration of massive MIMO are still open problems. Hence, it is of interest to model indoor 3D mmWave SCNs, considering actual indoor built environments with walls and stochastic blockages.

- Other system performance aspects such as backhaul capacity, uplink communication performance, delay and energy efficiency need to be further investigated to provide a comprehensive understanding of 3D SCNs. Moreover, considering realistic distributions of traffic load and user locations may yield interesting results.

- The application of emerging technologies for the sixth generation cellular networks (6G), e.g., terahertz communication and intelligent reflective surface (IRS) in 3D SCNs, will introduce new research opportunities.

References

[1] Cisco, "Cisco annual internet report (2018-2023)," Tech. Rep., Mar. 2020.

[2] J. G. Andrews *et al.*, "What will 5g be?" *IEEE J. Sel. Areas Commun.*, vol. 32, no. 6, pp. 1065–1082, Jun. 2014.

[3] Cisco, "Cisco visual networking index: Global mobile data traffic forecast update (2015–2020)," Feb. 2016.

[4] ArrayComm and William Webb, Ofcom, London, U.K., 2007.

[5] "Market status statistics feb 2016 — mobile experts," *Small Cell Forum*, Feb. 2016.

[6] T. S. Rappaport, S. Sun, R. Mayzus, H. Zhao, Y. Azar, K. Wang, G. N. Wong, J. K. Schulz, M. Samimi, and F. Gutierrez, "Millimeter wave mobile communications for 5g cellular: It will work!" *IEEE Access*, vol. 1, pp. 335–349, May. 2013.

[7] S. Rangan, T. S. Rappaport, and E. Erkip, "Millimeter-wave cellular wireless networks: potentials and challenges," *Proceedings of the IEEE*, vol. 102, no. 3, pp. 366–385, 2014.

[8] Ericsson, "Ericsson, qualcomm and u.s. cellular achieve extended-range 5g data call over mmwave," Tech. Rep. Sep. 2020.

[9] S. Rangan, T. S. Rappaport, and E. Erkip, "Millimeter-wave cellular wireless networks: Potentials and challenges," *Proc. IEEE*, vol. 102, no. 3, pp. 366–385, Mar. 2014.

[10] I. Hwang, B. Song, and S. S. Soliman, "A holistic view on hyper-dense heterogeneous and small cell networks," *IEEE Communications Magazine*, vol. 51, no. 6, pp. 20–27, Jun. 2013.

[11] C. Liu, M. Li, S. V. Hanly, I. B. Collings, and P. Whiting, "Millimeter wave beam alignment: large deviations analysis and design insights," *IEEE J. Sel. Areas Commun.*, vol. 35, no. 7, pp. 1619–1631, 2017.

[12] D. López-Pérez, M. Ding, H. Claussen, and A. H. Jafari, "Towards 1 gbps/ue in cellular systems: Understanding ultra-dense small cell deployments," *IEEE Commun. Surveys Tuts.*, vol. 17, no. 4, p. 2078–2101, 4th Quart 2015.

[13] Y. S. Soh, T. Q. S. Quek, M. Kountouris, and H. Shin, "Energy efficient heterogeneous cellular networks," *IEEE J. Sel. Areas Commun.*, vol. 31, no. 5, pp. 840–850, 2013.

[14] Huawei, "Five trends to small cell 2020," 2016.

[15] H.-Y. Hsieh, S.-E. Wei, and C.-P. Chien, "Optimizing small cell deployment in arbitrary wireless networks with minimum service rate constraints," *IEEE Trans. Mobile Comput.*, vol. 13, no. 8, Aug. 2014.

[16] H. ElSawy, A. Sultan-Salem, M.-S. Alouini, and M. Z. Win, "Modeling and analysis of cellular networks using stochastic geometry: A tutorial," *IEEE Commun. Surv. Tutor.*, vol. 19, no. 1, pp. 167–203, Firstquarter 2017.

[17] A. Guo and M. Haenggi, "Spatial stochastic models and metrics for the structure of base stations in cellular networks," *IEEE Trans. Wireless Commun.*, vol. 12, no. 11, pp. 5800–5812, Nov. 2013.

[18] M. Haenggi, J. G. Andrews, F. Baccelli, O. Dousse, and M. Franceschetti, "Stochastic geometry and random graphs for the analysis and design of wireless networks," *IEEE J. Sel. Areas Commun.*, vol. 27, no. 7, pp. 1029–1046, Sep 2009.

[19] J. G. Andrews, F. Baccelli, and R. K. Ganti, "A tractable approach to coverage and rate in cellular networks," *IEEE Trans. Commun.*, vol. 59, no. 11, pp. 3122–3134, Nov. 2011.

[20] J. Liu, M. Sheng, K. Wang, and J. Li, "The impact of antenna height difference on the performance of downlink cellular networks," Singapore, pp. 1–7, 2017.

[21] I. Atzeni, J. Arnau, and M. Kountouris, "Downlink cellular network analysis with los/nlos propagation and elevated base stations," *IEEE Trans. Wireless Commun.*, vol. 17, no. 1, pp. 142–156, Jan. 2018.

[22] C.-S. Choi, J. O. Woo, and J. G. Andrews, "An analytical framework for modeling a spatially repulsive cellular network," *IEEE IEEE Trans. Commun.*, vol. 66, no. 2, pp. 862–874, 2018.

[23] W. K. D. Stoyan and J. Mecke, *Stochastic Geometry and Its Applications*, 2nd edition. John Wiley and Sons, 1996.

[24] Y. Zhong, T. Q. S. Quek, and X. Ge, "Heterogeneous cellular networks with spatio-temporal traffic: delay analysis and scheduling," *IEEE J. Sel. Areas Commun.*, vol. 35, no. 6, pp. 1373–1386, Jun. 2017.

[25] X. Zhang and J. G. Andrews, "Downlink cellular network analysis with multi-slope path loss models," *IEEE Trans. Commun.*, vol. 63, no. 5, pp. 1881–1894, May. 2015.

[26] J. Liu, M. Sheng, L. Liu, and J. Li, "Effect of densification on cellular network performance with bounded pathloss model," *IEEE Commun. Lett.*, vol. 21, no. 2, pp. 346–349, Feb. 2017.

[27] C. Chen, S. Yang, J. Zhang, X. Chu, and J. Zhang, "Tractable performance analysis of small-cell networks with a novel bounded path loss model," *Electron. Lett.*, vol. 56, no. 2, pp. 105–107, 2020.

[28] M. Ding, P. Wang, D. López-Pérez, G. Mao, and Z. Lin, "Performance impact of los and nlos transmissions in dense cellular networks," *IEEE Trans. Wireless Commun.*, vol. 15, no. 3, pp. 2365–2380, Mar. 2016.

[29] T. Bai, R. Vaze, and R. W. Heath, "Analysis of blockage effects on urban cellular networks," *IEEE Trans. Wireless Commun.*, vol. 13, no. 9, pp. 5070–5083, Sep. 2014.

[30] M. R. Akdeniz, Y. Liu, M. K. Samimi, S. Sun, S. Rangan, T. S. Rappaport, and E. Erkip, "Millimeter wave channel modeling and cellular capacity evaluation," *IEEE J. Sel. Areas Commun.*, vol. 32, no. 6, pp. 1164–1179, Jun. 2014.

[31] A. A. T. Bai and R. W. Heath, "Coverage and capacity of millimeter-wave cellular networks," *IEEE Commun. Mag.*, vol. 52, no. 9, pp. 70–77, Sep. 2014.

[32] X. Yu, J. Zhang, M. Haenggi, and K. B. Letaief, "Coverage analysis for millimeter wave networks: The impact of directional antenna arrays," *IEEE J. Sel. Areas Commun.*, vol. 35, no. 7, pp. 1498–1512, Jul. 2017.

[33] J. G. Andrews, T. Bai, M. N. Kulkarni, A. Alkhateeb, A. K. Gupta, and R. W. Heath, "Modeling and analyzing millimeter wave cellular systems," *IEEE Trans. Commun.*, vol. 65, no. 1, pp. 403–430, Jan. 2017.

[34] W. L. M. Di Renzo and P. Guan, "The intensity matching approach: A tractable stochastic geometry approximation to system-level analysis of cellular networks," *IEEE Trans. Wireless Commun.*, vol. 15, no. 9, p. 5963–5983, Sep. 2016.

[35] M. N. Kulkarni, A. Ghosh, and J. G. Andrews, "A comparison of mimo techniques in downlink millimeter wave cellular networks with hybrid beamforming," *IEEE Trans. Commun.*, vol. 64, no. 5, pp. 1952–1967, May. 2016.

[36] H. Jo, Y. J. Sang, P. Xia, and J. G. Andrews, "Heterogeneous cellular networks with flexible cell association: a comprehensive downlink sinr analysis," *IEEE Trans. Wireless Commun.*, vol. 11, no. 10, pp. 3484–3495, Oct. 2012.

[37] A. Adhikary, H. S. Dhillon, and G. Caire, "Massive-mimo meets hetnet: Interference coordination through spatial blanking," *IEEE J. Sel. Areas Commun.*, vol. 33, no. 6, pp. 1171–1186, 2015.

[38] E. Turgut and M. C. Gursoy, "Coverage in heterogeneous downlink millimeter wave cellular networks," *IEEE Trans. Commun.*, vol. 65, no. 10, pp. 4463–4477, Oct. 2017.

[39] H. Sun, M. Wildemeersch, M. Sheng, and T. Q. S. Quek, "D2d enhanced heterogeneous cellular networks with dynamic tdd," *IEEE Trans. Wireless Commun.*, vol. 14, no. 8, pp. 4204–4218, Aug. 2015.

[40] G. Nigam, P. Minero, and M. Haenggi, "Coordinated multipoint joint transmission in heterogeneous networks," *IEEE Trans. Commun.*, vol. 62, no. 11, pp. 4134–4146, Nov. 2014.

[41] M. Taranetz, R. W. Heath, and M. Rupp, "Analysis of urban two-tier heterogeneous mobile networks with small cell partitioning," *IEEE Trans. Wireless Commun.*, vol. 15, no. 10, pp. 7044–7057, Oct. 2016.

[42] M. K. Müller, S. Schwarz, and M. Rupp, "Investigation of area spectral efficiency in indoor wireless communications by blockage models," in *2018 16th International Symposium on Modeling and Optimization in Mobile, Ad Hoc, and Wireless Networks (WiOpt)*, 2018, pp. 1–6.

[43] Y. Wang, H. Zheng, C.Chen, and X. Chu, "The effect of wall blockages on indoor smallcell networks with los/nlos user association strategies," accepted by VTC2021-Spring.

[44] M. K. Muller, M. Taranetz, and M. Rupp, "Analyzing wireless indoor communications by blockage models," *IEEE Access*, vol. 5, pp. 2172–2186, 2017.

[45] M. Ding and D. López-Pérez, "Performance impact of base station antenna heights in dense cellular networks," *IEEE Trans. Wireless Commun.*, vol. 16, no. 12, pp. 8147–8161, Dec. 2017.

[46] Z. Pan and Q. Zhu, "Modeling and analysis of coverage in 3d cellular networks," *IEEE Commun. Lett.*, vol. 19, no. 5, pp. 831–834, May. 2015.

[47] A. K. Gupta, X. Zhang, and J. G. Andrews, "Sinr and throughput scaling in ultradense urban cellular networks," *IEEE Wireless Commun. Lett.*, vol. 4, no. 6, pp. 605–608, Dec. 2015.

Part II

Papers

Paper I

Performance Analysis for 3D Millimeter-wave Small-cell Networks, co-authored with M. Zhou, J. Zhang, X. Chu, F. Naessens and J. Zhang. This paper has been submitted to IEEE Transactions on Wireless Communications.

I conceived the idea and carried out the mathematical analysis, numerical simulations and writing of the manuscript. Mengxin Zhou, Jiliang Zhang, Xiaoli Chu, Frederik Naessens and I contributed to the network modelling. Xiaoli Chu and Jie Zhang guided and supervised the work. All authors discussed the theoretical aspects and numerical results, and reviewed the manuscript.

Performance Analysis for 3D Millimeter-wave Small-cell Networks

Chen Chen[1], Mengxin Zhou[1], Jiliang Zhang[1], Xiaoli Chu[1], Frederik Naessens[2], and Jie Zhang[1,3]

[1] Department of Electronic and Electrical Engineering, the University of Sheffield, Sheffield, S10 2TN, UK

[2] Televic Conference NV, Leo Bekaertlaan 1, 8870 Izegem, Belgium

[3] Ranplan Wireless Network Design Ltd., Cambridge, CB23 3UY, UK

Abstract

Millimeter-wave (mmWave) small-cell networks (SCNs) have been a promising solution to enhancing network capacity. However, most existing works modelled mmWave SCNs on a two-dimensional (2D) plane, which does not capture the three-dimensional (3D) nature of deployment environments. In this paper, we present a 3D system model for mmWave SCNs, where the potentially different heights of base stations (BSs), users and blockages are modeled, and the locations of BSs, users and blockages follow three independent Poisson point processes. Moreover, we characterize the 3D BS antenna radiation pattern and decompose it into the antenna downtilt gain and beamforming gain to facilitate the performance analysis. Based on the 3D system model, we drive the integral-form approximate expressions for the downlink (DL) coverage probability (CP) and the area spectral efficiency (ASE), and their closed-from expressions for special cases such as ultra-dense 3D mmWave SCNs. Our numerical results reveal that the DL CP first grows to a peak and then degrades with the BS antenna downtilt, and that the optimal BS antenna downtilt maximizing the DL CP increases with the BS density and BS height. Furthermore, we observe that for given BS density, blockage density, user height and distribution of blockage heights, the DL CP and ASE can be maximized by jointly optimizing the BS height and BS antenna downtilt.

1 Introduction

Mobile traffic demand has been increasing in an exponential fashion due to the emerging data-hungry applications such as Internet of Things, virtual reality, and autonomous vehicles [1, 2]. In this light, the use of millimeter-wave (mmWave) bands in conjunction with massive antenna arrays and small-cell networks (SCNs) has been regarded to be a key driver of network capacity gains for the fifth-generation (5G) mobile cellular networks [3–7].

Most existing works modeled mmWave SCNs on a two-dimensional (2D) plane, ignoring the height difference between base stations (BSs) and users. Nevertheless, recent studies [8, 9] revealed that the elevated BS has a prominent negative impact on the coverage probability (CP) and area spectral efficiency (ASE), especially when the SCN becomes ultra-dense. It is worth noting that the height difference between BSs and users can be exploited to improve network performance. On the one hand, a properly configured BS antenna downtilt brings a vertical antenna gain. On the other hand, 3D beamforming techniques can achieve antenna array gains in both the elevation and the conventional azimuth dimensions [10].

In this paper, we develop a novel mathematical framework to model the features of 3D mmWave SCNs, including the 3D antenna radiation patterns for BSs and the potentially different heights of BSs, users and blockages, as well as their spatial distributions. Based on the 3D framework, we derive the analytical expressions of the downlink (DL) CP and ASE, and use them to evaluate the effects of the BS height, BS density, and BS antenna downtilt on the DL CP and ASE.

1.1 Related Works

MmWave SCNs have been extensively investigated using the tools from stochastic geometry [11–14]. Due to the higher penetration loss through blockages at mmWave frequencies than at micro-wave frequencies, Non-Line-Of-Sight (NLOS) links need to be integrated into the modelling. In [11], the authors adopted a sectored model to approximate the antenna array gain and a Line-Of-Sight (LOS) ball model, where the LOS region is assumed to be a ball with a fixed radius centered at the receiver of interest, to approximate the effect of blockages

in single-tier mmWave cellular networks. The similar analytical methods were applied to heterogeneous mmWave cellular networks in [12]. Although these approximations render the analysis tractable, they sacrifice the accuracy of the analytical results. In [14], two 2D antenna patterns were proposed to characterize the actual antenna array gain, but the effects of blockages were still analyzed using the simple LOS ball model. Moreover, all these works modeled mmWave SCNs on a 2D plane.

Several recent works have studied 3D cellular networks, involving the modeling of 3D antenna patterns [15–17]. In [15], the joint impact of the BS antenna arrays and antenna downtilt on the DL CP was investigated via simulations in a hexagonal cellular network. Based on stochastic geometry, in [17], the expression of CP was derived and the optimal BS antenna downtilt that maximizes the DL CP was obtained numerically. However, none of the aforementioned works considered the distinct features of mmWave SCNs such as the sensitivity to blockages and the use of large antenna arrays.

There are few works on system-level performance evaluation of 3D mmWave SCNs using stochastic geometry. In [18], the authors characterized the impact of human bodies on mmWave signal propagation by modeling the human bodies as cylinders, and derived the LOS probability and the received signal strength as functions of transmitter-receiver distance, user density and user height. In [19], transmitters and receivers were modeled as cylinders and were assumed to be blockages that may block the interfering signals. Although both vertical and horizontal directivities of the BS antenna array were characterized, the relationship between the BS antenna array gain and the number of BS antennas was not given. Note that neither [18] nor [19] provided network performance analysis in terms of CP or spectral efficiency.

So far, the performance of 3D mmWave SCNs has not been analyzed in conjunction with 3D modeling of blockages and antenna radiation patterns, which will be studied in this paper.

1.2 Contributions

The main goal of this paper is to analyze the performance of 3D mmWave SCNs regarding the DL CP and ASE. Our main contributions are listed as follows:

- We develop a tractable mathematical framework for the performance analysis of 3D mmWave SCNs using stochastic geometry, capturing the effects of the height difference between BSs and users, 3D blockages, and 3D radiation patterns of large antenna arrays deployed at BSs. To facilitate fast numerical analysis, we propose a simple exponential expression to approximate the BS antenna downtilt gain with a very high level of accuracy.

- Based on the analytical framework, we derive the LOS probability of a link as a function of network parameters such as the BS density, the blockage density, the link distance, and the height difference between BSs and users.

- Leveraging the derived BS antenna downtilt gain and link LoS probability, we derive an integral-form expression of the DL CP for general 3D mmWave SCNs, and obtain its closed-form expression for ultra-dense 3D mmWave SCNs with isotropic BS antennas. The numerical results show that there will be an optimal BS antenna downtilt maximizing the DL CP and that for given BS density, blockage density, user height and distribution of blockage heights, the DL CP and ASE can be maximized by jointly optimizing the BS height and BS antenna downtilt.

1.3 Paper Organization

This paper is structured as follows. Section 2 introduces the system model. The expressions of the DL CP and ASE are derived in Section 3 and 4, respectively. The numerical results are presented in Section 5, with remarks providing novel guidelines on the joint optimization of BS height and BS antenna downtilt. The conclusions of this paper are drawn in Section 6.

2 System Model

2.1 Network Model

Our proposed outdoor 3D mmWave SCN model is illustrated in Fig. 1. The locations of the BSs, blockages and users are modeled following three independent homogeneous Poisson

Table 1 Summary of Notations

Notation	Meaning
Φ_{B}, Φ_{b}, Φ_{U}	Homogeneous PPPs modeling the locations of BSs, blockages and users
λ_{B}, λ_{b}, λ_{U}	Densities of BSs, blockages and users
H, H_{b}, h	Heights of BSs, blockages and users
ℓ, ω, θ_{b}	Length, width and orientation of blockages
M, W	Mean values of blockage length and blockage width
μ	Parameter of the exponential distribution for blockage height
β	Path loss at reference distance
α	Path loss exponent
P	Transmit power of BSs
g	Power gain of Nakagami-m fading
m	Shape parameter of Nakagami-m fading
T	CP threshold
D	Horizontal distance from the typical user to its serving BS
θ_{tilt}	BS antenna downtilt
ϕ_{a}, ϕ_{e}	Half-power beamwidths in the azimuth plane and the elevation plane
$G_{\mathrm{A}}^{\mathrm{M}}$, $G_{\mathrm{A}}^{\mathrm{m}}$	Main-lobe gain and side-lobe gain of the BS antenna array
P_{M}, P_{m}	Probabilities of main-lobe gain and side-lobe gain
N_{B}	Number of BS antennas for the square BS antenna array
N_0	Additive white Gaussian noise
B_0	Serving BS for the typical user
Φ_{L}	Set of LOS BSs

point processes (PPPs) Φ_{B}, Φ_{b} and Φ_{U} with densities λ_{B}, λ_{b} and λ_{U}, respectively, on a 2D ground plane. It is assumed that the typical user is located at the origin O of the 2D ground plane. Assume that all the BSs are of the same height H and all the users are of the same height h with $H \geq h$. Each blockage is modeled as a cuboid, with a uniformly distributed length $\ell \sim U(0, 2M)$, where M is the mean value of blockage length, a uniformly distributed

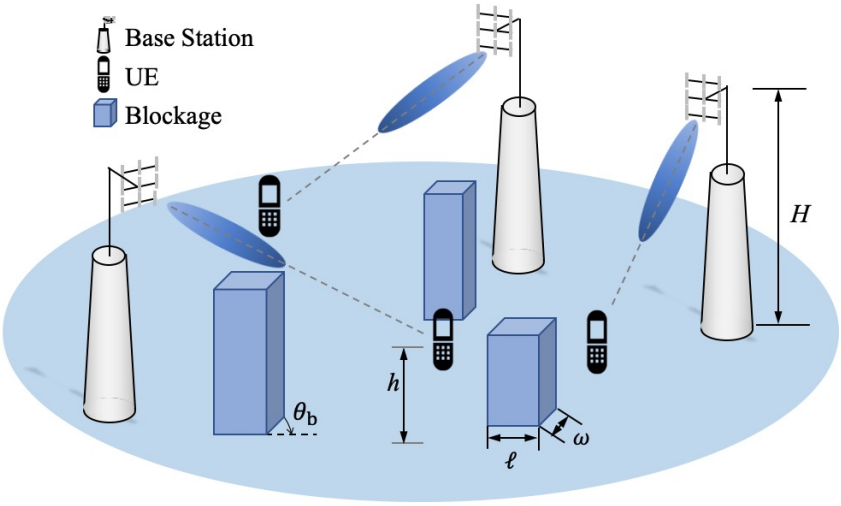

Fig. 1 An illustration of a 3D mmWave network.

width $\omega \sim U(0,2W)$, where W is the mean value of blockage width, a uniformly distributed orientation $\theta_b \sim U(0,2\pi)$, and a height H_b that follows Rayleigh distribution with mean value μ [20, 25]. We assume that each cell adopts orthogonal time/frequency division multiple access to eliminate the intra-cell interference in the DL. The used notations are listed in Table 1.

2.2 Channel Model

The channel model comprises path loss and Nakagami-m fading [21]. Denoting the horizontal distance between the typical user and a BS by d, the path loss of the link between the BS and the typical user is given by

$$l(d) = \beta \left[d^2 + (H-h)^2\right]^{-\alpha/2}, \tag{1}$$

where β is the path loss at the reference distance 1 m and α is the path loss exponent.

Denote the power gain of Nakagami-m fading by g, which is a random variable following the normalized Gamma distribution, i.e., $g \sim \Gamma(m, \frac{1}{m})$ with probability density function (PDF) $f_g(x) = \frac{m^m x^{m-1} e^{-mx}}{\Gamma(m)}$, where m is the shape parameter of Nakagami-m fading. For tractability, m is assumed to be an integer [11].

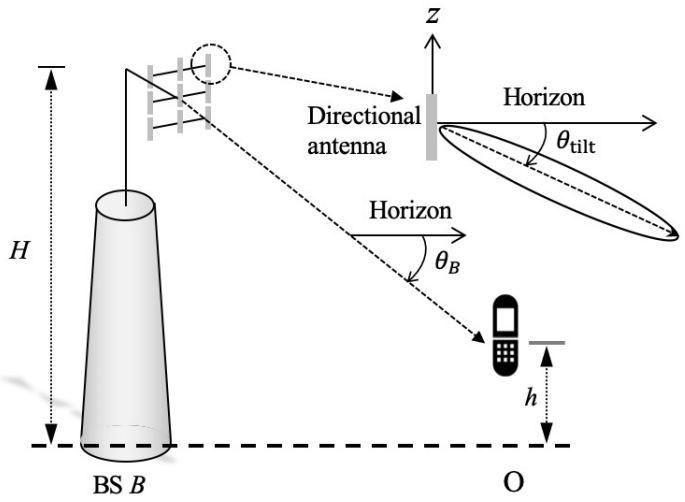

Fig. 2 An illustration of BS antenna array and antenna downtilt.

2.3 3D BS Antenna Pattern

As shown in Fig. 2, we assume that each small-cell BS adopts a uniform planar square array comprising N_{B} identical directional BS antennas and each user adopts an isotropic antenna. Each directional BS antenna consists of multiple vertically stacked radiating elements and the gain of each antenna depends on the number, the patterns and the relative positions of radiating elements [15]. Due to the excessive power consumption of RF chain components at mmWave frequencies, we adopt analog beamforming to provide directional beams, i.e., only one RF chain is used. The 3D BS antenna radiation pattern consists of two parts: the directional antenna radiation pattern and the antenna array radiation pattern [22], as described in the following.

1) Directional Antenna Radiation Pattern: Assuming that each radiating element at a directional BS antenna is an identical dipole, the radiation pattern of a directional BS antenna in dBi is given by [17, 23]

$$G_{\text{D}}(\theta_B, \theta_{\text{tilt}})^{\text{dBi}} = G_{\text{h}}^{\text{dBi}} + G_{\text{v}}(\theta_B, \theta_{\text{tilt}})^{\text{dBi}} + G_{\text{m}}^{\text{dBi}}, \tag{2}$$

where $G_{\text{h}}^{\text{dBi}} = 0$ dBi is the horizontal gain of a directional BS antenna, $G_{\text{v}}(\theta_B, \theta_{\text{tilt}})^{\text{dBi}}$ is the vertical gain of a directional BS antenna, which is referred to as the BS antenna downtilt gain hereafter, $\theta_B = \arctan(\frac{H-h}{r_B})$ is the elevation angle between the horizon and the line from BS B

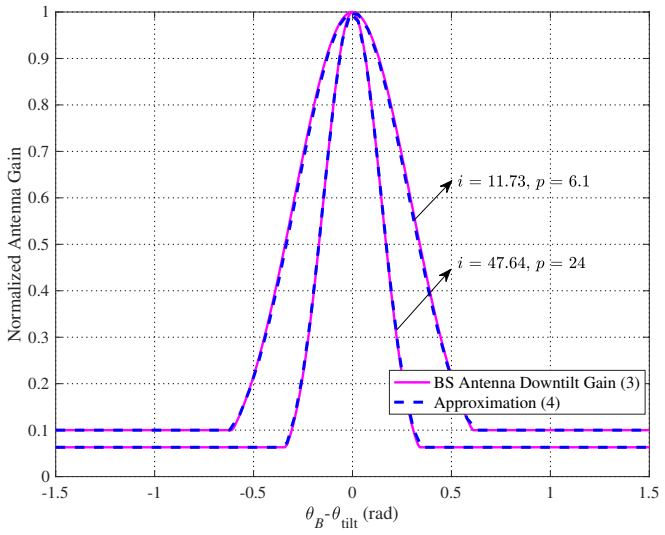

Fig. 3 BS antenna downtilt gain.

to the typical user, r_B is the horizontal distance from BS B to the typical user, $\theta_{\text{tilt}} \in (0, \frac{\pi}{2})$ is the BS antenna downtilt, which is assumed to be of the same value for all the antennas, and $G_{\text{m}}^{\text{dBi}}$ is the maximum directional BS antenna gain [23]. The actual BS antenna downtilt gain is $\frac{\sin^2\left[\frac{\pi N_{\text{dipole}}}{2}(\sin\theta_B - \sin\theta_{\text{tilt}})\right]}{N_{\text{dipole}}\sin^2\left[\frac{\pi}{2}(\sin\theta_B - \sin\theta_{\text{tilt}})\right]}$, where N_{dipole} is the number of dipoles per directional BS antenna. For analytical tractability, we adopt the widely used approximate BS antenna downtilt gain given in linear scale by [23]

$$G_{\text{v}}(\theta_B, \theta_{\text{tilt}}) = \max\left\{\cos^i(\theta_B - \theta_{\text{tilt}}), 10^{0.1F_{\text{V}}}\right\}, \tag{3}$$

where F_{V} is the vertical side-lobe level with respect to the main-lobe level of the directional BS antenna. If the directional BS antenna consists of two half-wave dipoles, $i = 11.73$, $F_{\text{V}} = -10$ dB and $G_{\text{m}}^{\text{dBi}} = 5.15$ dBi; if the directional BS antenna consists of four half-wave dipoles, $i = 47.64$, $F_{\text{V}} = -12$ dB and $G_{\text{m}}^{\text{dBi}} = 8.15$ dBi [23].

We note that the power of a cosine function in (3) will hinder the subsequent analysis. To remove the power of a cosine function from (3), we give the following remark.

Remark 1. *For the typical user, the BS antenna downtilt gain from BS B can be approximated by*

$$G_{\text{exp}}(\theta_B, \theta_{\text{tilt}}) = \max\left\{\exp\left\{-p\left(\theta_B - \theta_{\text{tilt}}\right)^2\right\}, 10^{0.1F_{\text{V}}}\right\}, \tag{4}$$

where the value of p can be obtained by curve fitting to (3).

Fig. 3 compares the approximate BS antenna downtilt gain in (3) and the approximation in (4), from which we can see that the gap between them is negligible.

2) Antenna Array Radiation Pattern: We adopt the 3D sectorized antenna array model [24], where the beamforming gains of a uniform planar square array comprising N_{B} isotropic antennas are considered to be a constant G_{A}^{M} in the main-lobe direction and a constant G_{A}^{m} in the side-lobe direction. We suppose that each BS knows the location information of all its associated users through dedicated beam training methods [14], and can align their beams to the users connected to them. Hence, the typical user obtains the main-lobe gain G_{A}^{M} from its serving BS. The beamforming gain from an interfering BS to the typical user can be calculated in linear scale as follows,

$$G_{\text{A}}(\phi_{\text{a}}, \phi_{\text{e}}) = \begin{cases} G_{\text{A}}^{\text{M}}, & P_{\text{M}} = \frac{\phi_{\text{a}}}{2\pi}\sin\left(\frac{\phi_{\text{e}}}{2}\right), \\ G_{\text{A}}^{\text{m}}, & P_{\text{m}} = 1 - P_{\text{M}}, \end{cases} \tag{5}$$

where ϕ_{a} and ϕ_{e} are half-power beamwidths generated by the antenna array in the azimuth direction and that in the elevation direction, respectively, P_{M} and P_{m} are the probabilities that the typical user is in the interfering BS's main-lobe direction or side-lobe direction, respectively. The values of parameters in (5) are dependent on N_{B} and are listed in Table 2 [24].

To sum up, when BS B is the serving BS, the 3D BS antenna gain between BS B and the typical user is expressed in linear scale as $G_{\text{S}}(\theta_B, \theta_{\text{tilt}}) = G_{\text{D}}(\theta_B, \theta_{\text{tilt}})G_{\text{A}}^{\text{M}}$; and when BS B is an interfering BS, the 3D BS antenna gain between BS B and the typical user is expressed in linear scale as $G_{\text{I}}(\theta_B, \theta_{\text{tilt}}, \phi_{\text{a}}, \phi_{\text{e}}) = G_{\text{D}}(\theta_B, \theta_{\text{tilt}})G_{\text{A}}(\phi_{\text{a}}, \phi_{\text{e}})$.

Table 2 Antenna Array Parameters [24]

Number of directional BS antennas N_{B}	$16, 36, 64, 100$
Half-power beamwidth $\phi_{\mathrm{a}} = \phi_{\mathrm{e}}$	$\frac{\sqrt{3}}{\sqrt{N_{\mathrm{B}}}}$
Main-lobe gain $G_{\mathrm{A}}^{\mathrm{M}}$	N_{B}
Side-lobe gain $G_{\mathrm{A}}^{\mathrm{m}}$	$\frac{\sqrt{N_{\mathrm{B}}} - \frac{\sqrt{3}}{2\pi} N_{\mathrm{B}} \sin\left(\frac{\sqrt{3}}{2\sqrt{N_{\mathrm{B}}}}\right)}{\sqrt{N_{\mathrm{B}}} - \frac{\sqrt{3}}{2\pi} \sin\left(\frac{\sqrt{3}}{2\sqrt{N_{\mathrm{B}}}}\right)}$

2.4 LOS Probability

Firstly, we analyze the horizontal LOS probability from a BS located at X with a horizontal distance r to the typical user located at the origin O on the 2D plane. The horizontal LOS probability is the probability that no blockage crosses OX. In line with [25], the number of blockages lying across OX is a Poisson random variable with a mean $\eta r + p$, where $\eta = \frac{2\lambda_{\mathrm{b}}[\mathbb{E}(\ell)+\mathbb{E}(\omega)]}{\pi} = \frac{2\lambda_{\mathrm{b}}(M+W)}{\pi}$ and $p = \lambda_{\mathrm{b}}\mathbb{E}(\ell)\mathbb{E}(\omega) = \lambda_{\mathrm{b}} MW$. Following the properties of Poisson distribution, the horizontal LOS probability can be computed as $\mathbb{P}(\eta r + p = 0) = e^{-(\eta r + p)}$.

Next, we analyze the 3D LOS probability between the BS located at X and the typical user. As shown in Fig. 4, for a blockage lying across OX at a horizontal distance t from the typical user, only if $H_{\mathrm{b}} > h_t$, where $h_t = \frac{hr+(H-h)t}{r}$, it will effectively block the 3D LOS path between the BS and the typical user. The conditional probability that a blockage blocks the path between the BS located at X and the typical user under the condition that it lies across OX can be derived following [25] as

$$\begin{aligned}
\varepsilon &= \frac{1}{r}\int_0^r \mathbb{P}\left[H_{\mathrm{b}} > h_t\right] \mathrm{d}t \\
&= \frac{1}{r}\int_0^r \left(1 - \int_0^{\frac{hr+(H-h)t}{r}} f_H(H_{\mathrm{b}}) \mathrm{d}H_{\mathrm{b}}\right) \mathrm{d}t \\
&= 1 - \frac{1}{r}\int_0^r \int_0^{\frac{hr+(H-h)t}{r}} \frac{\pi H_{\mathrm{b}}}{2\mu^2} e^{-\frac{\pi H_{\mathrm{b}}^2}{4\mu^2}} \mathrm{d}H_{\mathrm{b}} \mathrm{d}t \\
&= \frac{\mu\left[\mathrm{erf}\left(\frac{\sqrt{\pi}H}{2\mu}\right) - \mathrm{erf}\left(\frac{\sqrt{\pi}h}{2\mu}\right)\right]}{H-h},
\end{aligned} \tag{6}$$

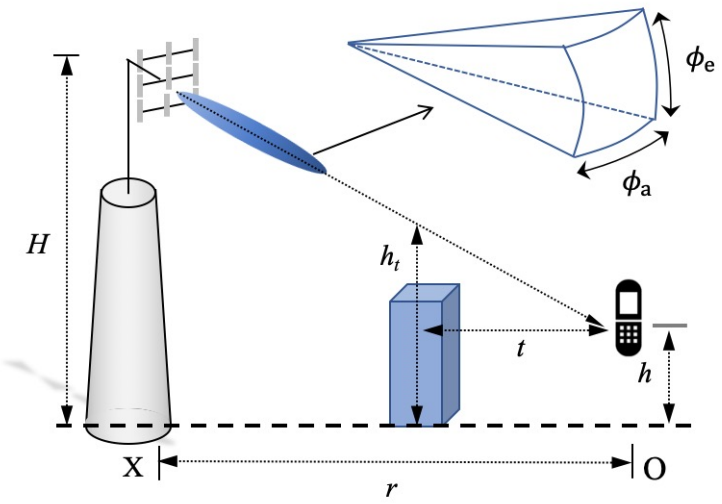

Fig. 4 An illustration of 3D blockage and array beamforming.

where $f_H(H_b)$ is the PDF of H_b and erf$(\cdot)$ is the error function. The number of blockages that effectively block the 3D LoS path can be obtained by thinning the number of blockages lying across OX by a factor ε, which is a Poisson random variable with a mean $\varepsilon(\eta r+p)$. Hence, the 3D LOS probability of the link between the BS at X and the typical user is given by $e^{-\varepsilon(\eta r+p)}$. Note that the analysis of the 3D LOS probability under the exponential distribution of blockage heights can be extended to other distributions of blockage heights following similar steps.

2.5 BS Association and SINR

The blockages are assumed to be impenetrable as mmWave signals experience very high penetration losses [14]. Under this assumption, both the desired signals and interfering signals come from the LOS BSs. For analytical tractability, we assume that each user connects to the nearest LOS BS.

Lemma 1. *Denoting the distance between the typical user and its serving BS by D, the PDF of D is given by* $f_D(x) = 2\pi\lambda_B x e^{-[\varepsilon(\eta x+p)+2\pi\lambda_B F(x)]}$, *where* $F(x) = \frac{e^{-\varepsilon p}}{(\varepsilon\eta)^2}[1-(\varepsilon\eta x+1)e^{-\varepsilon\eta x}]$.

Proof. The complementary cumulative distribution function (CCDF) of D is given by

$$\begin{aligned}\mathbb{P}(D>x) &\overset{(a)}{=} \exp\left\{-2\pi\lambda_{\mathrm{B}}\int_0^x e^{-\varepsilon(\eta r+p)} r\mathrm{d}r\right\}\\ &= e^{-2\pi\lambda_{\mathrm{B}}F(x)},\end{aligned} \tag{7}$$

where (a) is obtained using the void probability of PPP. Then the PDF of D can be derived as

$$f_D(x) = \frac{\mathrm{d}(1-\mathbb{P}(D>x))}{\mathrm{d}x} = 2\pi\lambda_{\mathrm{B}} x e^{-[\varepsilon(\eta x+p)+2\pi\lambda_{\mathrm{B}}F(x)]}. \tag{8}$$

□

For a given $D=x$, the signal-to-noise-plus-interference ratio (SINR) of the typical user is given by

$$\begin{aligned}\mathrm{SINR}(x) &= \frac{g_0 Pl(x) G_{\mathrm{S}}(\theta_{\mathrm{B}_0},\theta_{\mathrm{tilt}})}{\sum_{j\in\Phi_{\mathrm{L}}\setminus\mathrm{B}_0} g_j Pl(D_j) G_{\mathrm{I}}(\theta_{\mathrm{B}_j},\theta_{\mathrm{tilt}},\phi_{\mathrm{a}},\phi_{\mathrm{e}})+N_0}\\ &= \frac{g_0 Pl(x) G_{\mathrm{D}}(\theta_{\mathrm{B}_0},\theta_{\mathrm{tilt}}) G_{\mathrm{A}}^{\mathrm{M}}}{\sum_{j\in\Phi_{\mathrm{L}}\setminus\mathrm{B}_0} g_j Pl(D_j) G_{\mathrm{D}}(\theta_{\mathrm{B}_j},\theta_{\mathrm{tilt}}) G_{\mathrm{A}}(\phi_{\mathrm{a}},\phi_{\mathrm{e}})+N_0},\end{aligned} \tag{9}$$

where P is the transmit power of BSs assuming all BSs transmit the same power, g_0 and g_j are the Nakagami-m fading power gains from the serving BS B_0 and the interfering BS B_j to the typical user, respectively, D_j is the transmission distance between the typical user and B_j, Φ_{L} is the set of LOS BSs to the typical user, $G_{\mathrm{D}}(\theta_{\mathrm{B}_0},\theta_{\mathrm{tilt}}) = 10^{0.1G_{\mathrm{D}}(\theta_{\mathrm{B}_0},\theta_{\mathrm{tilt}})^{\mathrm{dBi}}}$, $G_{\mathrm{D}}(\theta_{\mathrm{B}_j},\theta_{\mathrm{tilt}}) = 10^{0.1G_{\mathrm{D}}(\theta_{\mathrm{B}_j},\theta_{\mathrm{tilt}})^{\mathrm{dBi}}}$, and N_0 is the power of additive white Gaussian noise.

By substituting (2) and (4) into (9), we have

$$\mathrm{SINR}(x) \approx \frac{g_0 l(x) G_{\exp}(\theta_{\mathrm{B}_0},\theta_{\mathrm{tilt}})}{\sum_{j\in\Phi_{\mathrm{L}}\setminus\mathrm{B}_0} g_j l(D_j) G_{\exp}(\theta_{\mathrm{B}_j},\theta_{\mathrm{tilt}}) G_{\mathrm{A}}^{\mathrm{I}}+\delta^2}, \tag{10}$$

where $G_{\mathrm{A}}^{\mathrm{I}} = \frac{G_{\mathrm{A}}^{\mathrm{M}}P_{\mathrm{M}}+G_{\mathrm{A}}^{\mathrm{m}}P_{\mathrm{m}}}{G_{\mathrm{A}}^{\mathrm{M}}}$, $\delta^2 = \frac{N_0}{G_{\mathrm{A}}^{\mathrm{M}}P10^{0.1G_{\mathrm{m}}^{\mathrm{dBi}}}}$.

3 Coverage Probability

In this section, we first derive the DL CP for a general 3D mmWave SCN and then give the expressions of DL CP for some special cases.

3.1 General 3D MmWave SCNs

The definition of CP is the probability that the SINR of the typical user is greater than a given threshold T, i.e.,

$$\mathrm{P_{COV}} = \mathbb{P}(\mathrm{SINR} > T), \tag{11}$$

Theorem 1. *The DL CP of a general 3D mmWave SCN is given by*

$$\mathrm{P_{COV}}(H,\lambda_{\mathrm{B}},\theta_{\mathrm{tilt}},T) \approx \sum_{n=1}^{m}(-1)^{n+1}\binom{m}{n}\int_0^{\infty}\exp\left\{\frac{-\zeta nT}{\mathrm{SNR}(x)} - 2\pi\lambda_{\mathrm{B}}\int_x^{\infty}Q(x,t)e^{-\varepsilon(\eta t+p)}t\mathrm{d}t\right\}f_D(x)\mathrm{d}x, \tag{12}$$

where

$$\begin{cases} \mathrm{SNR}(x) = \frac{l(x)G_{\exp}(x)}{\delta^2}, \\ Q(x,t) = 1 - \left[1 + \frac{\zeta nT G_{\mathrm{A}}^{\mathrm{I}} G_{\exp}(t)}{mG_{\exp}(x)}\left(\frac{x^2+(H-h)^2}{t^2+(H-h)^2}\right)^{\frac{\alpha}{2}}\right]^{-m}, \\ G_{\exp}(t) = \max\left\{\exp\left\{-p\left(\arctan\left(\frac{H-h}{t}\right) - \theta_{\mathrm{tilt}}\right)^2\right\}, 10^{0.1F_{\mathrm{V}}}\right\}, \\ G_{\exp}(x) = \max\left\{\exp\left\{-p\left(\arctan\left(\frac{H-h}{x}\right) - \theta_{\mathrm{tilt}}\right)^2\right\}, 10^{0.1F_{\mathrm{V}}}\right\}, \end{cases} \tag{13}$$

and $\zeta = m(m!)^{-\frac{1}{m}}$.

Proof. See Appendix A. □

Corollary 1. *The DL CP of a 3D mmWave SCN monotonically increases with the number of BS antennas N_{B}. When $N_{\mathrm{B}} \to \infty$, the asymptotic DL CP is given by*

$$\widehat{\mathrm{P}}_{\mathrm{COV}}(H, \lambda_{\mathrm{B}}, \theta_{\mathrm{tilt}}, T) \approx \sum_{n=1}^{m} (-1)^{n+1} \binom{m}{n} \int_0^{\infty} e^{-\frac{\zeta n T}{\mathrm{SNR}(x)}} f_D(x) \mathrm{d}x, \tag{14}$$

Proof. Recall that $G_{\mathrm{A}}^{\mathrm{I}} = \frac{G_{\mathrm{A}}^{\mathrm{M}} P_{\mathrm{M}} + G_{\mathrm{A}}^{\mathrm{m}} P_{\mathrm{m}}}{G_{\mathrm{A}}^{\mathrm{M}}}$. Using (5), $G_{\mathrm{A}}^{\mathrm{I}}$ can be rewritten as a function of N_{B} as $G_{\mathrm{A}}^{\mathrm{I}}(N_{\mathrm{B}}) = \frac{3}{2N_{\mathrm{B}}\pi^2} + \frac{1 - \frac{\sqrt{3N_{\mathrm{B}}}}{2\pi} \sin\left(\frac{\sqrt{3}}{2\sqrt{N_{\mathrm{B}}}}\right)}{N_{\mathrm{B}} - \frac{\sqrt{3N_{\mathrm{B}}}}{2\pi} \sin\left(\frac{\sqrt{3}}{2\sqrt{N_{\mathrm{B}}}}\right)} \left(1 - \frac{3}{2N_{\mathrm{B}}\pi^2}\right)$. It can be computed that $G_{\mathrm{A}}^{\mathrm{I}}{}'(N_{\mathrm{B}}) < 0$ for $N_{\mathrm{B}} \geq 1$, i.e, $G_{\mathrm{A}}^{\mathrm{I}}(N_{\mathrm{B}})$ monotonically decreases with N_{B}. From (10), it can be obtained that $\mathrm{SINR}(x)$ monotonically increases with N_{B}. Following the definition of CP in (11), it is straightforward that the CP monotonically increases with N_{B}. It can be seen that $G_{\mathrm{A}}^{\mathrm{I}} \to 0$ as $N_{\mathrm{B}} \to \infty$, and the expression of $\mathrm{SINR}(x)$ in (10) will reduce to $\mathrm{SNR(x)}$, which has been given in (12). □

To facilitate fast numerical evaluation, we derive a closed-form approximation of (12) using Gauss–Chebyshev integration in the next corollary.

Corollary 2. *The DL CP of a general 3D mmWave SCN can be approximated as*

$$\widetilde{\mathrm{P}}_{\mathrm{COV}}(H, \lambda_{\mathrm{B}}, \theta_{\mathrm{tilt}}, T) \approx \sum_{n=1}^{m} (-1)^{n+1} \binom{m}{n} \frac{\pi L}{2N_2} \sum_{q=1}^{N_2} \Delta(\varphi_q) \sqrt{1 - \varphi_q^2}, \tag{15}$$

where $\varphi_q = \cos\left(\frac{2q-1}{2N_2}\pi\right)$ is the Gauss-Chebyshev node, L and N_2 are the parameters of Gauss-Chebyshev integration set to large numbers, and $\Delta(\varphi_q)$ is given by

$$\Delta(\varphi_q) = \exp\Bigg\{ \frac{-\zeta n T}{\mathrm{SNR}\left(\frac{L\varphi_q}{2} + \frac{L}{2}\right)} - \frac{\pi^2 \lambda_{\mathrm{B}} \left(\frac{L}{2} - \frac{L\varphi_q}{2}\right)}{N_1} \times \sum_{k=1}^{N_1} \Lambda\left(\frac{L\varphi_q}{2} + \frac{L}{2}, \psi_k\right) \sqrt{1 - \psi_k^2} \Bigg\} f_D\left(\frac{L\varphi_q}{2} + \frac{L}{2}\right), \tag{16}$$

where $\psi_k = \cos\left(\frac{2k-1}{2N_1}\pi\right)$ *is the Gauss-Chebyshev node,* N_1 *is the parameter of Gauss-Chebyshev integration set to a large number, and*

$$\Lambda(y,z) = Q\left(y, \frac{L-y}{2}z + \frac{L+y}{2}\right) \exp\left\{-\varepsilon\eta\left(\frac{L-y}{2}z + \frac{L+y}{2}\right) - \varepsilon p\right\}\left(\frac{L-y}{2}z + \frac{L+y}{2}\right). \quad (17)$$

Proof. The approximation in (15) is derived following the Gauss–Chebyshev integration [26] and the integral transformation $\int_{\mathrm{a}}^{b} f(x)\mathrm{d}x = \frac{b-a}{2}\int_{-1}^{1} f\left(\frac{b-a}{2}t + \frac{b+a}{2}\right)\mathrm{d}t$. □

3.2 Ultra-dense 3D MmWave SCNs

When the SCN becomes ultra-dense, it is considered that the BS density is much greater than the blockage density. We assume that there is no self-blockage caused by BSs or human bodies, so all the BSs are LOS BSs to the typical user and the SCN becomes interference-limited [11, 27].

Theorem 2. *The DL CP of an ultra-dense 3D mmWave SCN is given by*

$$\mathrm{P}_{\mathrm{COV\_U}}(H, \lambda_{\mathrm{B}}, \theta_{\mathrm{tilt}}, T) \approx \sum_{n=1}^{m} (-1)^{n+1}\binom{m}{n}\int_0^{\infty} \exp\left\{-2\pi\lambda_{\mathrm{B}}\int_x^{\infty}(1 - F(x,t))\, t\mathrm{d}t\right\} f_d(x)\mathrm{d}x, \quad (18)$$

where $f_d(x) = 2\pi\lambda_{\mathrm{B}} x e^{-\pi\lambda_{\mathrm{B}}x^2}$, *and*

$$F(x,t) = \left[1 + \frac{\zeta n T G_{\mathrm{A}}^{\mathrm{I}} G_{\exp}(t)}{m G_{\exp}(x)}\left(\frac{x^2 + (H-h)^2}{t^2 + (H-h)^2}\right)^{\frac{\alpha}{2}}\right]^{-m}, \quad (19)$$

where ζ, $G_{\exp}(t)$, *and* $G_{\exp}(x)$ *have been given in Theorem 1.*

Proof. When the SCN becomes ultra-dense, the LOS probability from an arbitrary BS to the typical user will be 1, i.e., $\varepsilon = \eta = 0$ in Lemma 1. Plugging $\varepsilon = \eta = 0$ into (12), the expression of DL CP can be reduced to (18). □

3.3 Ultra-dense 3D MmWave SCNs with BS Arrays formed of Isotropic Antennas

In this section, we consider the special case that each BS is equipped with a uniform planar square array comprising N_{B} identical isotropic antennas, i.e., $G_{\mathrm{D}}(\theta_B, \theta_{\mathrm{tilt}})^{\mathrm{dBi}} = 0$ dBi, and present the following theorem to simplify the DL CP in (18) to a closed-form expression.

Theorem 3. *The DL CP of an ultra-dense 3D mmWave SCN where each BS adopts a uniform planar square array comprising N_{B} identical isotropic antennas is expressed as*

$$\mathrm{P}_{\mathrm{COV\_U}}(H, \lambda_{\mathrm{B}}, T) \approx \sum_{n=1}^{m} (-1)^{n+1} \binom{m}{n} \frac{e^{-\pi\lambda_{\mathrm{B}} K(m,n)(H-h)^2}}{K(m,n)+1}, \tag{20}$$

where $K(m,n) = {}_2F_1\left[-\frac{2}{\alpha}, m; 1-\frac{2}{\alpha}; -\frac{\zeta n T G_{\mathrm{A}}^{\mathrm{I}}}{m}\right] - 1$, and ${}_2F_1[\cdot]$ denotes the Gauss hypergeometric function.

Proof. See Appendix B. □

Corollary 3. *The DL CP of an ultra-dense 3D mmWave SCN where each BS adopts a uniform planar square array comprising N_{B} identical isotropic antennas is lower-bounded by*

$$\widehat{\mathrm{P}}_{\mathrm{COV\_U}}(H, \lambda_{\mathrm{B}}, T) = \frac{e^{-\pi\lambda_{\mathrm{B}} K(1,1)(H-h)^2}}{K(1,1)+1}, \tag{21}$$

which monotonically decreases with λ_{B} and $H (H > h)$.

Proof. It has been shown in [9] that the CP monotonically increases with m, and therefore $\widehat{\mathrm{P}}_{\mathrm{COV\_U}}(H, \lambda_{\mathrm{B}})$ can be obtained by substituting $m = 1$ into (20). The first derivative of $\widehat{\mathrm{P}}_{\mathrm{COV\_U}}(H, \lambda_{\mathrm{B}})$ with regard to λ_{B} can be computed as $\frac{\mathrm{d}\widehat{\mathrm{P}}_{\mathrm{COV\_U}}(H,\lambda_{\mathrm{B}})}{\mathrm{d}\lambda_{\mathrm{B}}} = \frac{-\pi K(H-h)^2 e^{-\pi\lambda_{\mathrm{B}} K(1,1)(H-h)^2}}{K(1,1)+1} < 0$. Likewise, $\frac{\mathrm{d}\widehat{\mathrm{P}}_{\mathrm{COV\_U}}(H,\lambda_{\mathrm{B}})}{\mathrm{d}H} = \frac{-2\pi\lambda_{\mathrm{B}} K(1,1)(H-h) e^{-\pi\lambda_{\mathrm{B}} K(1,1)(H-h)^2}}{K+1} < 0$. □

(20) is based on the property that the CDF of a gamma random variable g with parameter m is tightly approximated by $\mathbb{P}(g < x) > \left(1 - e^{-\zeta x}\right)^m$, where $x > 0$ and $\zeta = m(m!)^{-\frac{1}{m}}$ [28]. Next, we derive the exact expression of the DL CP for an ultra-dense 3D mmWave SCN where each BS adopts a uniform planar square array comprising N_{B} identical isotropic antennas.

Theorem 4. *The exact DL CP of an ultra-dense 3D mmWave SCN where each BS is equipped with a uniform planar square array comprising N_{B} identical isotropic antennas is given by*

$$\overline{\mathrm{P}}_{\mathrm{COV\_U}}(H,\lambda_{\mathrm{B}},T)=\sum_{k=0}^{m-1}\int_0^{\infty}\frac{(-s)^k}{k!}e^{\rho(s,x)}\mathscr{B}_k\left(\frac{\mathrm{d}}{\mathrm{d}s}\rho(s,x),\frac{\mathrm{d}^2}{\mathrm{d}s^2}\rho(s,x)\ldots\frac{\mathrm{d}^k}{\mathrm{d}s^k}\rho(s,x)\right)f_d(x)\mathrm{d}x, \tag{22}$$

where $s=TG_{\mathrm{A}}^{\mathrm{I}}/l(x)$, $f_d(x)=2\pi\lambda_{\mathrm{B}}xe^{-\pi\lambda_{\mathrm{B}}x^2}$, $\mathscr{B}_k(\cdot)$ is the kth complete Bell polynomial,

$$\rho(s,x)=-2\pi\lambda_{\mathrm{B}}\int_x^{\infty}\left(1-\left(1+\frac{s}{m}l(t)\right)^{-m}\right)\mathrm{d}t, \tag{23}$$

and

$$\frac{\mathrm{d}^k}{\mathrm{d}s^k}\rho(s,x)=-2\pi\lambda_{\mathrm{B}}\int_x^{\infty}\frac{\mathrm{d}^k}{\mathrm{d}s^k}\tau(s,t)\mathrm{d}t, \tag{24}$$

where

$$\frac{\mathrm{d}^k}{\mathrm{d}s^k}\tau(s,t)=(-1)^{k-1}\frac{\Gamma(m+k)}{\Gamma(m)m^k}\left(1+\frac{s}{m}l(t)\right)^{-m-k}l^k(t). \tag{25}$$

Proof. See Appendix C. □

4 Area Spectral Efficiency

In this section, we analyze the performance of the 3D mmWave SCN with respect to ASE, which is defined as the average spectral efficiency per unit area. As per [29], the expression of ASE in bps/Hz/m^2 is given by

$$A(\lambda_{\mathrm{B}})=\lambda_{\mathrm{B}}\log_2(1+T)\mathrm{P}_{\mathrm{COV}}(H,\lambda_{\mathrm{B}},\theta_{\mathrm{tilt}},T), \tag{26}$$

where $\log_2(1+T)\mathrm{P}_{\mathrm{COV}}(H,\lambda_{\mathrm{B}},\theta_{\mathrm{tilt}},T$ is the average throughput per cell.

Corollary 4. *The ASE of an ultra-dense 3D mmWave SCN with isotropic BS antennas is lower-bounded by*

$$\widehat{A}_{\mathrm{U}}(\lambda_{\mathrm{B}}) = \frac{\lambda_{\mathrm{B}}\log_2(1+T)e^{-\pi\lambda_{\mathrm{B}}K(1,1)(H-h)^2}}{K(1,1)+1}, \tag{27}$$

which first grows and then degrades with λ_{B}, and the optimal λ_{B} that maximizes $\widehat{A}_{\mathrm{U}}(\lambda_{\mathrm{B}})$ is $\lambda_{\mathrm{B}}^{*} = \frac{1}{\pi K(1,1)(H-h)^2}$.

Proof. Substituting $\widehat{\mathrm{P}}_{\mathrm{COV\_U}}(H,\lambda_{\mathrm{B}})$ into (26), $\widehat{A}_{\mathrm{U}}(\lambda_{\mathrm{B}})$ can be obtained. The first derivative of $\widehat{A}_{\mathrm{U}}(\lambda_{\mathrm{B}})$ can be computed as $\frac{\mathrm{d}\widehat{A}_{\mathrm{U}}(\lambda_{\mathrm{B}})}{\mathrm{d}\lambda_{\mathrm{B}}} = \frac{\log_2(1+T)e^{-\pi\lambda_{\mathrm{B}}K(1,1)(H-h)^2}\left(1-\pi\lambda_{\mathrm{B}}K(1,1)(H-h)^2\right)}{K(1,1)+1}$. When $\lambda_{\mathrm{B}} < \frac{1}{\pi K(1,1)(H-h)^2}$, $\frac{\mathrm{d}\widehat{A}_{\mathrm{U}}(\lambda_{\mathrm{B}})}{\mathrm{d}\lambda_{\mathrm{B}}} > 0$, and When $\lambda_{\mathrm{B}} > \frac{1}{\pi K(1,1)(H-h)^2}$, $\frac{\mathrm{d}\widehat{A}_{\mathrm{U}}(\lambda_{\mathrm{B}})}{\mathrm{d}\lambda_{\mathrm{B}}} < 0$. Hence, $\widehat{A}_{\mathrm{U}}(\lambda_{\mathrm{B}})$ first grows and then degrades with λ_{B}, and the optimal λ_{B} that maximizes $\widehat{A}_{\mathrm{U}}(\lambda_{\mathrm{B}})$ is $\frac{1}{\pi K(1,1)(H-h)^2}$. □

5 Numerical Results

In this section, numerical results for the DL CP and the ASE in the 3D mmWave SCN are presented. Before system analysis, we verify the analytical results through Monte-Carlo simulations on a 1km×1km area with 10^5 random trials. The default numerical simulation parameters are given in Table 3 [12, 23, 25].

5.1 Validation of the Analytical Results

In Fig. 5, we show the effects of the number of BS antennas. For the analytical results, we analyze the DL CP using Theorem 1 with our proposed exponential expression of the BS antenna downtilt gain. It can be observed that our analytical results match with Monte-Carlo simulation curves exactly, which verifies the accuracy of our analytical results. Moreover, we can see that a larger number of antenna array elements leads to a higher DL CP, which is in line with our conclusion in Corollary 1. In Fig. 6, we can see that 3D mmWave SCNs can provide higher CP than 2D mmWave SCNs due to the BS antenna downtilt gain.

Table 3 Values of Parameters

Parameter	Default Value
Height of BSs H	5 m
Height of users h	1 m
Density of BSs λ_{B}	10^{-3} BS/m^2
Density of blockages λ_{b}	10^{-3} blockage/m^2
Path loss exponent α	2
Number of BS antennas for the square BS antenna array N_{B}	36
Parameters of the directional BS antenna i, F_{V}, $G_{\mathrm{m}}^{\mathrm{dBi}}$	47.64, -12 dB, 8.15 dBi
Transmit power of BSs P	33 dBm
Additive white Gaussian noise N_0	-74 dBm
CP threshold T	10 dB
Mean value of blockage length M	15 m
Mean value of blockage width W	15 m
Mean value of blockage height μ	10 m
Parameters of Gauss-Chebyshev integration L, N_1, N_2	3000, 600, 600
Path loss at the reference distance β	-61.4 dB
Shape parameter of small scale fading m	3
BS antenna downtilt θ_{tilt}	$\pi/6$

5.2 Effects of BS Height and BS Antenna Downtilt

In Fig. 7, we show the DL CP against the BS height for different values of λ_{b}. When the SCN is ultra-dense, the number of blockages is negligible, and the DL CP first grows to a peak and then degrades with the BS height. This is because for the BS antenna downtilt ($\theta_{\mathrm{tilt}} = \pi/6$) in our evaluation, the directional BS antenna gain first grows to a peak and then degrades with the BS height. Moreover, the decrease of DL CP is also due to more inter-cell interference caused by the larger BS height, which has been demonstrated in [8]. From the $\lambda_{\mathrm{b}} = 5\lambda_{\mathrm{B}}$, $\lambda_{\mathrm{b}} = 10\lambda_{\mathrm{B}}$ and $\lambda_{\mathrm{b}} = 15\lambda_{\mathrm{B}}$ curves, we can see that the optimal BS height that maximizes the directional BS antenna gain increases with the increasing blockage density. However, for the $\lambda_{\mathrm{b}} = 30\lambda_{\mathrm{B}}$ case, the DL CP falls victim to excessive blockages. The DL CP first grows with the BS height because a larger BS height provides a higher LOS probability for the desired signal.

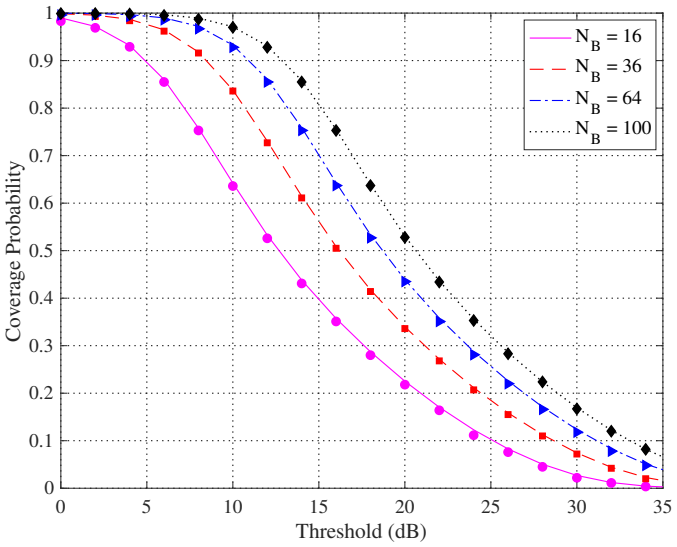

Fig. 5 CP versus T. Lines and markers denote analytical results and simulation results, respectively.

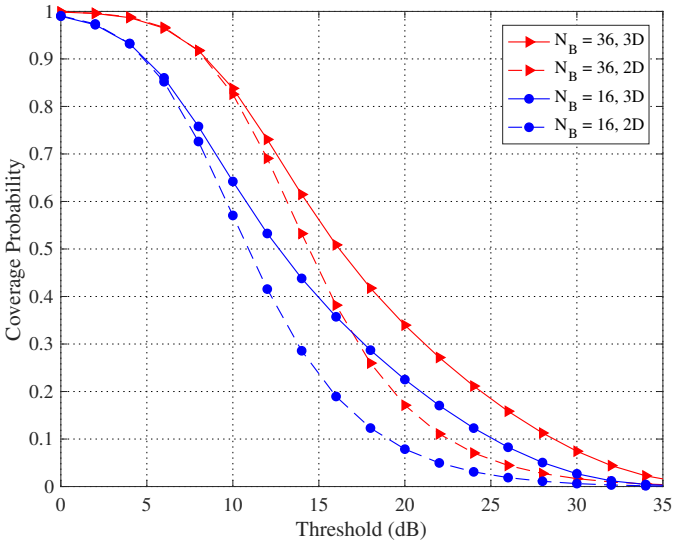

Fig. 6 CP versus T for 3D and 2D mmWave SCNs.

In Fig. 8, we show the DL CP against the BS height for different values of θ_{tilt}. From (3), the BS height that maximizes the directional BS antenna gain increases with θ_{tilt}. Specifically, for the $\theta_{\text{tilt}} = 0$ case, the BS height that maximizes the directional BS antenna gain is 1 m, and therefore, no DL CP gain can be obtained through increasing the BS height. The DL CP monotonically decreases with the BS height since a larger BS height leads to a larger inter-cell

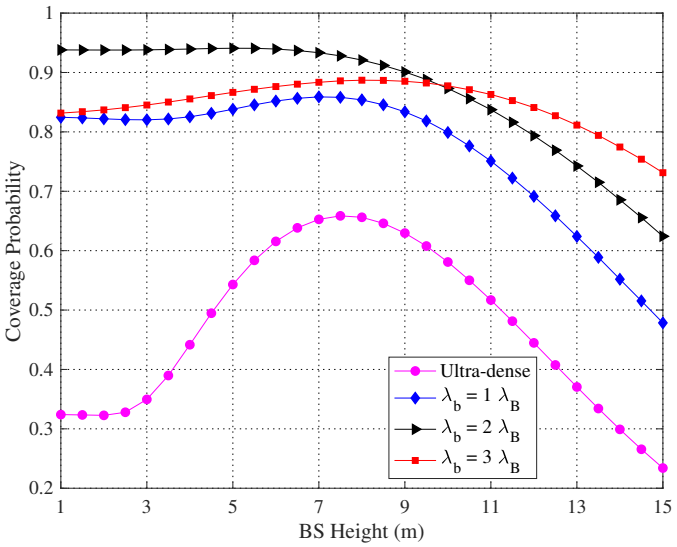

Fig. 7 CP versus H for different values of λ_{b}.

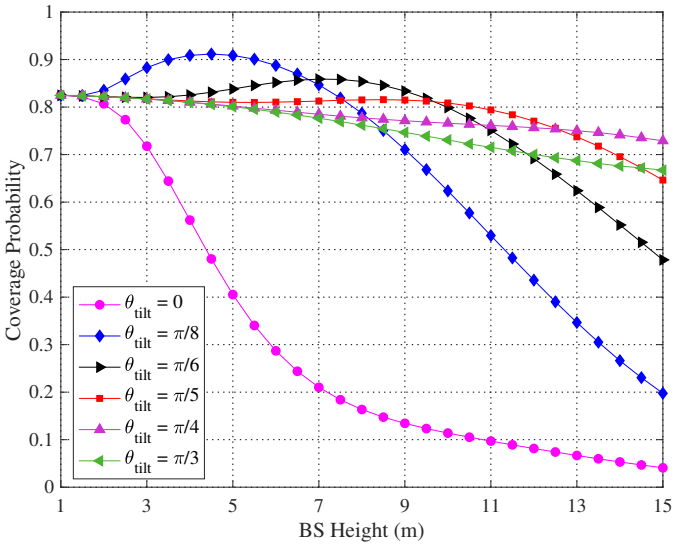

Fig. 8 CP versus H for different values of θ_{tilt}.

interference. For the $\theta_{\mathrm{tilt}} = \pi/2$ case, the DL CP monotonically decreases because the BS height that maximizes the directional BS antenna gain goes to infinity, and the loss resulted from the larger BS height always exceeds the directional BS antenna gain. For other cases, the DL CP first decreases and then increases with the BS height.

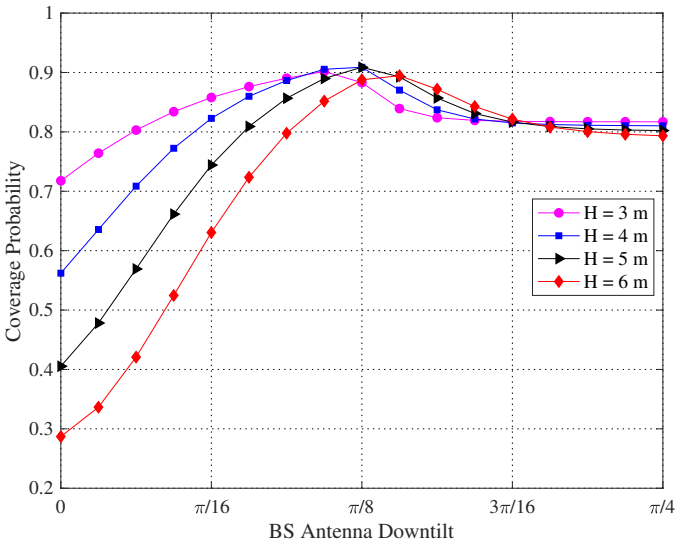

Fig. 9 CP versus θ_{tilt} for different values of H.

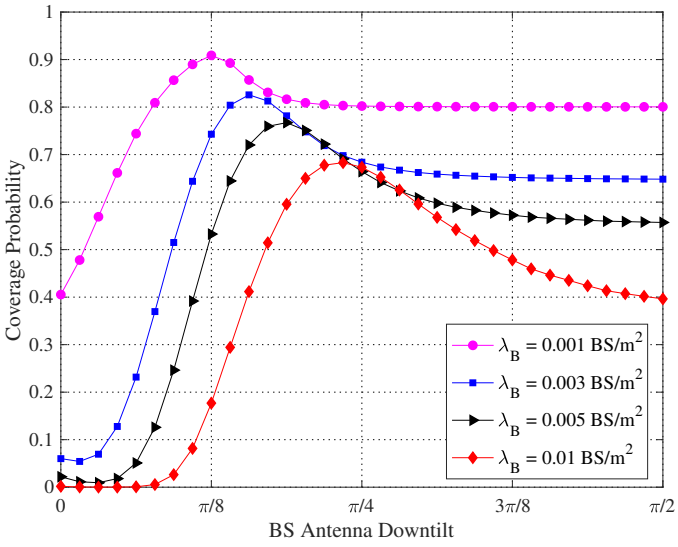

Fig. 10 CP versus θ_{tilt} for different values of λ_{B}.

In Fig. 9 and Fig. 10, we depict the DL CP against the BS antenna downtilt. From Fig. 9, we can observe that the DL CP first grows to a peak and then degrades with the BS antenna downtilt, and that a larger BS height brings a larger optimal BS antenna downtilt that maximizes the DL CP. From Fig. 10, it is observed that the optimal BS antenna downtilt that maximizes

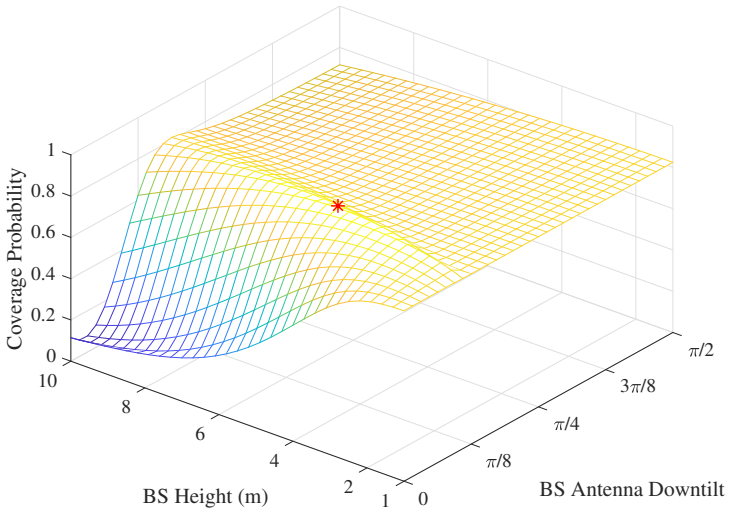

Fig. 11 Effects of H and θ_{tilt} on the CP. The marker denotes the maximum CP.

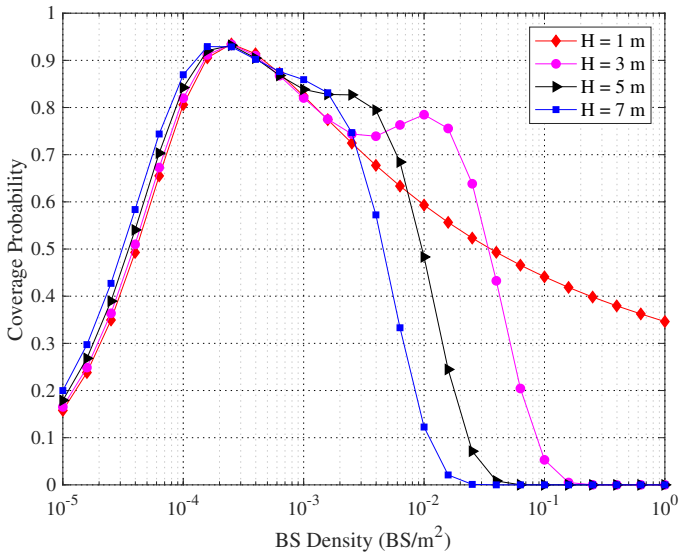

Fig. 12 CP versus λ_{B} for different values of H.

the DL CP increases with λ_{B}. This is because a larger λ_{B} results in a smaller distance between the serving BS and the typical user.

Fig. 11 shows the joint effects of BS height and BS antenna downtilt on the DL CP. For given BS density, blockage density, user height and distribution of blockage heights, the BS

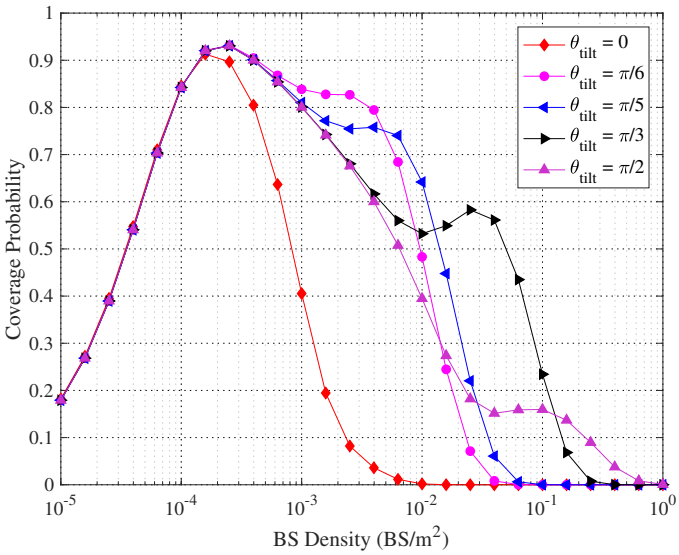

Fig. 13 CP versus λ_B for different values of θ_{tilt}.

height and the BS antenna downtilt can be jointly optimized to maximize the DL CP using Theorem 1.

5.3 Effect of BS Density

In Fig. 12, we display the effect of the BS density on the DL CP for different values of H. When $H = 1$ m, the directional BS antenna gain remains unchanged, and the DL CP first grows to a peak and then degrades with the BS density. This is because excessive blockages degrade the DL CP by blocking the desired signal, while moderate blockages improve the DL CP by reducing the inter-cell interference. For the $H > 1$ m cases, two peaks can be observed. The first peak can be explained for the same reason as in the $H = 1$ m case, and the second peak is due to the increase of directional BS antenna gain.

In Fig. 13, we display the effect of the BS density on the DL CP for different values of θ_{tilt}. When $\theta_{tilt} = 0$, the directional BS antenna gain is negligible and the DL CP first grows to a peak and then degrades with the BS density, which can be explained for the same reason as in the $H = 1$ m case in Fig. 11. When $\theta_{tilt} > 0$, the DL CP shows the second peak or a slower decrease due to the increase of directional BS antenna gain.

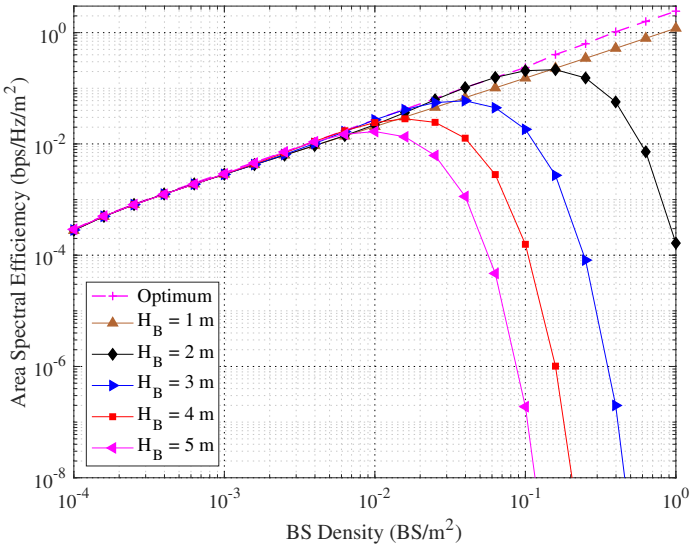

Fig. 14 ASE versus λ_{B} for different values of H.

5.4 Area Spectral Efficiency

In Fig. 14, we show the ASE for different values of H. The dashed line represents the ASE with jointly optimized H and θ_{tilt}, while the solid lines represent the ASE with the default θ_{tilt}. From the solid lines, we can see that the ASE scales linearly with the BS density when the BS height equals to the user height. However, when $H > 1$ m, the ASE first grows to a peak and then degrades with the BS density, which matches the trends of coverage probabilities in Fig. 12. The dashed line always exceeds the solid lines, indicating the importance of the joint optimization of H and θ_{tilt}.

6 Conclusions

In this paper, we have proposed a novel and tractable stochastic geometry framework for the performance evaluation of 3D mmWave SCNs. The effects of 3D blockages and the 3D BS antenna radiation pattern were characterized. We have analytically derived the integral-form expressions of the DL CP and ASE, and obtained the closed-form expressions in some special cases. The numerical results show that 3D mmWave SCNs can provide higher DL CP than 2D mmWave SCNs thanks to the BS antenna downtilt gain. Moreover, for given BS density,

blockage density, user height and distribution of blockage heights, the BS height and the BS antenna downtilt can be jointly optimized to obtain the maximum DL CP and ASE. These findings provide valuable insights into the deployment of 3D SCNs in mmWave bands.

In the future, we will extend the proposed framework to heterogeneous mmWave SCNs and investigate more sophisticated interference management techniques.

Appendix A

Plugging (10) into (11), we have

$$\begin{aligned}
&\mathrm{P}_{\mathrm{COV}}(H,\lambda_{\mathrm{B}},\theta_{\mathrm{tilt}})\\
&\approx\mathbb{E}_x\left[\mathbb{P}\left[\frac{g_0 l(x)G_{\exp}(\theta_{\mathrm{B}_0},\theta_{\mathrm{tilt}})}{\sum_{j\in\Phi_{\mathrm{L}}\setminus\mathrm{B}_0} g_j l(D_j)G_{\exp}(\theta_{\mathrm{B}_j},\theta_{\mathrm{tilt}})G_{\mathrm{A}}^{\mathrm{I}}+\delta^2}>T\right]\right]\\
&=\int_0^\infty \mathbb{P}\left[g_0>Tl^{-1}(x)G_{\exp}^{-1}(\theta_{\mathrm{B}_0},\theta_{\mathrm{tilt}})\left(\delta^2+\sum_{j\in\Phi_{\mathrm{L}}\setminus\mathrm{B}_0} g_j l(D_j)G_{\exp}(\theta_{\mathrm{B}_j},\theta_{\mathrm{tilt}})G_{\mathrm{A}}^{\mathrm{I}}\right)\right] f_D(x)\mathrm{d}x.
\end{aligned} \tag{28}$$

Defining $\sum_{j\in\Phi_{\mathrm{L}}\setminus\mathrm{B}_0} g_j l(D_j)G_{\exp}(\theta_{\mathrm{B}_j},\theta_{\mathrm{tilt}})G_{\mathrm{A}}^{\mathrm{I}}=I$, we have

$$\begin{aligned}
&\mathbb{P}\left[g_0>Tl^{-1}(x)G_{\exp}^{-1}(\theta_{\mathrm{B}_0},\theta_{\mathrm{tilt}})\left(\delta^2+I\right)\right]\\
&\overset{(a)}{<}1-\mathbb{E}\left[\left(1-e^{-\zeta Tl^{-1}(x)G_{\exp}^{-1}(\theta_{\mathrm{B}_0},\theta_{\mathrm{tilt}})\left(\delta^2+I\right)}\right)^m\right]\\
&\overset{(b)}{=}\sum_{n=1}^{m}(-1)^{n+1}\binom{m}{n}\mathbb{E}\left[e^{-\zeta nTl^{-1}(x)G_{\exp}^{-1}(\theta_{\mathrm{B}_0},\theta_{\mathrm{tilt}})\left(\delta^2+I\right)}\right],
\end{aligned} \tag{29}$$

where (a) is achieved using the approximation that for a gamma random variable g with parameter m, $\mathbb{P}(g>x)$ is tightly approximated by $\mathbb{P}(g>x)<\left(1-e^{-\zeta x}\right)^m$, in which $x>0$ and $\zeta=m(m!)^{-\frac{1}{m}}$ [28]. (b) is derived following Binomial series expansion. Denoting

$G_{\exp}(\theta_{\mathrm{B}_0},\theta_{\mathrm{tilt}})$ as $G_{\exp}(x)=\max\left\{\exp\left\{-p\left(\arctan\left(\frac{H-h}{x}\right)-\theta_{\mathrm{tilt}}\right)^2\right\},10^{0.1F_{\mathrm{V}}}\right\}$, we have

$$\begin{aligned}&\mathbb{E}\left[e^{-\zeta nTl^{-1}(x)G_{\exp}^{-1}(\theta_{\mathrm{B}_0},\theta_{\mathrm{tilt}})\left(\delta^2+I\right)}\right]\\&=e^{-\zeta nTl^{-1}(x)G_{\exp}^{-1}(x)\delta^2}\mathbb{E}\left[e^{-\zeta nTl^{-1}(x)G_{\exp}^{-1}(x)I}\right],\end{aligned}\tag{30}$$

where

$$\begin{aligned}&\mathbb{E}\left[e^{-\zeta nTl^{-1}(x)G_{\exp}^{-1}(x)I}\right]\\&=\mathbb{E}\left[e^{-\zeta nTl^{-1}(x)G_{\exp}^{-1}(x)\sum_{j\in\Phi_{\mathrm{L}}\setminus\mathrm{B}_0}g_jl(D_j)G_{\exp}(\theta_{\mathrm{B}_j},\theta_{\mathrm{tilt}})G_{\mathrm{A}}^{\mathrm{I}}}\right]\\&\overset{(a)}{=}\exp\left\{-2\pi\lambda_{\mathrm{B}}\int_x^{\infty}\left(1-\mathbb{E}_g\left[e^{-\frac{\zeta nTgl(t)G_{\exp}(t)G_{\mathrm{A}}^{\mathrm{I}}}{l(x)G_{\exp}(x)}}\right]\right)e^{-\varepsilon\eta t}t\mathrm{d}t\right\}\\&\overset{(b)}{=}\exp\left\{-2\pi\lambda_{\mathrm{B}}\int_x^{\infty}\left[1-\left[1+\frac{\zeta nTl(t)G_{\mathrm{A}}^{\mathrm{I}}G_{\exp}(t)}{ml(x)G_{\exp}(x)}\right]^{-m}\right]e^{-\varepsilon\eta t}t\mathrm{d}t\right\},\end{aligned}\tag{31}$$

where $G_{\exp}(t)=\max\left\{e^{-p\left(\arctan\left(\frac{H-h}{t}\right)-\theta_{\mathrm{tilt}}\right)^2},10^{0.1F_{\mathrm{V}}}\right\}$, (a) comes from the probability generating functional of homogeneous PPP and (b) comes from the MGF of the gamma random variable g.

Appendix B

For ultra-dense SCNs with isotropic BS antennas, $G_{\mathrm{D}}(\theta_B,\theta_{\mathrm{tilt}})^{\mathrm{dBi}}=G_{\mathrm{m}}^{\mathrm{dBi}}$. Substituting $G_{\exp}(x)=G_{\exp}(t)=1$ into (18), the DL CP can be computed as

$$\mathrm{P}_{\mathrm{COV\_U}}(H,\lambda_{\mathrm{B}})\approx\sum_{n=1}^{m}(-1)^{n+1}\binom{m}{n}\int_0^{\infty}\exp\left\{-2\pi\lambda_{\mathrm{B}}\int_x^{\infty}(1-Z(x,t))\,t\mathrm{d}t\right\}f_d(x)\mathrm{d}x,\tag{32}$$

where

$$Z(x,t)=\left[1+\frac{\zeta nTG_{\mathrm{A}}^{\mathrm{I}}}{m}\left(\frac{x^2+(H-h)^2}{t^2+(H-h)^2}\right)^{\frac{\alpha}{2}}\right]^{-m}.\tag{33}$$

By employing the integral $\int_{\mathrm{a}}^{\infty}\left(1-\left(1+\frac{s}{y^{-\alpha}}\right)^{-m}\right)y\mathrm{d}y=\frac{a^2}{2}\left({}_2F_1\left[-\frac{2}{\alpha},m;1-\frac{2}{\alpha};-\frac{s}{a^{\alpha}}\right]-1\right)$, we have

$$\int_x^{\infty}(1-Z(x,t))\,t\mathrm{d}t=\frac{x^2+(H-h)^2}{2}\left({}_2F_1\left[-\frac{2}{\alpha},m;1-\frac{2}{\alpha};-\frac{\zeta nTG_{\mathrm{A}}^{\mathrm{I}}}{m}\right]-1\right). \tag{34}$$

Plugging (34) into (32), (20) can be obtained through simple integral calculation.

Appendix C

For ultra-dense SCNs where each BS adopts a uniform planar square array comprising N_{B} identical isotropic antennas, (28) reduces to

$$\begin{aligned}
&\overline{\mathrm{P}}_{\mathrm{COV_U}}(H,\lambda_{\mathrm{B}})\\
&=\mathbb{E}_x\left[\mathbb{P}\left[\frac{g_0 l(x)}{\sum_{j\in\Phi_{\mathrm{L}}\setminus\mathrm{B}_0}g_j l(D_j)G_{\mathrm{A}}^{\mathrm{I}}}>T\right]\right]\\
&=\int_0^{\infty}\mathbb{P}\left[g_0>Tl^{-1}(x)\sum_{j\in\Phi_{\mathrm{L}}\setminus\mathrm{B}_0}g_j l(D_j)G_{\mathrm{A}}^{\mathrm{I}}\right)\Bigg]f_d(x)\mathrm{d}x\\
&\overset{(a)}{=}\sum_{k=0}^{m-1}\int_0^{\infty}\left[\frac{(-s)^k}{k!}\frac{\mathrm{d}^k}{\mathrm{d}s^k}e^{\rho(s,x)}\right]f_d(x)\mathrm{d}x,
\end{aligned} \tag{35}$$

where $\rho(s,x)=-2\pi\lambda_{\mathrm{B}}\int_x^{\infty}\left(1-\left(1+\frac{s}{m}l(t)\right)^{-m}\right)\mathrm{d}t$ and $s=TG_{\mathrm{A}}^{\mathrm{I}}/l(x)$. (a) comes from the CCDF of the gamma random variable g_0, which is expressed as $C(x)=e^{-mx}\sum_{k=0}^{m-1}\frac{(mx)^k}{k!}$ [14]. The k-th derivative of $e^{\rho(s,x)}$ can be expressed as a special case of Faà di Bruno's formula [30], i.e.,

$$\frac{\mathrm{d}^k}{\mathrm{d}s^k}e^{\rho(s,x)}=e^{\rho(s,x)}\mathscr{B}_k\left(\frac{\mathrm{d}}{\mathrm{d}s}\rho(s,x),\frac{\mathrm{d}^2}{\mathrm{d}s^2}\rho(s,x)\ldots\frac{\mathrm{d}^k}{\mathrm{d}s^k}\rho(s,x)\right). \tag{36}$$

Defining $\tau(s,t)=1-\left(1+\frac{s}{m}l(t)\right)^{-m}$, we have

$$\frac{\mathrm{d}^k}{\mathrm{d}s^k}\rho(s,x)=-2\pi\lambda_{\mathrm{B}}\int_x^{\infty}\frac{\mathrm{d}^k}{\mathrm{d}s^k}\tau(s,t)\mathrm{d}t, \tag{37}$$

where

$$\frac{\mathrm{d}^k}{\mathrm{d}s^k}\tau(s,t) = (-1)^{k-1}\frac{\Gamma(m+k)}{\Gamma(m)m^k}\left(1+\frac{s}{m}l(t)\right)^{-m-k} l^k(t). \tag{38}$$

Acknowledgment

This project has received funding from the European Union's Horizon 2020 Research and Innovation Program under Grants 766231 and 734798.

References

[1] J. G. Andrews *et al*., "What will 5G be?" *IEEE J. Sel. Areas Commun.*, vol. 32, no. 6, pp. 1065-1082, Jun. 2014.

[2] T. S. Rappaport *et al*., "Wireless communications and applications above 100 GHz: opportunities and challenges for 6G and beyond," *IEEE Access*, vol. 7, pp. 78729-78757, 2019.

[3] D. López-Pérez, M. Ding, H. Claussen, and A. H. Jafari, "Towards 1 Gbps/UE in cellular systems: Understanding ultra-dense small cell deployments," *IEEE Commun. Surveys Tuts.*, vol. 17, no. 4, pp. 2078–2101, 4th Quart. 2015.

[4] M. Kamel, W. Hamouda and A. Youssef, "Ultra-dense networks: a survey," *IEEE Commun. Surveys Tut.,* vol. 18, no. 4, pp. 2522-2545, Fourthquarter 2016.

[5] J. G. Andrews, X. Zhang, G. D. Durgin and A. K. Gupta, "Are we approaching the fundamental limits of wireless network densification?" *IEEE Commun. Mag.,* vol. 54, no. 10, pp. 184-190, Oct. 2016.

[6] T. Bai, A. Alkhateeb and R. W. Heath, "Coverage and capacity of millimeter-wave cellular networks," *IEEE Commun. Mag.,* vol. 52, no. 9, pp. 70-77, Sept. 2014.

[7] M. Shafi *et al*., "5G: A tutorial overview of standards, trials, challenges, deployment, and practice," *IEEE J. Sel. Areas Commun.,* vol. 35, no. 6, pp. 1201-1221, Jun. 2017.

[8] M. Ding and D. López-Pérez, “Performance impact of base station antenna heights in dense cellular networks,” *IEEE Trans. Wireless Commun.,* vol. 16, no. 12, pp. 8147-8161, Dec. 2017.

[9] I. Atzeni, J. Arnau, and M. Kountouris, “Downlink cellular network analysis with LOS/NLOS propagation and elevated base stations,” *IEEE Trans. Wireless Commun.*, vol. 17, no. 1, pp. 142-156, Jan. 2018.

[10] Q. Nadeem, A. Kammoun and M. Alouini, “Elevation beamforming with full dimension MIMO architectures in 5G systems: A tutorial,” *IEEE Commun. Surveys Tuts.*, vol. 21, no. 4, pp. 3238-3273, 4th Quart. 2019.

[11] T. Bai and R. W. Heath, Jr., “Coverage and rate analysis for millimeter-wave cellular networks,” *IEEE Trans. Wireless Commun.*, vol. 14, no. 2, pp. 1100-1114, Feb. 2015.

[12] E. Turgut and M. C. Gursoy, "Coverage in heterogeneous downlink millimeter wave cellular networks," *IEEE Trans. Commun.,* vol. 65, no. 10, pp. 4463-4477, Oct. 2017.

[13] N. Deng, M. Haenggi and Y. Sun, “Millimeter-wave device-to-device networks with heterogeneous antenna arrays,” *IEEE Trans. Commun.,* vol. 66, no. 9, pp. 4271-4285, Sept. 2018.

[14] X. Yu, J. Zhang, M. Haenggi and K. B. Letaief, “Coverage analysis for millimeter wave networks: the impact of directional antenna arrays,” *IEEE J. Sel. Areas Commun.,* vol. 35, no. 7, pp. 1498-1512, Jul. 2017.

[15] N. Seifi, R. W. Heath, M. Coldrey and T. Svensson, “Adaptive multicell 3-D beamforming in multiantenna cellular networks,” *IEEE Trans. Veh. Technol.,* vol. 65, no. 8, pp. 6217-6231, Aug. 2016.

[16] M. Baianifar, S. Khavari, S. M. Razavizadeh, and T. Svensson, “Impact of user height on the coverage of 3D beamforming-enabled massive MIMO systems,” in *Proc. IEEE 28th Annu. Int. Symp. Pers., Indoor, Mobile Radio Commun. (PIMRC)*, Oct. 2017, pp. 1–5.

[17] J. Yang, M. Ding, G. Mao, Z. Lin, D. Zhang and T. H. Luan, "Optimal base station antenna downtilt in downlink cellular networks," *IEEE Trans. Wireless Commun.*, vol. 18, no. 3, pp. 1779-1791, Mar. 2019.

[18] M. Gapeyenko *et al.*, "Analysis of human-body blockage in urban millimeter-wave cellular communications," in *Proc. IEEE Int. Conf. Commun. (ICC)*, 2016, pp. 1-7.

[19] R. Kovalchukov *et al.*, "Evaluating SIR in 3D millimeter-wave deployments: direct modeling and feasible approximations," *IEEE Trans. Wireless Commun.,* vol. 18, no. 2, pp. 879-896, Feb. 2019.

[20] P. Series, "Propagation data and prediction methods required for the design of terrestrial broadband radio access systems operating in a frequency range from 3 to 60 GHz," *Recommendation ITU-R*, pp. 1410-1415, 2013.

[21] T. Rappaport et al., "Millimeter wave mobile communications for 5G cellular: It will work!" *IEEE Access*, vol. 1, pp. 335-349, 2013.

[22] 3GPP TR 37.840 v12.1.0, "Technical Specification Group Radio Access Network; Study of Radio Frequency (RF) and Electromagnetic Compatibility (EMC) requirements for Active Antenna Array System (AAS) base station," Tech. Rep., 2013.

[23] X. Li, R. W. Heath, Jr., K. Linehan, and R. Butler. (Feb. 2015). "Impact of metro cell antenna pattern and downtilt in heterogeneous networks." [Online]. Available: https://arxiv.org/abs/1502.05782

[24] K. Venugopal, M. C. Valenti and R. W. Heath, "Device-to-device millimeter wave communications: interference, coverage, rate, and finite topologies," *IEEE Trans. Wireless Commun.*, vol. 15, no. 9, pp. 6175-6188, Sept. 2016.

[25] T. Bai, R. Vaze and R. W. Heath, "Analysis of blockage effects on urban cellular networks," *IEEE Trans. Wireless Commun.*, vol. 13, no. 9, pp. 5070-5083, Sept. 2014.

[26] M. Abramowitz and I. A. Stegun, *Handbook of Mathematical Functions with Formulas, Graphs, and Mathematical Tables*, 9th edition. Dover Publications, 1972.

[27] B. Yang, G. Mao, M. Ding, X. Ge and X. Tao, "Dense small cell networks: from noise-limited to dense interference-limited," *IEEE Trans. Veh. Technol.,* vol. 67, no. 5, pp. 4262-4277, May. 2018.

[28] A. Thornburg, T. Bai, and R. Heath, "Performance analysis of outdoor mmWave ad hoc networks," *IEEE Trans. Signal Process.*, vol. 64, no. 15, pp. 4065-4079, Aug. 2016.

[29] J. Liu, M. Sheng and J. Li, "Improving network capacity scaling law in ultra-dense small cell networks," *IEEE Trans. Wireless Commun.,* vol. 17, no. 9, pp. 6218-6230, Sept. 2018.

[30] W. P. Johnson, "The curious history of Faà di Bruno's formula," *Amer. Math. Monthly*, vol. 109, no. 3, pp. 217–234, 2002.

Paper II

On the Deployment of Small Cells in 3D Heterogeneous Networks, co-authored with J. Zhang, X. Chu and J. Zhang. This paper has been submitted to IEEE Transactions on Wireless Communications.

I conceived the idea and carried out the mathematical analysis, numerical simulations and writing of the manuscript. Jiliang Zhang, Xiaoli Chu, and I contributed to the network modelling. Xiaoli Chu and Jie Zhang guided and supervised the work. All authors discussed the theoretical aspects and numerical results, and reviewed the manuscript.

On the Deployment of Small Cells in 3D Heterogeneous Networks

Chen Chen[1], Jiliang Zhang[1], Xiaoli Chu[1], and Jie Zhang[1,2]

[1] Department of Electronic and Electrical Engineering, the University of Sheffield, Sheffield, S10 2TN, UK

[2] Ranplan Wireless Network Design Ltd., Cambridge, CB23 3UY, UK

Abstract

With the dense deployment of small cells, the impact of height difference between base stations (BSs) and user equipments (UEs) on the performance of heterogeneous networks (HetNets) becomes significant. The traditional two-dimensional models are no longer sufficient to capture the three-dimensional (3D) features of dense HetNets. In this paper, we propose a 3D model for a K-tier HetNet, where different tiers may differ in BS height, BS density, number of antennas per BS, transmit power, association bias, and path loss exponent. We analytically derive the per-tier association probability under both the strongest received signal and the closest BS cell-association strategies. Based on that, we derive the expressions for the downlink ergodic rate, area spectral efficiency (ASE) and energy efficiency. The numerical results reveal that in the presence of macrocell BSs, for low to medium small-cell BS (SBS) densities, the closest BS cell-association strategy leads to low ergodic rate, ASE and energy efficiency regardless of the SBS height; while at very high SBS densities, under both cell-association strategies, SBSs should be deployed at the same height as UEs to achieve high ergodic rate, ASE and energy efficiency. Moreover, we find that for a given SBS height, there exists an optimal combination of SBS density and number of antennas per SBS that maximizes the system energy efficiency.

1 Introduction

The 1000× network capacity gain of 5G is fueled by the dense deployment of small cells [1–4]. A typical heterogeneous network (HetNet) comprises macrocells overlaid by various types of

small-cells like picocells, femtocells, and relays [5]. The reported research on HetNets was mainly conducted on a two-dimensional (2D) plane, ignoring the height difference between the base stations (BSs) and the UEs [6–8]. In dense HetNets, where small-cell BSs (SBSs) can be very close to the UEs, the heights of BSs and UEs need to be considered in the calculation of link ranges and will affect the network performance with respect to coverage probability and area spectral efficiency (ASE) [9]. Therefore, given the existing macrocell network, the deployment of SBSs needs to be studied in three dimensions, i.e., to consider BS heights in addition to the BS locations on the 2D ground plane. On the other track, deploying more antennas on BSs is playing an important role in addressing the rapid growth of wireless capacity demands [10]. In this paper, we propose a three-dimensional (3D) HetNet model where each BS is equipped with multiple antennas, and develop an analytical framework to evaluate the network performance with regard to the downlink ergodic rate, ASE and energy efficiency for both the strongest received signal cell-association strategy and the closest BS cell-association strategy.

1.1 Related Works

HetNets have been extensively investigated using stochastic geometry [11–15]. In [11], the downlink signal-to-interference-plus-noise-ratio (SINR) and outage probability were characterized for a K-tier HetNet where each tier is allocated with a particular association bias and each UE is connected to the BS providing the strongest biased average received power. The optimal per-tier bias that maximizes the downlink coverage was obtained in a multi-antenna HetNet in [13]. Considering a realistic path loss model and directional antenna gains, the authors in [12] analyzed the downlink coverage performance of millimeter-wave HetNets. In [14], the latency and deployment cost were characterized taking into account both wired and wireless backhauls for a two-tier HetNet. In [15], the authors explored coordinated multipoint transmission in HetNets in the presence of user mobility. However, all of these works modeled the HetNets on a 2D plane.

Several studies have modeled HetNets using 3D stochastic geometry due to its tractability [16, 17]. In [16], the millimeter-wave HetNet was modeled using a 3D Mátern Hard-Core

Process with a BS density in BS/m^3 and the downlink coverage probability was derived. An indoor 3D HetNet was studied in [17], where the picocells and femtocells were distributed following two independent 3D Poisson point processes (PPPs). These works modelled BS locations as 3D point processes where the BS height is randomly distributed in the third dimension without any bound, which may be suitable for the indoor small-cell networks in high-rise buildings. Nevertheless, in outdoor networks, BSs of the same type usually have similar heights within a certain range.

The impact of the height difference between BSs and UEs on network performance has been studied recently [9, 18–20]. In [9], a single-tier small-cell network was analyzed considering a multi-slope path loss model incorporating both line-of-sight (LoS) and non-line-of-sight (NLoS) transmissions as well as the height difference between SBSs and UEs. It was shown that even when the SBSs are equipped with directional antennas, both the downlink coverage and ASE degrade to zero as the SBS density increases to infinity. The effect of LOS/NLOS path loss model with random placed buildings was integrated in a single-tier small-cell network with elevated BSs in [18]. The results revealed that the coverage probability would monotonically decrease for the closest BS association, while the monotonicity would not hold for the strongest BS association. In [19], the authors analyzed the effect of vertical beamforming on the coverage probability and obtained the optimal antenna downtilt numerically. In [20], the authors investigated the optimal BS height for a single-tier mmWave network, where the blockages were modelled as cylinders with an exponentially distributed height. However, none of these works captured the heterogeneity of current cellular networks.

Unmanned aerial vehicle (UAV) assisted wireless networks can be considered as a type of 3D HetNets. In [21], the aerial BSs were modeled as a 2D PPP at a particular height and the terrestrial BSs were modelled as a 2D PPP on the ground. In [22], the authors studied UAV-assisted cell-edge offloading for ground HetNets. In [23], a general K-layer UAV network model was proposed, in which the coverage probability and throughput were derived for the closest node and the strongest received pilot signal node association strategies. Although the heights of UAVs were considered in [21–23], the heights of terrestrial BSs on the ground were ignored. In [24], the height difference between terrestrial BSs and UEs was considered, but the

closest BS cell-association strategy did not include the cell-association bias, which would be necessary for load balancing across different tiers in a HetNet. Moreover, the aforementioned works only considered single-antenna BSs and UAVs, while the the analysis of HetNets with multi-antenna BSs is much more challenging [13]. It is worth noting that UAVs usually have a much higher height than UEs [25], while SBSs can be deployed at the similar height of UEs, which requires a different deployment strategy than UAV deployment.

To the best of our knowledge, the performance analysis of a multi-tier 3D HetNet with multi-antenna transmission and LOS/NLOS path-loss attenuation has not been fully investigated, which will be the focus of this paper.

1.2 Contributions

In this paper, we study the deployment of small cells in a 3D HetNet taking into account the potentially different BS height, number of antennas per BS and cell-association bias for each tier. The main contributions of this paper are summarized as follows:

- We develop a novel stochastic geometry framework for a K-tier 3D HetNet, where different tiers have potentially different BS densities, BS heights, number of antennas per BS and cell-association biases. Moreover, we incorporate the LOS/NLOS transmission into both the large-scale path loss and small-scale fading.

- Based on the framework, we derive the LOS probability of a link as a function of system parameters such as the BS density, the blockage density, the link distance, and the height difference between BSs and UEs. Furthermore, the per-tier association probability is newly derived for both the strongest received signal and the closest BS cell-association strategies.

- The per-tier association probability is then used to obtain the downlink ergodic rates for both the strongest received signal and the closest BS cell-association strategies. Our analytical and numerical results show the effects of the SBS density, SBS height, number of antennas per SBS and SBS bias on the ergodic rate. We find that in the presence of macrocell BSs (MBSs), the ergodic rate monotonically decreases with the SBS density

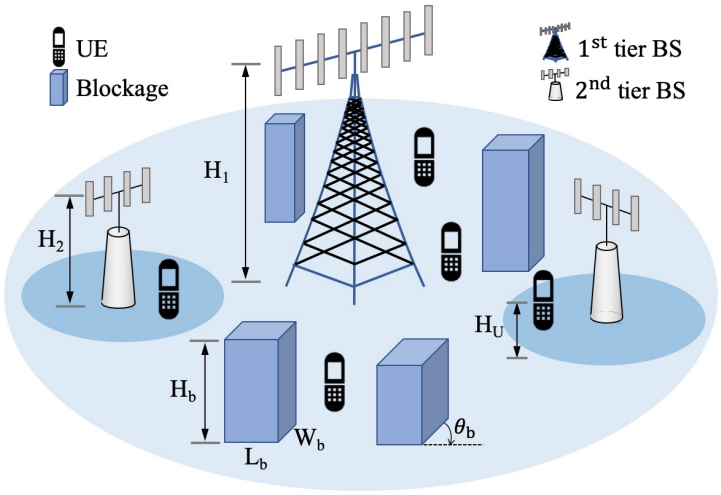

Fig. 1 An illustration of a 3D heterogeneous network.

regardless of the SBS height, which is different from the observation in a single-tier small-cell network [9].

- We also derive the expressions for the ASE and energy efficiency. We observe that under both cell-association strategies, SBSs should be deployed at the same height as UEs in an ultra-dense HetNet for good network performance in terms of the ergodic rate, ASE and energy efficiency.

1.3 Paper Organization

The remainder of this paper is structured as follows. Section II describes the system model. The expressions of downlink ergodic rate are derived in Section III. In Section IV, we extend our analysis to ASE and energy efficiency. The numerical results are presented in Section V, with remarks shedding new light on the deployment of multi-antenna SBSs in 3D HetNets. Finally, the conclusions are drawn in Section VI.

2 System Model

2.1 Network Model

We consider downlink transmission in an outdoor K-tier 3D HetNet, where the horizontal locations of the BSs in the k^{th} tier are modelled following a homogeneous PPP $\widetilde{\Phi}_k$ with density $\widetilde{\lambda}_k$ on a 2D ground plane, in the absence of blockages. Each BS in the k^{th} tier has transmit power P_k with M_k antennas deployed in a horizontal linear array. We assume that BSs in the k^{th} tier are deployed at a fixed height H_k for analytical tractability. This assumption can be extended to the case where the BS height of each tier follows a specific distribution, which will be investigated in our future work. The set of indices of the tiers is denoted by $\mathscr{K} = \{1, 2, \ldots, K\}$. The horizontal locations of single-antenna UEs are also modelled following a homogeneous PPP Φ_{U} with density λ_{U}, which is independent of $\{\Phi_k\}_{k\in\mathscr{K}}$. λ_{U} is assumed to be sufficiently large so that each BS can have at least one served UE [9, 18]. The UEs are of the same height H_{U} and $H_k \geq H_{\text{U}}$ for $k \in \mathscr{K}$. Blockages are assumed to be cuboids [26] with a uniformly distributed length $L_{\text{b}} \sim U(0, 2\overline{L}_{\text{b}})$, a uniformly distributed width $W_{\text{b}} \sim U(0, 2\overline{W}_{\text{b}})$, a uniformly distributed orientation $\theta_{\text{b}} \sim U(0, 2\pi)$, and a Rayleigh-distributed height H_{b} with mean $\overline{H}_{\text{b}}$. The centers of the blockages on the ground plane are distributed following a homogeneous PPP Φ_{b} with density λ_{b}. In the presence of blockages, the actual horizontal locations of the BSs in the k^{th} tier form a Poisson hole process $\widehat{\Phi}_k = \widetilde{\Phi}_k \backslash \Phi_{k,\text{b}}$, where $\Phi_{k,\text{b}}$ denotes the set of the k^{th} tier BSs located in the blockage regions. Assuming that BSs and blockages are independently distributed, $\widehat{\Phi}_k$ can be well approximated by a homogeneous PPP Φ_k with density $\lambda_k = \widetilde{\lambda}_k \exp(-\lambda_{\text{b}} \overline{L}_{\text{b}} \overline{W}_{\text{b}})$ [27]. Without loss of generality, we consider that the typical UE under study is located at the origin of the ground plane. We assume that all the tiers share the same frequency band, and that orthogonal resource partitioning is adopted in each cell to eliminate intra-cell interference. A two-tier 3D HetNet scenario is shown in Fig. 1, and the used notations are listed in Table 1.

Table 1 Summary of Notations

Notation	Meaning
$\Phi_k, \Phi_{\mathrm{b}}, \Phi_{\mathrm{U}}$	Homogeneous PPPs modeling the horizontal locations of the k^{th}-tier BSs, blockages and UEs, respectively
λ_{k}, λ_{b}, λ_{U}	Densities of the k^{th}-tier BSs, blockages and UEs, respectively
$H_k, H_{\mathrm{b}}, H_{\mathrm{U}}$	Heights of the k^{th}-tier BSs, blockages and UEs, respectively
$\hat{H}_k$	$H_k - H_{\mathrm{U}}$
L_{b}, W_{b}, θ_{b}	Length, width and orientation of blockages, respectively
$\overline{L}_{\mathrm{b}}, \overline{W}_{\mathrm{b}}, \overline{H}_{\mathrm{b}}$	Mean values of blockage length, blockage width and blockage height, respectively
β_k^{L}, β_k^{NL}	Path loss of LOS and NLOS transmission links at the reference distance in the k^{th} tier, respectively
α_k^{L}, α_k^{NL}	Path loss exponents of LOS and NLOS transmission links in the k^{th} tier, respectively
P_k	Transmit power of BSs in the k^{th} tier
M_k	Number of antennas per BS in the k^{th} tier
B_k	A BS in the k^{th} tier with horizontal distance r_{B_k} from the origin
h_k^{L}, h_k^{NL}	Small-scale fading power gains of serving LOS and NLOS transmission links in the k^{th} tier, respectively
g_k^{L}, g_k^{NL}	Small-scale fading power gains of interfering LOS and NLOS transmission links in the k^{th} tier, respectively
m_k	Shape parameter of Nakagami-m fading in the k^{th} tier
R_k^{L}, R_k^{NL}	Horizontal distances from the typical UE to its nearest LOS BS and NLOS BS in the k^{th} tier, respectively
C_k	Cell-association bias for the k^{th} tier
$P_{\mathrm{L},k}(x)$, $P_{\mathrm{NL},k}(x)$	LOS and NLOS probabilities of a transmission link with horizontal distance x in the k^{th} tier, respectively
$P_{\mathrm{r},k}^{\mathrm{L}}(x)$, $P_{\mathrm{r},k}^{\mathrm{NL}}(x)$	Average biased received power of LOS and NLOS transmission links with horizontal distance x in the k^{th} tier, respectively
$T_k(x)$	Biased transmission distance from a BS to the typical UE with horizontal distance x in the k^{th} tier
$\mathscr{R}_{\mathrm{S}}, \mathscr{R}_{\mathrm{C}}$	Downlink ergodic rates under the strongest received signal and closest BS cell-association strategies, respectively
δ_k^2	Additive white Gaussian noise power in the k^{th} tier
$\eta_k, P_{\mathrm{C},k}, \rho_k$	Power amplifier efficiency, circuit power per antenna, and parameter related to DC-DC converter, current supply and cooling in the k^{th} tier

2.2 LOS Probability

For a BS B_k with horizontal distance r_{B_k} from the origin in the k^{th} tier, the horizontal LOS probability between B_k and the typical UE is a function of r_{B_k} given by $e^{-\xi r_{B_k}}$, where $\xi = \frac{2\lambda_{\mathrm{b}}(\mathbb{E}(L_{\mathrm{b}})+\mathbb{E}(W_{\mathrm{b}}))}{\pi} = \frac{2\lambda_{\mathrm{b}}\left(\overline{L}_{\mathrm{b}}+\overline{W}_{\mathrm{b}}\right)}{\pi}$ [20, 26].

The conditional probability that a blockage blocks the transmission link between B_k and the typical UE in the vertical dimension under the condition that it blocks the transmission link in the horizontal dimension is computed following [26] by

$$\begin{aligned}\mu_k &= 1 - \frac{1}{r_{B_k}} \int_0^{r_{B_k}} \int_0^{\frac{H_{\mathrm{U}} r_{B_k} + \hat{H}_k t}{r_{B_k}}} f_{H_{\mathrm{b}}}(x) \mathrm{d}x \mathrm{d}t \\ &= \frac{\overline{H}_{\mathrm{b}} \left[\mathrm{erf}\left(\frac{\sqrt{\pi} H_k}{2\overline{H}_{\mathrm{b}}} \right) - \mathrm{erf}\left(\frac{\sqrt{\pi} H_{\mathrm{U}}}{2\overline{H}_{\mathrm{b}}} \right) \right]}{\hat{H}_k},\end{aligned} \tag{1}$$

where $\hat{H}_k = H_k - H_{\mathrm{U}}$, $f_{H_{\mathrm{b}}}(x) = \frac{\pi x}{2\overline{H}_{\mathrm{b}}^2} e^{-\frac{\pi x^2}{4\overline{H}_{\mathrm{b}}^2}}$ is the probability density function (PDF) of H_{b} and $\mathrm{erf}(\cdot)$ is the error function. Then, the 3D LOS probability of the transmission link between B_k and the typical UE is given by

$$P_{\mathrm{L},k}(r_{B_k}) = e^{-\xi \mu_k r_{B_k}}. \tag{2}$$

Correspondingly, the 3D NLOS probability is given by $P_{\mathrm{NL},k}(r_{B_k}) = 1 - P_{\mathrm{L},k}(r_{B_k})$. From (2), we can see that the LOS probability monotonically decreases with the horizontal distance of a transmission link and increases with the BS height.

2.3 Channel Model

The channel model is composed of path loss and small-scale fading. A transmission link can be either an LOS or NLOS link, and the path loss from B_k to the typical UE can be expressed as follows

$$l_k(r_{B_k}) = \begin{cases} \beta_k^{\mathrm{L}} \left(r_{B_k}^2 + \hat{H}_k^2 \right)^{-\frac{\alpha_k^{\mathrm{L}}}{2}}, & \text{with prob. } P_{\mathrm{L},k}(r_{B_k}) \\ \beta_k^{\mathrm{NL}} \left(r_{B_k}^2 + \hat{H}_k^2 \right)^{-\frac{\alpha_k^{\mathrm{NL}}}{2}}, & \text{with prob. } P_{\mathrm{NL},k}(r_{B_k}) \end{cases} \tag{3}$$

where β_k^{L} and β_k^{NL} are the path loss of LOS and NLOS transmission links at the reference distance, respectively, and α_k^{L} and α_k^{NL} are the path loss exponents of LOS and NLOS transmis-

sion links in the k^{th} tier, respectively. For analytical tractability, the modelling of multi-slope path loss [9] has not been included, which will be investigated in our future work.

For single-input single-output transmission in the k^{th} tier, i.e., $M_k = 1$, we characterize the small-scale fading of LOS and NLOS transmission links by Nakagami-*m* fading with shape parameter m_k and Rayleigh fading, respectively [18]. Notice that when the shape parameter is set to 1, Nakagami-*m* fading reduces to Rayleigh fading. The channel power gain of the transmission link from a multi-antenna BS to the typical UE depends on the multi-antenna transmission technique and whether the BS is a serving BS or an interfering BS. In this paper, we focus on sub-6GHz frequencies. We adopt maximal ratio transmission (MRT) precoding and assume perfect channel state information. If B_k is a serving BS, we denote the channel power gain of the link from B_k to the typical UE by $h_k^{\text{L}} \sim \Gamma(M_k m_k, \frac{1}{m_k})$ and $h_k^{\text{NL}} \sim \Gamma(M_k, 1)$, when the link is in LOS and NLOS conditions, respectively [28]. If B_k is an interfering BS, we denote the channel power gain of the link from B_k to the typical UE by $g_k^{\text{L}} \sim \Gamma(m_k, \frac{1}{m_k})$ and $g_k^{\text{NL}} \sim \text{Exp}(1)$, when the link is in LOS and NLOS conditions, respectively.

2.4 Cell Association

We consider both the strongest received signal and the closest BS cell-association strategies, where one UE can only connect to one BS. In the Lemma below, we give the PDFs of the distances from the typical UE to its nearest LOS and NLOS BSs in the k^{th} tier, respectively, which will be useful when we develop expressions of cell association probabilities.

Lemma 1. *Denoting by R_k^{L} and R_k^{NL} the horizontal distances from the typical UE to its nearest LOS BS and NLOS BS in the k^{th} tier, respectively, the PDFs of R_k^{L} and R_k^{NL} are given by*

$$f_{R_k^{\text{L}}}(x) = 2\pi\lambda_k x P_{\text{L},k}(x) \exp\left\{-2\pi\lambda_k E_k(x)\right\}, \tag{4}$$

$$f_{R_k^{\text{NL}}}(x) = 2\pi\lambda_k x P_{\text{NL},k}(x) \exp\left\{-\pi\lambda_k x^2 + 2\pi\lambda_k E_k(x)\right\}, \tag{5}$$

where $E_k(x) = \frac{1}{(\xi\mu_k)^2}\left[1 - (\xi\mu_k x + 1)e^{-\xi\mu_k x}\right]$.

Proof. The cumulative distribution function (CDF) of R_k^{L} is computed by

$$\begin{aligned} F_{R_k^{\mathrm{L}}}(x) &= 1-\mathbb{P}(R_k^{\mathrm{L}}>x) \\ &\overset{(a)}{=} 1-\exp\left\{-2\pi\lambda_k\int_0^x e^{-\xi\mu_k R_k^{\mathrm{L}}}R_k^{\mathrm{L}}\mathrm{d}R_k^{\mathrm{L}}\right\} \\ &= 1-e^{-2\pi\lambda_k E_k(x)}, \end{aligned} \tag{6}$$

where (a) is obtained using the void probability of PPP. Then the PDF of R_k^{L} is computed by

$$f_{R_k^{\mathrm{L}}}(x)=\frac{\mathrm{d}F_{R_k^{\mathrm{L}}}(x)}{\mathrm{d}(x)}=2\pi\lambda_k x e^{-[\xi\mu_k x+2\pi\lambda_k E_k(x)]}. \tag{7}$$

The PDF of R_k^{NL} can be derived following the similar steps. □

Under the strongest received signal cell-association strategy, a UE connects to the BS providing the strongest downlink average biased received power. Denoting the bias factor for the k^{th} tier by C_k, the downlink average biased received power at the typical UE from B_k is computed by

$$P_{\mathrm{r},k}^{s}(r_{B_k})=P_k C_k \beta_k^s\left(r_{B_k}^2+\hat{H}_k^2\right)^{-\frac{\alpha_k^s}{2}}, \tag{8}$$

where s takes the form of L and NL when the transmission link from B_k to the typical UE is in LOS and NLOS conditions, respectively. The typical UE connects to a BS with channel condition s in the k^{th} tier if

$$k,s=\underset{j\in\mathscr{K},t\in\{\mathrm{L},\mathrm{NL}\}}{\arg\max}\ P_{\mathrm{r},j}^{t}\left(R_j^t\right). \tag{9}$$

Then we characterize the cell association probability under the strongest received signal cell-association strategy in the following Lemma.

Lemma 2. *Under the strongest received signal cell-association strategy, the probabilities that the typical UE is associated with an LOS BS and an NLOS BS in the k^{th} tier, denoted by $\mathscr{A}_{\mathrm{S},k}^{\mathrm{L}}$*

and $\mathscr{A}_{\mathrm{S},k}^{\mathrm{NL}}$*, respectively, are given by*

$$\mathscr{A}_{\mathrm{S},k}^{\mathrm{L}} = \int_0^{\infty} f_{R_k^{\mathrm{L}}}(x) \prod_{j\in\mathscr{K},j\neq k} e^{-2\pi\lambda_j \int_0^{F_{\mathrm{S},k,j,\mathrm{L}}^{\mathrm{L}}(x)} P_{\mathrm{L},j}(u)u\mathrm{d}u} \times \prod_{j\in\mathscr{K}} e^{-2\pi\lambda_j \int_0^{F_{\mathrm{S},k,j,\mathrm{L}}^{\mathrm{NL}}(x)} P_{\mathrm{NL},j}(u)u\mathrm{d}u}\mathrm{d}x, \tag{10}$$

$$\mathscr{A}_{\mathrm{S},k}^{\mathrm{NL}} = \int_0^{\infty} f_{R_k^{\mathrm{NL}}}(x) \prod_{j\in\mathscr{K},j\neq k} e^{-2\pi\lambda_j \int_0^{F_{\mathrm{S},k,j,\mathrm{NL}}^{\mathrm{NL}}(x)} P_{\mathrm{NL},j}(u)u\mathrm{d}u} \times \prod_{j\in\mathscr{K}} e^{-2\pi\lambda_j \int_0^{F_{\mathrm{S},k,j,\mathrm{NL}}^{\mathrm{L}}(x)} P_{\mathrm{L},j}(u)u\mathrm{d}u}\mathrm{d}x, \tag{11}$$

where

$$F_{\mathrm{S},k,j,s}^{t}(x) = \begin{cases} 0, & x < D_{\mathrm{S},k,j,s}^{t}, \\ \sqrt{\left(\Omega_{k,j,s}^{t}\right)^{-\frac{2}{\alpha_j^t}} \left(x^2+\hat{H}_k^2\right)^{\frac{\alpha_k^s}{\alpha_j^t}} - \hat{H}_j^2}, & x \geq D_{\mathrm{S},k,j,s}^{t}, \end{cases} \tag{12}$$

where $s,t \in \{\mathrm{L},\mathrm{NL}\}$*,* $\Omega_{k,j,s}^{t} = \frac{P_k \beta_k^s C_k}{P_j \beta_j^t C_j}$*, and*

$$D_{\mathrm{S},k,j,s}^{t} = \begin{cases} 0, & \hat{H}_j^{\frac{\alpha_j^t}{\alpha_k^s}} \left(\Omega_{k,j,s}^{t}\right)^{\frac{1}{\alpha_k^s}} < \hat{H}_k, \\ \sqrt{\hat{H}_j^{\frac{2\alpha_j^t}{\alpha_k^s}} \left(\Omega_{k,j,s}^{t}\right)^{\frac{2}{\alpha_k^s}} - \hat{H}_k^2}, & \hat{H}_j^{\frac{\alpha_j^t}{\alpha_k^s}} \left(\Omega_{k,j,s}^{t}\right)^{\frac{1}{\alpha_k^s}} \geq \hat{H}_k. \end{cases} \tag{13}$$

Proof. See Appendix A. □

Under the strongest received signal cell-association strategy, let $X_{\mathrm{S},k}^{\mathrm{L}}$ and $X_{\mathrm{S},k}^{\mathrm{NL}}$ be the distances from the serving LOS BS and NLOS BS to the typical UE, given that the typical UE is associated with an LOS BS and an NLOS BS in the k^{th} tier, respectively. We characterize the PDFs of $X_{\mathrm{S},k}^{\mathrm{L}}$ and $X_{\mathrm{S},k}^{\mathrm{NL}}$ in the following Lemma.

Lemma 3. *Under the strongest received signal cell-association strategy, the PDFs of the distances from the serving LOS BS and NLOS BS in the* k^{th} *tier to the typical UE, denoted by*

$f_{X^{\mathrm{L}}_{\mathrm{S},k}}(x)$ and $f_{X^{\mathrm{NL}}_{\mathrm{S},k}}(x)$, respectively, are given by

$$f_{X^{\mathrm{L}}_{\mathrm{S},k}}(x) = \frac{f_{R^{\mathrm{L}}_k}(x)}{\mathscr{A}^{\mathrm{L}}_{\mathrm{S},k}} \prod_{j\in\mathscr{K},j\neq k} e^{-2\pi\lambda_j \int_0^{F^{\mathrm{L}}_{\mathrm{S},k,j,\mathrm{L}}(x)} P_{\mathrm{L},j}(u)u\mathrm{d}u} \times \prod_{j\in\mathscr{K}} e^{-2\pi\lambda_j \int_0^{F^{\mathrm{L}}_{\mathrm{S},k,j,\mathrm{NL}}(x)} P_{\mathrm{NL},j}(u)u\mathrm{d}u}, \tag{14}$$

$$f_{X^{\mathrm{NL}}_{\mathrm{S},k}}(x) = \frac{f_{R^{\mathrm{NL}}_k}(x)}{\mathscr{A}^{\mathrm{NL}}_{\mathrm{S},k}} \prod_{j\in\mathscr{K},j\neq k} e^{-2\pi\lambda_j \int_0^{F^{\mathrm{NL}}_{\mathrm{S},k,j,\mathrm{NL}}(x)} P_{\mathrm{NL},j}(u)u\mathrm{d}u} \times \prod_{j\in\mathscr{K}} e^{-2\pi\lambda_j \int_0^{F^{\mathrm{L}}_{\mathrm{S},k,j,\mathrm{NL}}(x)} P_{\mathrm{L},j}(u)u\mathrm{d}u}. \tag{15}$$

Proof. Denoting the event that the typical UE is associated with an LOS BS in the k^{th} tier by $V^{\mathrm{L}}_{\mathrm{S},k}$, the CDF of $X^{\mathrm{L}}_{\mathrm{S},k}$ is computed by

$$\mathbb{P}\left[X^{\mathrm{L}}_{\mathrm{S},k} < x\right] = \mathbb{P}\left[R^{\mathrm{L}}_k < x | V^{\mathrm{L}}_{\mathrm{S},k}\right] = \frac{\mathbb{P}\left[R^{\mathrm{L}}_k < x, V^{\mathrm{L}}_{\mathrm{S},k}\right]}{\mathbb{P}\left[V^{\mathrm{L}}_{\mathrm{S},k}\right]}, \tag{16}$$

where $\mathbb{P}\left[V^{\mathrm{L}}_{\mathrm{S},k}\right] = \mathscr{A}^{\mathrm{L}}_{\mathrm{S},k}$, and

$$\mathbb{P}\left[R^{\mathrm{L}}_k < x, V^{\mathrm{L}}_{\mathrm{S},k}\right] = \int_0^x \mathbb{P}\left[P^{\mathrm{L}}_{\mathrm{r},k}(u) > \max_{j\in\mathscr{K},j\neq k} P^{\mathrm{L}}_{\mathrm{r},j}\left(R^{\mathrm{L}}_j\right)\right] \times \mathbb{P}\left[P^{\mathrm{L}}_{\mathrm{r},k}(u) > \max_{j\in\mathscr{K}} P^{\mathrm{NL}}_{\mathrm{r},j}\left(R^{\mathrm{NL}}_j\right)\right] f_{R^{\mathrm{L}}_k}(u)\mathrm{d}u, \tag{17}$$

where $\mathbb{P}\left[P^{\mathrm{L}}_{\mathrm{r},k}(u) > \max_{j\in\mathscr{K},j\neq k} P^{\mathrm{L}}_{\mathrm{r},j}\left(R^{\mathrm{L}}_j\right)\right]$ and $\mathbb{P}\left[P^{\mathrm{L}}_{\mathrm{r},k}(u) > \max_{j\in\mathscr{K}} P^{\mathrm{NL}}_{\mathrm{r},j}\left(R^{\mathrm{NL}}_j\right)\right]$ can be found in Appendix A. With these insights, $f_{X^{\mathrm{L}}_{\mathrm{S},k}}(x)$ is computed by

$$f_{X^{\mathrm{L}}_{\mathrm{S},k}}(x) = \frac{\mathrm{d}\mathbb{P}[X^{\mathrm{L}}_{\mathrm{S},k} < x]}{\mathrm{d}x}. \tag{18}$$

□

Under the closest BS cell-association strategy, the typical UE connects to the BS with the shortest biased transmission distance. The biased transmission distance from B_k to the typical UE is given by

$$T_k(r_{B_k}) = (r_{B_k}^2 + \hat{H}_k^2)^{\frac{1}{2}} C_k. \tag{19}$$

The typical UE connects to a BS with channel condition s in the k^{th} tier if

$$k, s = \underset{j \in \mathscr{K}, t \in \{\text{L,NL}\}}{\arg\min} \; T_j\left(R_j^t\right). \tag{20}$$

Then we characterize the cell association probability under the closest BS cell-association strategy in the following Lemma.

Lemma 4. *Under the closest BS cell-association strategy, the probabilities that the typical UE is associated with an LOS BS and an NLOS BS in the k^{th} tier, denoted by $\mathscr{A}_{\text{C},k}^{\text{L}}$ and $\mathscr{A}_{\text{C},k}^{\text{NL}}$, respectively, are given by*

$$\mathscr{A}_{\text{C},k}^{\text{L}} = \int_0^{\infty} f_{R_k^{\text{L}}}(x) \prod_{j \in \mathscr{K}, j \neq k} e^{-2\pi\lambda_j \int_0^{F_{\text{C},k,j}(x)} P_{\text{L},j}(u) u \mathrm{d}u} \times \prod_{j \in \mathscr{K}} e^{-2\pi\lambda_j \int_0^{F_{\text{C},k,j}(x)} P_{\text{NL},j}(u) u \mathrm{d}u} \mathrm{d}x, \tag{21}$$

$$\mathscr{A}_{\text{C},k}^{\text{NL}} = \int_0^{\infty} f_{R_k^{\text{NL}}}(x) \prod_{j \in \mathscr{K}, j \neq k} e^{-2\pi\lambda_j \int_0^{F_{\text{C},k,j}(x)} P_{\text{NL},j}(u) u \mathrm{d}u} \times \prod_{j \in \mathscr{K}} e^{-2\pi\lambda_j \int_0^{F_{\text{C},k,j}(x)} P_{\text{L},j}(u) u \mathrm{d}u} \mathrm{d}x, \tag{22}$$

where

$$F_{\text{C},k,j}(x) = \begin{cases} 0, & x < D_{\text{C},k,j}, \\ \sqrt{\left(\frac{C_k}{C_j}\right)^2 \left(x^2 + \hat{H}_k^2\right)^2 - \hat{H}_j^2}, & x \geq D_{\text{C},k,j}, \end{cases} \tag{23}$$

and

$$D_{\mathrm{C},k,j} = \begin{cases} 0, & \hat{H}_j \frac{C_j}{C_k} < \hat{H}_k, \\ \sqrt{\left(\frac{C_j}{C_k}\right)^2 \hat{H}_j^2 - \hat{H}_k^2}, & \hat{H}_j \frac{C_j}{C_k} \geq \hat{H}_k. \end{cases} \tag{24}$$

Proof. It follows similar proof as in Lemma 2. □

Under the closest BS cell-association strategy, let $X_{\mathrm{C},k}^{\mathrm{L}}$ and $X_{\mathrm{C},k}^{\mathrm{NL}}$ be the distances from the serving LOS BS and NLOS BS to the typical UE, given that the typical UE is associated with an LOS BS and an NLOS BS in the k^{th} tier, respectively. We characterize the PDFs of $X_{\mathrm{C},k}^{\mathrm{L}}$ and $X_{\mathrm{C},k}^{\mathrm{NL}}$ in the following Lemma.

Lemma 5. *Under the closest BS cell-association strategy, the PDFs of the distances between the serving LOS BS and NLOS BS in the k^{th} tier and the typical UE, denoted by $f_{X_{\mathrm{C},k}^{\mathrm{L}}}(x)$ and $f_{X_{\mathrm{C},k}^{\mathrm{NL}}}(x)$, respectively, are given by*

$$f_{X_{\mathrm{C},k}^{\mathrm{L}}}(x) = \frac{f_{R_k^{\mathrm{L}}}(x)}{\mathscr{A}_{\mathrm{C},k}^{\mathrm{L}}} \prod_{j\in\mathscr{K},j\neq k} e^{-2\pi\lambda_j \int_0^{F_{\mathrm{C},k,j}(x)} P_{\mathrm{L},j}(u)u\mathrm{d}u} \times \prod_{j\in\mathscr{K}} e^{-2\pi\lambda_j \int_0^{F_{\mathrm{C},k,j}(x)} P_{\mathrm{NL},j}(u)u\mathrm{d}u}, \tag{25}$$

$$f_{X_{\mathrm{C},k}^{\mathrm{NL}}}(x) = \frac{f_{R_k^{\mathrm{NL}}}(x)}{\mathscr{A}_{\mathrm{C},k}^{\mathrm{NL}}} \prod_{j\in\mathscr{K},j\neq k} e^{-2\pi\lambda_j \int_0^{F_{\mathrm{C},k,j}(x)} P_{\mathrm{NL},j}(u)u\mathrm{d}u} \times \prod_{j\in\mathscr{K}} e^{-2\pi\lambda_j \int_0^{F_{\mathrm{C},k,j}(x)} P_{\mathrm{L},j}(u)u\mathrm{d}u}. \tag{26}$$

Proof. It follows similar proof as in Lemma 3. □

3 Downlink Ergodic Rate

In this section, the downlink ergodic rates of the typical UE in a 3D HetNet with muti-antenna BSs are derived for both the strongest received signal and the closest BS cell-association strategies.

3.1 Ergodic Rate Under the Strongest Received Signal Cell-association Strategy

Under the strongest received signal cell-association strategy, when the typical UE connects to an LOS BS $B^{\mathrm{L}}_{\mathrm{S},k}$ in the k^{th} tier, the signal-to-noise-plus-interference ratio (SINR) is given by

$$\mathrm{SINR}^{\mathrm{L}}_{\mathrm{S},k} = \frac{P_k \beta^{\mathrm{L}}_k h^{\mathrm{L}}_k \left[\left(R^{\mathrm{L}}_k\right)^2 + \hat{H}^2_k \right]^{-\frac{\alpha^{\mathrm{L}}_k}{2}}}{I^{\mathrm{L}}_{\mathrm{S},k,\mathrm{L}} + I^{\mathrm{NL}}_{\mathrm{S},k,\mathrm{L}} + \delta^2_k}, \tag{27}$$

where $I^{\mathrm{L}}_{\mathrm{S},k,\mathrm{L}} = \sum_{j\in\mathscr{K}} \sum_{i\in\Phi^{\mathrm{L}}_j \setminus B^{\mathrm{L}}_{\mathrm{S},k}} P_j \beta^{\mathrm{L}}_j g^{\mathrm{L}}_j \left(r^2_{i,j} + \hat{H}^2_j \right)^{-\frac{\alpha^{\mathrm{L}}_j}{2}}$ denotes the interference from LOS BSs, $I^{\mathrm{NL}}_{\mathrm{S},k,\mathrm{L}} = \sum_{j\in\mathscr{K}} \sum_{i\in\Phi^{\mathrm{NL}}_j} P_j \beta^{\mathrm{NL}}_j g^{\mathrm{NL}}_j \left(r^2_{i,j} + \hat{H}^2_j \right)^{-\frac{\alpha^{\mathrm{NL}}_j}{2}}$ denotes the interference from NLOS BSs, δ^2_k is the noise power in the k^{th} tier, Φ^{L}_j and Φ^{NL}_j denote the sets of LOS BSs and NLOS BSs in the k^{th} tier, respectively, and $r_{i,j}$ is the horizontal distance from BS i in the j^{th} tier to the typical UE.

Similarly, when the typical UE connects to an NLOS BS $B^{\mathrm{NL}}_{\mathrm{S},k}$ in the k^{th} tier, the SINR is given by

$$\mathrm{SINR}^{\mathrm{NL}}_{\mathrm{S},k} = \frac{P_k \beta^{\mathrm{NL}}_k h^{\mathrm{NL}}_k \left[\left(R^{\mathrm{NL}}_k\right)^2 + \hat{H}^2_k \right]^{-\frac{\alpha^{\mathrm{NL}}_k}{2}}}{I^{\mathrm{L}}_{\mathrm{S},k,\mathrm{NL}} + I^{\mathrm{NL}}_{\mathrm{S},k,\mathrm{NL}} + \delta^2_k}, \tag{28}$$

where $I^{\mathrm{L}}_{\mathrm{S},k,\mathrm{NL}} = \sum_{j\in\mathscr{K}} \sum_{i\in\Phi^{\mathrm{L}}_j} P_j \beta^{\mathrm{L}}_j g^{\mathrm{L}}_j \left(r^2_{i,j} + \hat{H}^2_j \right)^{-\frac{\alpha^{\mathrm{L}}_j}{2}}$ denotes the interference from LOS BSs and $I^{\mathrm{NL}}_{\mathrm{S},k,\mathrm{NL}} = \sum_{j\in\mathscr{K}} \sum_{i\in\Phi^{\mathrm{NL}}_j \setminus B^{\mathrm{NL}}_{\mathrm{S},k}} P_j \beta^{\mathrm{NL}}_j g^{\mathrm{NL}}_j \left(r^2_{i,j} + \hat{H}^2_j \right)^{-\frac{\alpha^{\mathrm{NL}}_j}{2}}$ denotes the interference from NLOS

BSs. Based on the SINR expressions in (27) and (28), the ergodic rate of the typical UE can be expressed as

$$\mathscr{R}_{\mathrm{S}} = \sum_{k=1}^{K} \left(\mathbb{E}\left[\log\left(1+\mathrm{SINR}_{\mathrm{S},k}^{\mathrm{L}}\right)\right] \mathscr{A}_{\mathrm{S},k}^{\mathrm{L}} + \mathbb{E}\left[\log\left(1+\mathrm{SINR}_{\mathrm{S},k}^{\mathrm{NL}}\right)\right] \mathscr{A}_{\mathrm{S},k}^{\mathrm{NL}} \right). \tag{29}$$

This performance metric can be used to evaluate the average downlink cell throughput with orthogonal multiple access techniques. With the analysis mentioned above, the expression of the ergodic rate is represented in the following Theorem.

Theorem 1. *Under the strongest received signal cell-association strategy, the downlink ergodic rate of the typical UE in nats/s/Hz is given by*

$$\mathscr{R}_{\mathrm{S}} = \sum_{k=1}^{K} \left(\mathscr{R}_{\mathrm{S},k}^{\mathrm{L}} \mathscr{A}_{\mathrm{S},k}^{\mathrm{L}} + \mathscr{R}_{\mathrm{S},k}^{\mathrm{NL}} \mathscr{A}_{\mathrm{S},k}^{\mathrm{NL}} \right), \tag{30}$$

where $\mathscr{A}_{\mathrm{S},k}^{\mathrm{L}}$ and $\mathscr{A}_{\mathrm{S},k}^{\mathrm{NL}}$ have been given in Lemma 2, $\mathscr{R}_{\mathrm{S},k}^{\mathrm{L}}$ and $\mathscr{R}_{\mathrm{S},k}^{\mathrm{NL}}$ are the ergodic rates of the typical UE when it is associated with an LOS BS and an NLOS BS in the k^{th} tier, respectively. The expressions of $\mathscr{R}_{\mathrm{S},k}^{\mathrm{L}}$ and $\mathscr{R}_{\mathrm{S},k}^{\mathrm{NL}}$ are given by

$$\mathscr{R}_{\mathrm{S},k}^{\mathrm{L}} = \int_0^{\infty}\int_0^{\infty} \frac{1-\left(1+\frac{z}{m_k}\right)^{-M_k m_k}}{z} \exp\left\{ -\frac{z}{\mathrm{SNR}_{\mathrm{L},k}(x)} - \sum_{j=1}^{K} Z_{\mathrm{S},k,j,\mathrm{L}}^{\mathrm{L}}(x,z) - \sum_{j=1}^{K} Z_{\mathrm{S},k,j,\mathrm{L}}^{\mathrm{NL}}(x,z) \right\} \times f_{X_{\mathrm{S},k}^{\mathrm{L}}}(x)\mathrm{d}z\mathrm{d}x, \tag{31}$$

$$\mathscr{R}_{\mathrm{S},k}^{\mathrm{NL}} = \int_0^{\infty}\int_0^{\infty} \frac{1-(1+z)^{-M_k}}{z} \exp\left\{ -\frac{z}{\mathrm{SNR}_{\mathrm{NL},k}(x)} - \sum_{j=1}^{K} Z_{\mathrm{S},k,j,\mathrm{NL}}^{\mathrm{L}}(x,z) - \sum_{j=1}^{K} Z_{\mathrm{S},k,j,\mathrm{NL}}^{\mathrm{NL}}(x,z) \right\} \times f_{X_{\mathrm{S},k}^{\mathrm{NL}}}(x)\mathrm{d}z\mathrm{d}x, \tag{32}$$

where $\mathrm{SNR}_{\mathrm{L},k}(x) = \frac{P_k \beta_k^{\mathrm{L}} \left(x^2+\hat{H}_k^2\right)^{-\frac{\alpha_k^{\mathrm{L}}}{2}}}{\delta_k^2}$, $\mathrm{SNR}_{\mathrm{NL},k}(x) = \frac{P_k \beta_k^{\mathrm{NL}} \left(x^2+\hat{H}_k^2\right)^{-\frac{\alpha_k^{\mathrm{NL}}}{2}}}{\delta_k^2}$,

$$Z^t_{\mathrm{S},k,j,s}(x,z) = 2\pi\lambda_j \int_{F^t_{\mathrm{S},k,j,s}(x)}^{\infty} Q^t_{k,j,s}(x,z,u) P_{t,j}(u) u \mathrm{d}u, \tag{33}$$

where $s,t \in \{\mathrm{L},\mathrm{NL}\}$,

$$Q^{\mathrm{L}}_{k,j,s}(x,z,u) = 1 - \left[1 + \frac{z P_j \beta_j^{\mathrm{L}} \left(x^2+\hat{H}_k^2\right)^{\alpha_k^s/2}}{m_j P_k \beta_k^s \left(u^2+\hat{H}_j^2\right)^{\alpha_j^{\mathrm{L}}/2}}\right]^{-m_j}, \tag{34}$$

and

$$Q^{\mathrm{NL}}_{k,j,s}(x,z,u) = 1 - \left[1 + \frac{z P_j \beta_j^{\mathrm{NL}} \left(x^2+\hat{H}_k^2\right)^{\alpha_k^s/2}}{P_k \beta_k^s \left(u^2+\hat{H}_j^2\right)^{\alpha_j^{\mathrm{NL}}/2}}\right]. \tag{35}$$

Proof. See Appendix B. □

Corollary 1. *Suppose* Φ_K *is the small-cell tier with the minimum BS height and largest BS density, i.e.,* $\hat{H}_K < \hat{H}_j, \lambda_K > \lambda_j, j \in \mathscr{K}, j \neq K$, *and* $\hat{H}_K > 0$, *the downlink ergodic rate under the strongest received signal cell-association strategy approaches to zero when* $\lambda_K \to \infty$.

Proof. See Appendix C. □

Corollary 1 reveals that the ultra-dense deployment of SBSs will significantly impair the transmission rate in the presence of the height difference between SBSs and UEs.

3.2 Ergodic Rate Under the Closest BS Cell-association Strategy

In this subsection, we present the expression of the ergodic rate under the closest BS cell-association strategy.

Theorem 2. *Under the closest BS cell-association strategy, the downlink ergodic rate of the typical UE in nats/s/Hz is given by*

$$\mathscr{R}_{\mathrm{C}} = \sum_{k=1}^{K} \left(\mathscr{R}_{\mathrm{C},k}^{\mathrm{L}} \mathscr{A}_{\mathrm{C},k}^{\mathrm{L}} + \mathscr{R}_{\mathrm{C},k}^{\mathrm{NL}} \mathscr{A}_{\mathrm{C},k}^{\mathrm{NL}} \right), \tag{36}$$

where $\mathscr{A}_{\mathrm{C},k}^{\mathrm{L}}$ and $\mathscr{A}_{\mathrm{C},k}^{\mathrm{NL}}$ have been given in Lemma 4, $\mathscr{R}_{\mathrm{C},k}^{\mathrm{L}}$ and $\mathscr{R}_{\mathrm{C},k}^{\mathrm{NL}}$ are the ergodic rates of the typical UE when it is associated with an LOS BS and an NLOS BS in the k^{th} tier, respectively. The expressions of $\mathscr{R}_{\mathrm{C},k}^{\mathrm{L}}$ and $\mathscr{R}_{\mathrm{C},k}^{\mathrm{NL}}$ are given by

$$\mathscr{R}_{\mathrm{C},k}^{\mathrm{L}} = \int_0^{\infty} \int_0^{\infty} \frac{1 - \left(1 + \frac{z}{m_k}\right)^{-M_k m_k}}{z} \exp\left\{ -\frac{z}{\mathrm{SNR}_{\mathrm{L},k}(x)} - \sum_{j=1}^{K} Z_{\mathrm{C},k,j,\mathrm{L}}^{\mathrm{L}}(x,z) - \sum_{j=1}^{K} Z_{\mathrm{C},k,j,\mathrm{L}}^{\mathrm{NL}}(x,z) \right\} \times f_{X_{\mathrm{C},k}^{\mathrm{L}}}(x) \mathrm{d}z \mathrm{d}x, \tag{37}$$

$$\mathscr{R}_{\mathrm{C},k}^{\mathrm{NL}} = \int_0^{\infty} \int_0^{\infty} \frac{1 - (1+z)^{-M_k}}{z} \exp\left\{ -\frac{z}{\mathrm{SNR}_{\mathrm{NL},k}(x)} - \sum_{j=1}^{K} Z_{\mathrm{C},k,j,\mathrm{NL}}^{\mathrm{L}}(x,z) - \sum_{j=1}^{K} Z_{\mathrm{C},k,j,\mathrm{NL}}^{\mathrm{NL}}(x,z) \right\} \times f_{X_{\mathrm{C},k}^{\mathrm{NL}}}(x) \mathrm{d}z \mathrm{d}x, \tag{38}$$

where

$$Z_{\mathrm{C},k,j,s}^{t}(x,z) = 2\pi\lambda_j \int_{F_{\mathrm{C},k,j,s}^{t}(x)}^{\infty} Q_{k,j,s}^{t}(x,z,u) P_{t,j}(u) u \mathrm{d}u, \tag{39}$$

$\mathrm{SNR}_{\mathrm{L},k}(x)$, $\mathrm{SNR}_{\mathrm{NL},k}(x)$ *and* $Q_{k,j,s}^{t}(x,z,u)$ *have been given in Theorem 1.*

Proof. It follows similar proof as in Theorem 1. □

Corollary 2. *Suppose Φ_K is the small-cell tier with the minimum BS height and largest BS density, i.e., $\hat{H}_K < \hat{H}_j, \lambda_K > \lambda_j, j \in \mathscr{K}, j \neq K$, and $\hat{H}_K > 0$, the downlink ergodic rate under the closest BS cell-association strategy approaches to zero when $\lambda_K \to \infty$.*

Proof. It follows similar proof as in Corollary 1. □

4 Other Performance Metrics

In this section, we evaluate other important performance metrics of 3D HetNets with multi-antenna BSs using the ergodic rate expression developed in the previous section. First, we extend our analysis to the ASE metric. Then, we formulate the expression of energy efficiency.

4.1 Area Spectral Efficiency

The ASE is a performance metric used to evaluate the network throughput and the potential gain of deploying more SBSs, which is defined as the product of the BS density and the average data rate per cell [10].

Under the strongest received signal cell-association strategy, the ASE of a 3D HetNet with multi-antenna BSs in nats/s/Hz/m^2 is given by [24]

$$ASE_{\mathrm{S}} = \sum_{k=1}^{K} \lambda_k \mathscr{R}_{\mathrm{S}}. \tag{40}$$

Under the closest BS cell-association strategy, the ASE of a 3D HetNet with multi-antenna BSs in nats/s/Hz/m^2 is given by

$$ASE_{\mathrm{C}} = \sum_{k=1}^{K} \lambda_k \mathscr{R}_{\mathrm{C}}. \tag{41}$$

4.2 Energy Efficiency

On the one hand, network densification improves the network capacity. On the other hand, the deployment of SBSs and multi-antenna systems requires more hardware infrastructure, resulting in higher power consumption of cellular networks. Hence, energy efficiency is another important performance metric. The energy efficiency is defined as the ratio of the ASE and the power consumption per unit area. The total power consumption per unit area in a 3D HetNet

with multi-antenna BSs is computed in W/m^2 by [29]

$$P_{\text{total}} = \sum_{k=1}^{K} \lambda_k \rho_k \left(M_k P_{\text{C},k} + \frac{P_k}{\eta_k} \right), \tag{42}$$

where $P_{\text{C},k}$ is the circuit power per antenna in the k^{th} tier, η_k is the power amplifier efficiency of the k^{th}-tier BSs, and ρ_k is a parameter related to the power loss rate of the DC-DC converter, current supply and cooling.

Combining (40) and (42), under the strongest received signal cell-association strategy, the energy efficiency of a 3D HetNet with multi-antenna BSs can be formulated in nats/s/Hz/W as follows

$$EE_{\text{S}} = \frac{ASE_{\text{S}}}{P_{\text{total}}} = \frac{\sum_{k=1}^{K} \lambda_k \mathscr{R}_{\text{S}}}{\sum_{k=1}^{K} \lambda_k \rho_k \left(M_k P_{\text{C},k} + \frac{P_k}{\eta_k} \right)}. \tag{43}$$

Similarly, combining (41) and (42), under the closest BS cell-association strategy, the energy efficiency of a 3D HetNet with multi-antenna BSs can be formulated in nats/s/Hz/W as follows

$$EE_{\text{C}} = \frac{ASE_{\text{C}}}{P_{\text{total}}} = \frac{\sum_{k=1}^{K} \lambda_k \mathscr{R}_{\text{C}}}{\sum_{k=1}^{K} \lambda_k \rho_k \left(M_k P_{\text{C},k} + \frac{P_k}{\eta_k} \right)}. \tag{44}$$

5 Numerical Results

In this section, we present numerical results for the ergodic rate, ASE and energy efficiency in 3D HetNets with multi-antennas and then study the deployment of SBSs in 3D HetNets. We consider a two-tier HetNet where the 1$^{\text{st}}$ tier is the macrocell tier and the 2$^{\text{nd}}$ tier is the small-cell tier. The default numerical simulation parameter values are listed in Table 2 unless otherwise stated, which are set according to Table A.2.1.1.2-3 of [30] and [26, 31–33]. We verify the analytical results through Monte-Carlo simulations on a 2km$\times$2km area with 10^5 random trials.

Table 2 Values of Parameters

Parameters	**Default Values**
H_1, H_2, H_{U}	30 m, 5 m, 1.5 m
$\overline{L}_{\mathrm{b}}$, $\overline{W}_{\mathrm{b}}$, $\overline{H}_{\mathrm{b}}$	15 m, 15 m, 10 m
λ_1, λ_2, λ_{b}	2×10^{-6}, 10^{-3}, 10^{-3} $\left(1/\mathrm{m}^2\right)$
C_1, C_2	1, 1
α_1^{L}, α_1^{NL}	2.42, 4.28
α_2^{L}, α_2^{NL}	2.09, 3.75
β_1^{L}, β_1^{NL}	$10^{-10.34}$, $10^{-13.11}$
β_2^{L}, β_2^{NL}	$10^{-10.38}$, $10^{-14.54}$
M_1, M_2	64, 4
P_1, P_2	53 dBm, 33 dBm
δ_k^2 $\forall k$	-95 dBm
m_k $\forall k$	3
$P_{\mathrm{C},1}$, $P_{\mathrm{C},2}$	20.7 W, 2.1 W
η_1, η_2	0.388, 0.08
ρ_1, ρ_2	1.25, 1.21

5.1 Effect of the Number of Antennas per SBS

In Fig. 2, we show the ergodic rate against the number of antennas per SBS for $H_2 = 5$ m and $H_2 = 15$ m, respectively. First of all, the analytical expressions match with simulation curves exactly, which implies the accuracy of our analytical results. In the following, two interesting insights can be obtained. For one thing, regardless of the SBS height, the ergodic rate of the 3D HetNet always increases when deploying more antennas per SBS. For another, the strongest received signal cell-association strategy provides higher ergodic rate than the closest BS cell-association strategy and the gap expands as the number of antennas increases. Moreover, we can see that for the default SBS density, 2D cases overestimate the network performance in terms of the ergodic rate, indicating the importance of considering BS heights. Notice that the conclusion may be different when the BS antennas are deployed in 2D arrays and vertical beamforming is performed.

Fig. 3 shows the impact of the number of antennas per SBS on the energy efficiency. It can be observed that regardless of the SBS height, the energy efficiency first increases rapidly with

the increment of number of antennas per SBS until reaching a peak, after which the increase turns into a decline. This is because adding more antennas at the beginning significantly improves the ergodic rate, while the gain of deploying more antennas decreases with M_2. However, the energy consumption scales linearly with M_2. Moreover, we observe that the critical number of antennas per SBS, i.e., the optimal M_2 that maximizes the energy efficiency increases with the increment of SBS height.

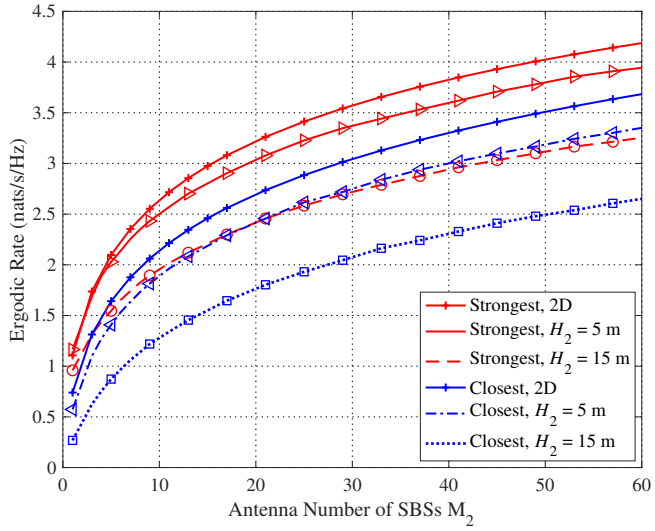

Fig. 2 Ergodic rate versus M_2. For 3D cases, lines and markers denote analytical results and simulation results, respectively.

5.2 Effects of SBS Density

In Fig. 4, we show the ergodic rate against the SBS density for $H_2 = 1.5$ m, $H_2 = 5$ m and $H_2 = 15$ m, respectively. We can see that the ergodic rate monotonically decreases with the increasing SBS density regardless of the cell-association strategy and SBS height. This is different from the observation in a single-tier network where the network coverage probability first increases and then decreases with the BS density [9]. In the presence of MBSs with high transmission power and large antenna arrays, the HetNet is already interference-limited. Hence, adding more SBSs only leads to more LOS interference links that deteriorate the ergodic rate. We also find that when SBSs are higher than UEs ($H_2 > 1.5$ m), the ergodic rate decays

towards zero with the network densification, which coincides with the conclusions of Corollary 1 and Corollary 2. This is because as $\lambda_2 \to \infty$, when $H_2 > 1.5$ m, the desired received power approaches to a constant while the extremely high aggregated interference becomes dominant, leading to extremely low SINR and ergodic rate.

In Fig. 5, we show the ASE for different values of SBS height. We note that for both cell-association strategies, when $H_2 = 1.5$ m, the ASE monotonically increases with the SBS density. However, when $H_2 = 5$ m and $H_2 = 15$ m, the ASE first increases linearly with the SBS density and then shows a slow growth caused by the height difference between SBSs and UEs. The $H_2 = 15$ m curve even suffers from a rapid decay under large SBS densities. Moreover, for a small value of SBS density, the ASE of the strongest received signal cell-association significantly outperforms that of the closest BS cell-association while the effect of BS height is negligible. In contrast, when the BS density becomes sufficiently large, the ASE is dominated by the SBS height. These observations highlight that SBSs should be deployed at the height of UEs in an ultra-dense HetNet for a high ASE. Fig. 4 and Fig. 5 show the tradeoff between ergodic rate and ASE. Although in most cases deploying more SBSs increases the ASE, it impairs the ergodic rate at the same time.

Fig. 6 shows the impact of the SBS density on the energy efficiency. It is interesting to observe that although the ergodic rate monotonically decreases with respect to the SBS density, the energy efficiency first increases rapidly with the SBS density, which indicates that in the presence of MBSs, the deployment of SBSs with low transmission power and circuit power can improve the system energy efficiency. However, when the SBS density exceeds a critical threshold, the energy efficiency begins to decrease since excessive SBSs significantly degrade the ergodic rate and cause high network energy consumption.

The results in Fig. 4, Fig. 5 and Fig. 6 reveal that at low to medium SBS densities, the closest BS cell-association strategy should be avoided regardless of the SBS height, and that at high SBS densities, under both considered cell-association strategies, SBSs should be deployed at the same height as UEs to obtain good network performance. Moreover, we can see that for most SBS densities, the network performance in terms of the ergodic rate, ASE and energy efficiency in traditional 2D network models is overestimated. In the practical deployment of

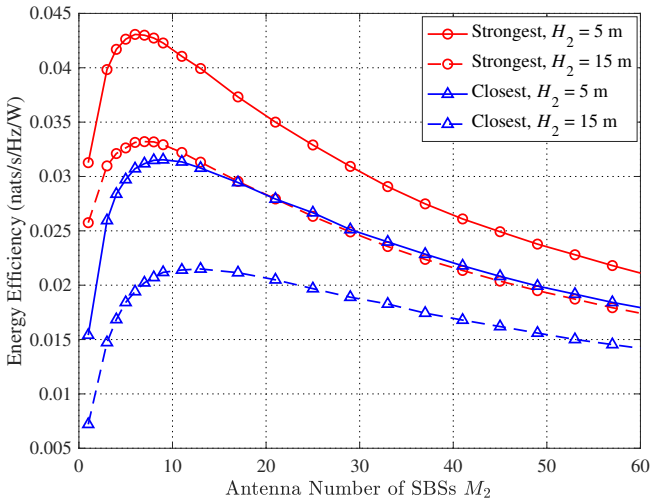

Fig. 3 Energy efficiency versus M_2 for different values of H_2.

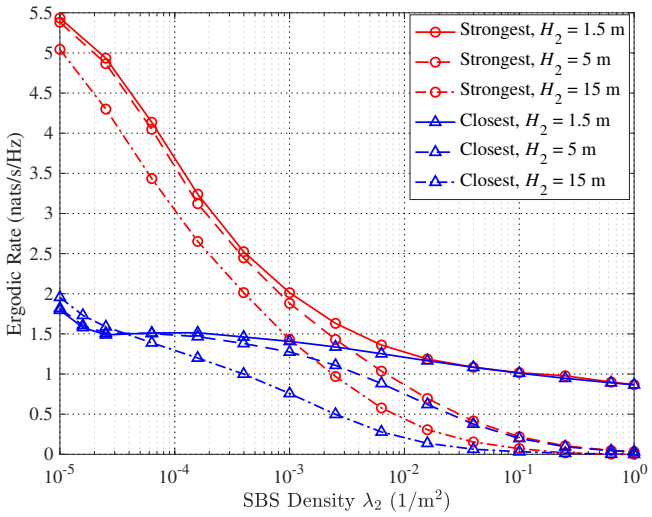

Fig. 4 Energy efficiency versus M_2 for different values of H_2.

SBSs, the tradeoff among ergodic rate, ASE and energy efficiency needs to be addressed by designing an optimization problem, e.g., maximizing the ASE while ensuring a certain ergodic rate and energy efficiency.

Fig. 7 shows the joint effects of SBS density and the number of antennas per SBS on the energy efficiency under the closest BS cell-association strategy. We can see that for given MBS configuration and SBS height, the SBS density and the number of antennas per SBS can be jointly optimized to maximize the energy efficiency.

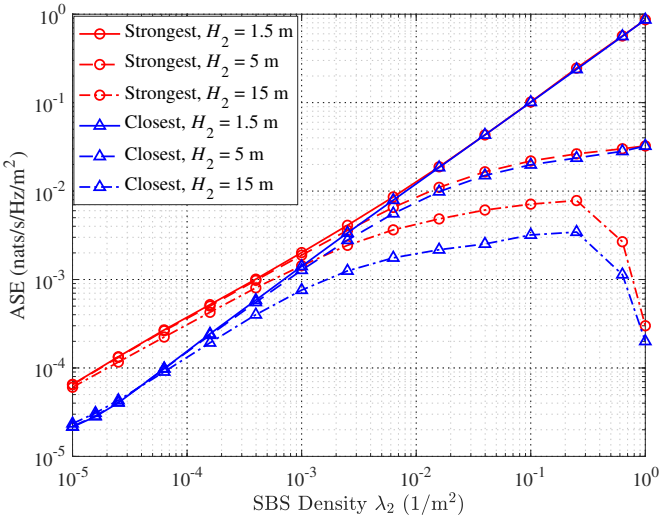

Fig. 5 ASE versus λ_2 for different values of H_2.

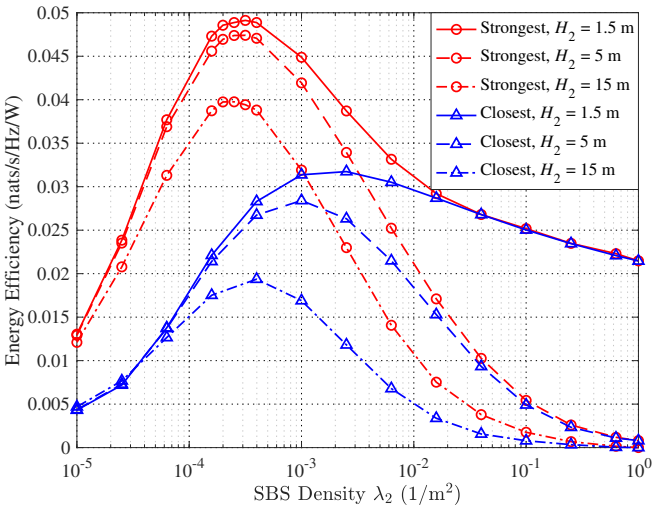

Fig. 6 Energy efficiency versus λ_2 for different values of H_2.

5.3 Effect of SBS Height

In Fig. 8, we analyze the effect of SBS height on the ergodic rate. Clearly the SBS height has a significant effect on the ergodic rate, which cannot be captured using traditional 2D HetNet models. Under the strongest received signal cell-association strategy, the ergodic rate monotonically decreases with the SBS height regardless of the SBS density. This is because elevated BSs lead to more LOS interference links. However, under the closest received signal

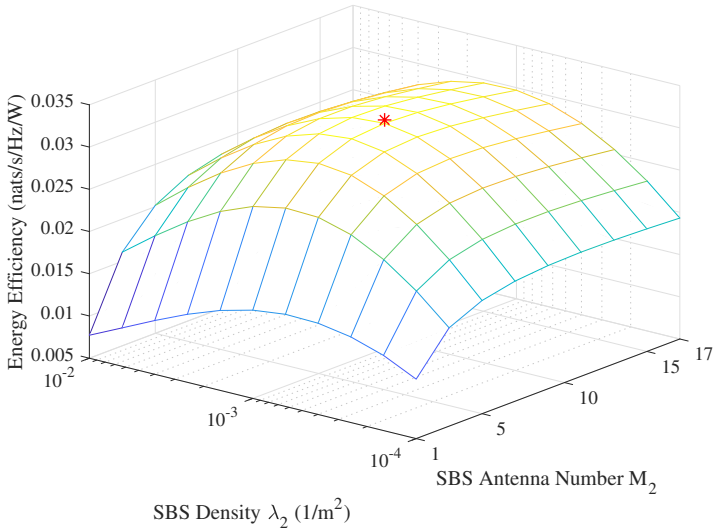

Fig. 7 Energy efficiency versus λ_2 and M_2. The marker denotes the maximum energy efficiency.

cell-association strategy, the trend of ergodic rate depends on the SBS density. More specifically, when $\lambda_2 = 10^{-5}$ BS/m^2, the ergodic rate always increases with the increment of SBS height, because when λ_2 approaches λ_1, the typical UE is more likely to be associated with the MBS providing the strongest received signal. As λ_2 increases to $\lambda_2 = 10^{-4}$ BS/m^2, the ergodic rate monotonically decreases with the SBS height as the loss caused by LOS interference links from elevated SBSs exceeds the gain of connecting to the best BS that provides the strongest received signal. When $\lambda_2 = 4 \times 10^{-5}$ BS/m^2, the ergodic rate almost remains unchanged due to the tradeoff between the aforementioned loss and gain.

5.4 Effect of Bias Factor

Fig. 9 presents the effect of SBS bias on the ergodic rate. Under the strongest received signal cell-association strategy, with the increase of SBS bias, the ergodic rate monotonically decreases with the SBS bias since each UE is more likely to miss the BS providing the strongest received signal, which reduces the SINR. In contrast, for the closest BS cell-association strategy, the ergodic rate first increases and then decreases with the SBS bias. This is because the increase of SBS bias first improves and then reduces the probability of associating with the BS providing

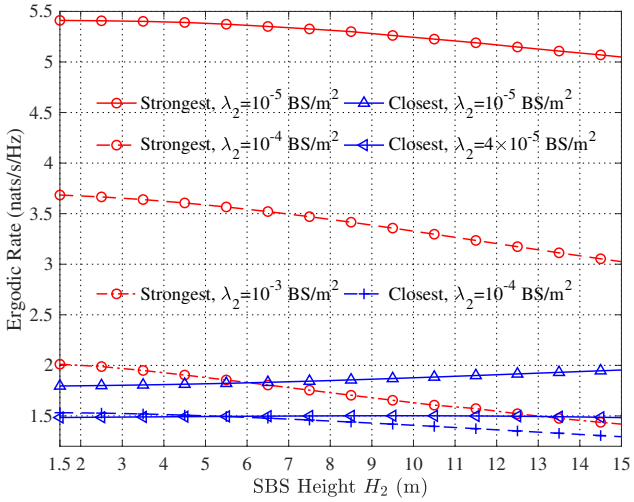

Fig. 8 Ergodic rate versus H_2 for different values of λ_2.

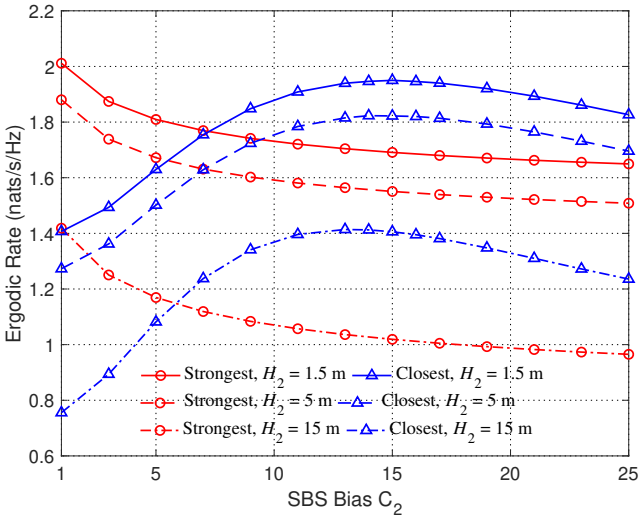

Fig. 9 Ergodic Rate versus C_2 for different values of H_2.

the strongest received signal for each UE. We can also note that the critical SBS bias, i.e., the optimal C_2 that maximizes the ergodic rate decreases with the increment of SBS height.

6 Conclusions

In this paper, we have proposed a novel stochastic geometry framework for a K-tier 3D HetNet incorporating the potentially different BS height, number of antennas per BS and

cell-association bias for each tier. Under both the strongest received signal and the closest BS cell-association strategies, we have derived the per-tier association probability, downlink ergodic rate, ASE and energy efficiency, the accuracy of which is verified by simulations. Our numerical results show that in an ultra-dense 3D HetNet, under both cell-association strategies, SBSs should be deployed at the height of UEs for achieving high ergodic rate, ASE and energy efficiency. We have also shown that increasing the number of antennas per SBS results in higher ergodic rate and energy efficiency, while excessive antennas impair the energy efficiency. Additionally, it has been observed that when other system parameters are fixed, the energy efficiency can be maximized by a joint optimization of the number of antennas per SBS and SBS density. The effect of cell-association bias has also been quantified. In our future work, we will extend the proposed 3D analytical model to mmWave HetNets while considering the effects of different beamforming techniques.

Appendix A

Under the strongest received signal cell-association strategy, denoting $R_k^{\mathrm{L}} = x$, the probability that the typical UE is connected to a LOS BS in the k^{th} tier is computed by

$$\begin{aligned}\mathscr{A}_{\mathrm{S},k}^{\mathrm{L}} &= \mathbb{E}_x\left[\mathbb{P}\left[P_{\mathrm{r},k}^{\mathrm{L}}(x) > \max_{j\in\mathscr{K}, j\neq k} P_{\mathrm{r},j}^{\mathrm{L}}\left(R_j^{\mathrm{L}}\right)\right]\mathbb{P}\left[P_{\mathrm{r},k}^{\mathrm{L}}(x) > \max_{j\in\mathscr{K}} P_{\mathrm{r},j}^{\mathrm{NL}}\left(R_j^{\mathrm{NL}}\right)\right]\right] \\ &= \mathbb{E}_x\left[\prod_{j\in\mathscr{K}, j\neq k}\mathbb{P}\left[P_{\mathrm{r},k}^{\mathrm{L}}(x) > P_{\mathrm{r},j}^{\mathrm{L}}\left(R_j^{\mathrm{L}}\right)\right]\prod_{j\in\mathscr{K}}\mathbb{P}\left[P_{\mathrm{r},k}^{\mathrm{L}}(x) > P_{\mathrm{r},j}^{\mathrm{NL}}\left(R_j^{\mathrm{NL}}\right)\right]\right],\end{aligned} \tag{45}$$

where

$$\begin{aligned}\mathbb{P}\left[P_{\mathrm{r},k}^{\mathrm{L}}(x) > P_{\mathrm{r},j}^{\mathrm{L}}\left(R_j^{\mathrm{L}}\right)\right] &\overset{(a)}{=} \mathbb{P}\left[\left(R_j^{\mathrm{L}}\right)^2 > \left(\Omega_{k,j,\mathrm{L}}^{\mathrm{L}}\right)^{-\frac{2}{\alpha_j^{\mathrm{L}}}}\left(x^2+\hat{H}_k^2\right)^{\frac{\alpha_k^{\mathrm{L}}}{\alpha_j^{\mathrm{L}}}} - \hat{H}_j^2\right] \\ &= \begin{cases} 1, & I_{k,j,\mathrm{L}}^{\mathrm{L}}(x) < 0, \\ e^{-2\pi\lambda_j\int_0^{\sqrt{I_{k,j,\mathrm{L}}^{\mathrm{L}}(x)}} P_{\mathrm{L},j}(u)u\mathrm{d}u}, & I_{k,j,\mathrm{L}}^{\mathrm{L}}(x) \geq 0, \end{cases}\end{aligned} \tag{46}$$

where $\Omega^{\mathrm{L}}_{k,j,\mathrm{L}}=\frac{P_k\beta^{\mathrm{L}}_k C_k}{P_j\beta^{\mathrm{L}}_j C_j}$ and $I^{\mathrm{L}}_{k,j,\mathrm{L}}(x)=\left(\Omega^{\mathrm{L}}_{k,j,\mathrm{L}}\right)^{-\frac{2}{\alpha^{\mathrm{L}}_j}}\left(x^2+\hat{H}^2_k\right)^{\frac{\alpha^{\mathrm{L}}_k}{\alpha^{\mathrm{L}}_j}}-\hat{H}^2_j$. Since $\left(R^{\mathrm{L}}_j\right)^2$ is always greater than 0, if $I^{\mathrm{L}}_{k,j,\mathrm{L}}(x)<0$, (a) will be equal to 1; otherwise, (a) can be computed using the void probability of PPP. When $I^{\mathrm{L}}_{k,j,\mathrm{L}}(x)<0$, we have $x<D^{\mathrm{L}}_{k,j,\mathrm{L}}$, where

$$D^{\mathrm{L}}_{k,j,\mathrm{L}}=\begin{cases}0, & \hat{H}_j^{\frac{\alpha^{\mathrm{L}}_j}{\alpha^{\mathrm{L}}_k}}\left(\Omega^{\mathrm{L}}_{k,j,\mathrm{L}}\right)^{\frac{1}{\alpha^{\mathrm{L}}_k}}<\hat{H}_k,\\ \sqrt{\hat{H}_j^{\frac{2\alpha^{\mathrm{L}}_j}{\alpha^{\mathrm{L}}_k}}\left(\Omega^{\mathrm{L}}_{k,j,\mathrm{L}}\right)^{\frac{2}{\alpha^{\mathrm{L}}_k}}-\hat{H}^2_k}, & \hat{H}_j^{\frac{\alpha^{\mathrm{L}}_j}{\alpha^{\mathrm{L}}_k}}\left(\Omega^{\mathrm{L}}_{k,j,\mathrm{L}}\right)^{\frac{1}{\alpha^{\mathrm{L}}_k}}\geq\hat{H}_k.\end{cases} \tag{47}$$

Defining that

$$F^{\mathrm{L}}_{\mathrm{S},k,j,\mathrm{L}}(x)=\begin{cases}0, & x<D^{\mathrm{L}}_{k,j,\mathrm{L}},\\ \sqrt{\left(\Omega^{\mathrm{L}}_{k,j,\mathrm{L}}\right)^{-\frac{2}{\alpha^{\mathrm{L}}_j}}\left(x^2+\hat{H}^2_k\right)^{\frac{\alpha^{\mathrm{L}}_k}{\alpha^{\mathrm{L}}_j}}-\hat{H}^2_j}, & x\geq D^{\mathrm{L}}_{k,j,\mathrm{L}},\end{cases} \tag{48}$$

(46) can be rewritten as

$$\mathbb{P}\left[P^{\mathrm{L}}_{\mathrm{r},k}(x)>P^{\mathrm{L}}_{\mathrm{r},j}\left(R^{\mathrm{L}}_j\right)\right]=e^{-2\pi\lambda_j\int_0^{F^{\mathrm{L}}_{\mathrm{S},k,j,\mathrm{L}}(x)}P_{\mathrm{L},k}(u)u\mathrm{d}u}. \tag{49}$$

Similarly, we have

$$\mathbb{P}\left[P^{\mathrm{L}}_{\mathrm{r},k}(x)>P^{\mathrm{NL}}_{\mathrm{r},j}\left(R^{\mathrm{NL}}_j\right)\right]=e^{-2\pi\lambda_j\int_0^{F^{\mathrm{NL}}_{\mathrm{S},k,j,\mathrm{L}}(x)}P_{\mathrm{NL},k}(u)u\mathrm{d}u}, \tag{50}$$

where

$$F^{\mathrm{NL}}_{\mathrm{S},k,j,\mathrm{L}}(x)=\begin{cases}0, & x<D^{\mathrm{NL}}_{k,j,\mathrm{L}},\\ \sqrt{\left(\Omega^{\mathrm{NL}}_{k,j,\mathrm{L}}\right)^{-\frac{2}{\alpha^{\mathrm{NL}}_j}}\left(x^2+\hat{H}^2_k\right)^{\frac{\alpha^{\mathrm{L}}_k}{\alpha^{\mathrm{NL}}_j}}-\hat{H}^2_j}, & x\geq D^{\mathrm{NL}}_{k,j,\mathrm{L}},\end{cases} \tag{51}$$

$\Omega_{k,j,\mathrm{L}}^{\mathrm{NL}} = \frac{P_k \beta_k^{\mathrm{L}} C_k}{P_j \beta_j^{\mathrm{NL}} C_j}$, and

$$D_{k,j,\mathrm{L}}^{\mathrm{NL}} = \begin{cases} 0, & \hat{H}_j^{\frac{\alpha_j^{\mathrm{NL}}}{\alpha_k^{\mathrm{L}}}} \left(\Omega_{k,j,\mathrm{L}}^{\mathrm{NL}}\right)^{\frac{1}{\alpha_k^{\mathrm{L}}}} < \hat{H}_k, \\ \sqrt{\hat{H}_j^{\frac{2\alpha_j^{\mathrm{NL}}}{\alpha_k^{\mathrm{L}}}} \left(\Omega_{k,j,\mathrm{L}}^{\mathrm{NL}}\right)^{\frac{2}{\alpha_k^{\mathrm{L}}}} - \hat{H}_k^2}, & \hat{H}_j^{\frac{\alpha_j^{\mathrm{NL}}}{\alpha_k^{\mathrm{L}}}} \left(\Omega_{k,j,\mathrm{L}}^{\mathrm{NL}}\right)^{\frac{1}{\alpha_k^{\mathrm{L}}}} \geq \hat{H}_k. \end{cases} \tag{52}$$

Plugging (49) and (50) into (45), (10) is obtained. $\mathscr{A}_{\mathrm{S},k}^{\mathrm{NL}}$ can be derived following the similar steps, which concludes our proof.

Appendix B

Recall that the ergodic rate under the strongest received signal cell-association strategy is computed by

$$\mathscr{R}_{\mathrm{S}} = \sum_{k=1}^{K} \left(\mathbb{E}\left[\log\left(1+\mathrm{SINR}_{\mathrm{S},k}^{\mathrm{L}}\right)\right] \mathscr{A}_{\mathrm{S},k}^{\mathrm{L}} + \mathbb{E}\left[\log\left(1+\mathrm{SINR}_{\mathrm{S},k}^{\mathrm{NL}}\right)\right] \mathscr{A}_{\mathrm{S},k}^{\mathrm{NL}} \right), \tag{53}$$

where

$$\begin{aligned} &\mathbb{E}\left[\log\left(1+\mathrm{SINR}_{\mathrm{S},k}^{\mathrm{L}}\right)\right] \\ &= \mathbb{E}_x\left[\mathbb{E}\left[\log\left(1+\frac{P_k \beta_k^{\mathrm{L}} h_k^{\mathrm{L}} \left(x^2+\hat{H}_k^2\right)^{-\alpha_k^{\mathrm{L}}/2}}{I_{\mathrm{S},k,\mathrm{L}}^{\mathrm{L}} + I_{\mathrm{S},k,\mathrm{L}}^{\mathrm{NL}} + \delta_k^2}\middle| R_k^{\mathrm{L}} = x\right)\right]\right] \\ &= \int_0^{\infty} \mathbb{E}\left[\log\left(1+\frac{P_k \beta_k^{\mathrm{L}} h_k^{\mathrm{L}} \left(x^2+\hat{H}_k^2\right)^{-\alpha_k^{\mathrm{L}}/2}}{I_{\mathrm{S},k,\mathrm{L}}^{\mathrm{L}} + I_{\mathrm{S},k,\mathrm{L}}^{\mathrm{NL}} + \delta_k^2}\middle| R_k^{\mathrm{L}} = x\right)\right] f_{X_{\mathrm{S},k}^{\mathrm{L}}}(x)\mathrm{d}x. \end{aligned} \tag{54}$$

Before further derivation, we introduce an important Lemma [34] as follows. For independent random variables X and Y ($X \geq 0$ and $Y \geq 0$), we have

$$\mathbb{E}_{X,Y}\left(\log\left(1+\frac{X}{Y}\right)\right) = \int_0^{\infty} \left(1-\mathscr{L}_X(z)\right)\mathscr{L}_Y(z)\frac{\mathrm{d}z}{z}, \tag{55}$$

where $\mathscr{L}_X(z)$ denotes the Laplace transform of X at z. Applying (55) into (54), we have

$$\begin{aligned}&\mathbb{E}\left[\log\left(1+\frac{P_k\beta_k^{\mathrm{L}}h_k^{\mathrm{L}}\left(x^2+\hat{H}_k^2\right)^{-\alpha_k^{\mathrm{L}}/2}}{I_{\mathrm{S},k,\mathrm{L}}^{\mathrm{L}}+I_{\mathrm{S},k,\mathrm{L}}^{\mathrm{NL}}+\delta_k^2}\middle| R_k^{\mathrm{L}}=x\right)\right]\\&=\int_0^\infty\left(1-\mathscr{L}_{h_k^{\mathrm{L}}}(z)\right)\mathscr{L}_I(z)\exp\left\{-\frac{z}{\mathrm{SNR}_{\mathrm{L},k}(x)}\right\}\frac{\mathrm{d}z}{z},\end{aligned}\tag{56}$$

where $\mathrm{SNR}_{\mathrm{L},k}(x)=\frac{P_k\beta_k^{\mathrm{L}}\left(x^2+\hat{H}_k^2\right)^{-\alpha_k^{\mathrm{L}}/2}}{\delta_k^2}$, $\mathscr{L}_{h_k^{\mathrm{L}}}(z)=\mathbb{E}_{h_k^{\mathrm{L}}}\left[e^{-h_k^{\mathrm{L}}z}\right]=\left(1+\frac{z}{m_k}\right)^{-M_km_k}$, and $\mathscr{L}_I(z)=\mathscr{L}_{I_{\mathrm{L}}}(z)\mathscr{L}_{I_{\mathrm{NL}}}(z)$, where

$$\begin{aligned}\mathscr{L}_{I_{\mathrm{L}}}(z)&=\mathbb{E}\left[\exp\left\{-\frac{I_{\mathrm{S},k,\mathrm{L}}^{\mathrm{L}}\left(x^2+\hat{H}_k^2\right)^{\alpha_k^{\mathrm{L}}/2}z}{P_k\beta_k^{\mathrm{L}}}\right\}\right]\\&=\mathbb{E}\left[\exp\left\{-\sum_{j\in\mathscr{K}}\sum_{i\in\Phi_j^{\mathrm{L}}\setminus B_{\mathrm{S},k}^{\mathrm{L}}}\frac{P_j\beta_j^{\mathrm{L}}g_j^{\mathrm{L}}\left(x^2+\hat{H}_k^2\right)^{\alpha_k^{\mathrm{L}}/2}z}{P_k\beta_k^{\mathrm{L}}\left(r_{i,j}^2+\hat{H}_j^2\right)^{\alpha_j^{\mathrm{L}}/2}}\right\}\right]\\&=\prod_{j\in\mathscr{K}}\mathbb{E}_{\Phi_j^{\mathrm{L}},g_j^{\mathrm{L}}}\left[\exp\left\{-\sum_{i\in\Phi_j^{\mathrm{L}}\setminus B_{\mathrm{S},k}^{\mathrm{L}}}\frac{P_j\beta_j^{\mathrm{L}}g_j^{\mathrm{L}}\left(x^2+\hat{H}_k^2\right)^{\alpha_k^{\mathrm{L}}/2}z}{P_k\beta_k^{\mathrm{L}}\left(r_{i,j}^2+\hat{H}_j^2\right)^{\alpha_j^{\mathrm{L}}/2}}\right\}\right].\end{aligned}\tag{57}$$

Defining that $\Delta_{\mathrm{L}}(x,z,u)=\frac{P_j\beta_j^{\mathrm{L}}\left(x^2+\hat{H}_k^2\right)^{\alpha_k^{\mathrm{L}}/2}z}{P_k\beta_k^{\mathrm{L}}\left(r_{i,j}^2+\hat{H}_j^2\right)^{\alpha_j^{\mathrm{L}}/2}}$, (57) can be derived as

$$\begin{aligned}\mathscr{L}_{I_{\mathrm{L}}}(z)&\overset{(a)}{=}\prod_{j\in\mathscr{K}}\exp\left\{-2\pi\lambda_j\int_{F_{\mathrm{S},k,j,\mathrm{L}}^{\mathrm{L}}(x)}^\infty\left(1-\mathbb{E}_{g_j^{\mathrm{L}}}\left[e^{-g_j^{\mathrm{L}}\Delta_{\mathrm{L}}(x,z,u)}\right]\right)P_{\mathrm{L},j}(u)u\mathrm{d}u\right\}\\&\overset{(b)}{=}\prod_{j\in\mathscr{K}}\exp\left\{-2\pi\lambda_j\int_{F_{\mathrm{S},k,j,\mathrm{L}}^{\mathrm{L}}(x)}^\infty\left(1-\left[1+\frac{\Delta_{\mathrm{L}}(x,z,u)}{m_j}\right]^{-m_j}\right)P_{\mathrm{L},j}(u)u\mathrm{d}u\right\},\end{aligned}\tag{58}$$

where (a) comes from the probability generating functional of PPP, in which the lower bound of the integral is the minimum horizontal distance between the interfering LOS BS in the j^{th} tier and the typical UE, and (b) comes from the moment generating function of the gamma random variable g_j^{L}.

Similarly, $\mathscr{L}_{I_{\mathrm{NL}}}(z)$ can be derived as

$$\begin{aligned}\mathscr{L}_{I_{\mathrm{NL}}}(z) &= \prod_{j\in\mathscr{K}} \exp\left\{ -2\pi\lambda_j \int_{F^{\mathrm{NL}}_{\mathrm{S},k,j,\mathrm{L}}(x)}^{\infty} \left(1-\mathbb{E}_{g_j^{\mathrm{NL}}}\left[e^{-g_j^{\mathrm{NL}}\Delta_{\mathrm{NL}}(x,z,u)}\right]\right) P_{\mathrm{NL},j}(u)u\mathrm{d}u \right\} \\ &\overset{(a)}{=} \prod_{j\in\mathscr{K}} \exp\left\{ -2\pi\lambda_j \int_{F^{\mathrm{NL}}_{\mathrm{S},k,j,\mathrm{L}}(x)}^{\infty} \left(1-\left[1+\Delta_{\mathrm{NL}}(x,z,u)\right]^{-1}\right) P_{\mathrm{NL},j}(u)u\mathrm{d}u \right\}, \end{aligned} \tag{59}$$

where (a) comes from the moment generating function of the exponential random variable g_j^{NL}. Plugging (56), (58) and (59) into (54), (31) can be obtained. $\mathscr{R}^{\mathrm{NL}}_{\mathrm{S},k}$ can be derived following the similar steps, which concludes our proof.

Appendix C

When $\lambda_K \to \infty$, the typical UE almost always connects to the K^{th} tier and the signals from other tiers can be omitted. Moreover, as $\lambda_K \to \infty$, both the desired and strong interfering signals almost certainly come from LOS BSs, and the effects of noise and NLOS interferers can be omitted [35]. Hence, the ergodic rate can be approximated by

$$\mathscr{R}_{\mathrm{S}} \approx \widetilde{\mathscr{R}}_{\mathrm{S}} = \mathbb{E}\left[\log\left(1+\mathrm{SINR}^{\mathrm{L}}_{\mathrm{S,D},K}\right)\right], \tag{60}$$

where

$$\mathrm{SINR}^{\mathrm{L}}_{\mathrm{S,D},K} = \frac{h^{\mathrm{L}}_K \left[\left(R^{\mathrm{L}}_K\right)^2 + \hat{H}^2_K\right]^{-\alpha^{\mathrm{L}}_K/2}}{\sum_{i\in\Phi^{\mathrm{L}}_K} g^{\mathrm{L}}_K \left(r^2_{i,K} + \hat{H}^2_K\right)^{-\alpha^{\mathrm{L}}_K/2}}. \tag{61}$$

Combining (60) and (61), and applying (55), we have

$$
\begin{aligned}
&\widetilde{\mathscr{R}}_{\mathrm{S}} \\
&= \mathbb{E}_x\left[\mathbb{E}\left[\log\left(1+\frac{h_K^{\mathrm{L}}\left[x^2+\hat{H}_K^2\right]^{-\frac{\alpha_K^{\mathrm{L}}}{2}}}{\sum_{i\in\Phi_K^{\mathrm{L}}} g_K^{\mathrm{L}}\left(r_{i,K}^2+\hat{H}_K^2\right)^{-\frac{\alpha_K^{\mathrm{L}}}{2}}}\middle| R_K^{\mathrm{L}}=x\right)\right]\right] \\
&= \int_0^{\infty}\int_0^{\infty} \frac{1-\left(1+\frac{z}{m_k}\right)^{-M_k m_k}}{z} 2\pi\lambda_K x e^{-\pi\lambda_K x^2} \\
&\quad \times e^{-2\pi\lambda_K \int_x^{\infty}\left(1-\left(1+\frac{z\left(x^2+\hat{H}_K^2\right)^{\alpha_K^{\mathrm{L}}/2}}{m_K\left(u^2+\hat{H}_K^2\right)^{\alpha_K^{\mathrm{L}}/2}}\right)^{-m_K}\right) u\mathrm{d}u} \mathrm{d}z\mathrm{d}x \\
&= \int_0^{\infty} \frac{\left[1-\left(1+\frac{z}{m_k}\right)^{-M_k m_k}\right] e^{-\pi\lambda_K \mathscr{K}(z,\alpha_K^{\mathrm{L}},m_K)\hat{H}_K^2}}{z\left[\mathscr{K}(z,\alpha_K^{\mathrm{L}},m_K)+1\right]} \mathrm{d}z,
\end{aligned} \tag{62}
$$

where $\mathscr{K}(z,\alpha_K^{\mathrm{L}},m_K) = {}_2F_1\left[-\frac{2}{\alpha_K^{\mathrm{L}}}, m_K; 1-\frac{2}{\alpha_K^{\mathrm{L}}}; -\frac{z}{m_K}\right] - 1$, and ${}_2F_1[\cdot]$ denotes the Gauss hypergeometric function. From (62), we can obtain that when $\lambda_K \to \infty$, $\widetilde{\mathscr{R}}_{\mathrm{S}} \to 0$, which completes our proof.

Acknowledgment

This project has received funding from the European Union Horizon 2020 research and innovation program under the Marie Sklodowska-Curie grant agreement No. 766231 WAVECOMBE H2020-MSCA-ITN-2017.

References

[1] J. G. Andrews *et al*., "What will 5G be?" *IEEE J. Sel. Areas Commun.*, vol. 32, no. 6, pp. 1065-1082, Jun. 2014.

[2] D. López-Pérez, M. Ding, H. Claussen, and A. H. Jafari, "Towards 1 Gbps/UE in cellular systems: Understanding ultra-dense small cell deployments," *IEEE Commun. Surveys Tuts.*, vol. 17, no. 4, pp. 2078–2101, 4th Quart. 2015.

[3] J. G. Andrews, X. Zhang, G. D. Durgin and A. K. Gupta, "Are we approaching the fundamental limits of wireless network densification?" *IEEE Commun. Mag.,* vol. 54, no. 10, pp. 184-190, Oct. 2016.

[4] C. Chen, Y. Zhang, J. Zhang, X. Chu and J. Zhang, "On the Performance of Indoor Multi-Story Small-Cell Networks," *IEEE Trans. Wireless Commun.,* vol. 20, no. 2, pp. 1336-1348, Feb. 2021.

[5] M. Kamel, W. Hamouda and A. Youssef, "Ultra-dense networks: a survey," *IEEE Commun. Surveys Tut.,* vol. 18, no. 4, pp. 2522-2545, Fourthquarter 2016.

[6] H. S. Dhillon, R. K. Ganti, F. Baccelli, and J. G. Andrews, "Modeling and analysis of K-tier downlink heterogeneous cellular networks," *IEEE J. Sel. Areas Commun.,* vol. 30, no. 3, pp. 550-560, Apr. 2012.

[7] X. Wang, E. Turgut and M. C. Gursoy, "Coverage in downlink heterogeneous mmWave cellular networks with user-centric small cell deployment," *IEEE Trans. Veh. Technol.,* vol. 68, no. 4, pp. 3513-3533, Apr. 2019.

[8] Y. Zhong, T. Q. S. Quek and X. Ge, “Heterogeneous cellular networks with spatio-temporal traffic: delay analysis and scheduling,” *IEEE J. Sel. Areas Commun.,* vol. 35, no. 6, pp. 1373-1386, Jun. 2017.

[9] M. Ding and D. López-Pérez, “Performance impact of base station antenna heights in dense cellular networks,” *IEEE Trans. Wireless Commun.,* vol. 16, no. 12, pp. 8147-8161, Dec. 2017.

[10] E. Björnson, L. Sanguinetti and M. Kountouris, “Deploying dense networks for maximal energy efficiency: small cells meet massive MIMO,” *IEEE J. Sel. Areas Commun.,* vol. 34, no. 4, pp. 832-847, April. 2016.

[11] H. Jo, Y. J. Sang, P. Xia and J. G. Andrews, “Heterogeneous cellular networks with flexible cell association: a comprehensive downlink SINR analysis,” *IEEE Trans. Wireless Commun.,* vol. 11, no. 10, pp. 3484-3495, Oct. 2012.

[12] E. Turgut and M. C. Gursoy, "Coverage in heterogeneous downlink millimeter wave cellular networks," *IEEE Trans. Commun.,* vol. 65, no. 10, pp. 4463-4477, Oct. 2017.

[13] A. K. Gupta, H. S. Dhillon, S. Vishwanath and J. G. Andrews, "Downlink multi-antenna heterogeneous cellular network with load balancing," *IEEE Trans. Commun.,* vol. 62, no. 11, pp. 4052-4067, Nov. 2014.

[14] D. C. Chen, T. Q. S. Quek and M. Kountouris, "Backhauling in heterogeneous cellular networks: modeling and tradeoffs,"*IEEE Trans. Wireless Commun.,* vol. 14, no. 6, pp. 3194-3206, Jun. 2015.

[15] W. Sun, L. Wang, J. Liu, N. Kato and Y. Zhang, “Movement aware CoMP handover in heterogeneous ultra-dense networks,” *IEEE Trans. Commun.,* vol. 69, no. 1, pp. 340-352, Jan. 2021.

[16] S. Bachtobji, A. Omri and R. Bouallegue, “Modelling and performance analysis of 3-D mmWaves based heterogeneous networks,” *2016 International Wireless Communications and Mobile Computing Conference (IWCMC)*, Paphos, 2016, pp. 72-76.

[17] A. Omri and M. O. Hasna, "Modelling and performance analysis of 3-D heterogeneous cellular networks," *2016 IEEE International Conference on Communications (ICC)*, Kuala Lumpur, 2016, pp. 1-5.

[18] I. Atzeni, J. Arnau, and M. Kountouris, “Downlink cellular network analysis with LOS/NLOS propagation and elevated base stations,” *IEEE Trans. Wireless Commun.*, vol. 17, no. 1, pp. 142-156, Jan. 2018.

[19] J. Yang, M. Ding, G. Mao, Z. Lin, D. Zhang and T. H. Luan, “Optimal base station antenna downtilt in downlink cellular networks,” *IEEE Trans. Wireless Commun.*, vol. 18, no. 3, pp. 1779-1791, Mar. 2019.

[20] C. Chen, J. Zhang, X. Chu and J. Zhang, “On the optimal base-station height in mmWave small-cell networks considering cylindrical blockage effects,” *IEEE Trans. Veh. Technol.,* vol. 70, no. 9, pp. 9588-9592, Sept. 2021.

[21] M. Alzenad and H. Yanikomeroglu, "Coverage and rate analysis for vertical heterogeneous networks (VHetNets)," *IEEE Trans. Wireless Commun.*, vol. 18, no. 12, pp. 5643-5657, Dec. 2019.

[22] H. Wu, Z. Wei, Y. Hou, N. Zhang and X. Tao, “Cell-edge user offloading via flying UAV in non-uniform heterogeneous cellular networks,” *IEEE Trans. Wireless Commun.*, vol. 19, no. 4, pp. 2411-2426, April. 2020.

[23] D. Kim, J. Lee and T. Q. S. Quek, “Multi-layer unmanned aerial vehicle networks: modeling and performance analysis,” *IEEE Trans. Wireless Commun.*, vol. 19, no. 1, pp. 325-339, Jan. 2020.

[24] J. Liu, M. Sheng, R. Lyu and J. Li, "Performance analysis and optimization of UAV integrated terrestrial cellular network," *IEEE Internet Things J.*, vol. 6, no. 2, pp. 1841-1855, Apr. 2019.

[25] Y. Zeng, J. Lyu and R. Zhang, “Cellular-connected UAV: potential, challenges, and promising technologies,” *IEEE Wirel. Commun.*, vol. 26, no. 1, pp. 120-127, Feb. 2019.

[26] T. Bai, R. Vaze and R. W. Heath, "Analysis of blockage effects on urban cellular networks," *IEEE Trans. Wireless Commun.*, vol. 13, no. 9, pp. 5070-5083, Sept. 2014.

[27] C.-H. Lee and M. Haenggi, "Interference and outage in Poisson cognitive networks," *IEEE Trans. Wireless Commun.*, vol. 11, no. 4, pp. 1392–1401, Apr. 2012.

[28] A. M. Hunter, J. G. Andrews, and S. Weber, "Transmission capacity of ad hoc networks with spatial diversity," *IEEE Trans. Wireless Commun.*, vol. 7, no. 12, pp. 5058–5071, Dec. 2008.

[29] X. Ge, J. Yang, H. Gharavi and Y. Sun, "Energy efficiency challenges of 5G small cell networks," *IEEE Commun. Mag.,* vol. 55, no. 5, pp. 184-191, May. 2017.

[30] 3rd Generation Partnership Project (3GPP), "Further Advancements for E-UTRA Physical Layer Aspects (Release 9)," Mar. 2010, 3GPP TR 36.814 V9.0.0 (2010-03).

[31] Q. Zhang, H. H. Yang, T. Q. S. Quek and J. Lee, "Heterogeneous cellular networks with LoS and NLoS transmissions—the role of massive MIMO and small cells," *IEEE Trans. Wireless Commun.*, vol. 16, no. 12, pp. 7996-8010, Dec. 2017.

[32] B. Yang, G. Mao, X. Ge, M. Ding and X. Yang, "On the energy-efficient deployment for ultra-dense heterogeneous networks with NLoS and LoS transmissions," *IEEE Trans. Green Commun. Netw.*, vol. 2, no. 2, pp. 369-384, June. 2018.

[33] Wenjia Liu, Shengqian Han, Chenyang Yang and Chengjun Sun, "Massive MIMO or small cell network: Who is more energy efficient?," *2013 IEEE Wireless Communications and Networking Conference Workshops (WCNCW)*, 2013, pp. 24-29.

[34] K. A. Hamdi, "Capacity of MRC on correlated Rician fading channels," *IEEE Trans. Commun.*, vol. 56, no. 5, pp. 708-711, May. 2008.

[35] T. Bai, A. Alkhateeb and R. W. Heath, "Coverage and capacity of millimeter-wave cellular networks," *IEEE Commun. Mag.,* vol. 52, no. 9, pp. 70-77, Sept. 2014.

Paper III

On the Performance of Indoor Multi-Story Small-Cell Networks, co-authored with Y. Zhang, J. Zhang, X. Chu and J. Zhang. This paper has been published on IEEE Transactions on Wireless Communications, 2021.

I conceived the idea and carried out the numerical simulations and writing of the manuscript. Jiliang Zhang and I performed the mathematical analysis. Yixin Zhang, Jiliang Zhang, Xiaoli Chu and I contributed to the network modelling. Xiaoli Chu and Jie Zhang guided and supervised the work. All authors discussed the theoretical aspects and numerical results, and reviewed the manuscript.

On the Performance of Indoor Multi-storey Small-cell Networks

Chen Chen[1], Yixin Zhang[1], Jiliang Zhang[1], Xiaoli Chu[1], Jie Zhang[1,2]

[1] Department of Electronic and Electrical Engineering, the University of Sheffield, Sheffield, S10 2TN, UK

[2] Ranplan Wireless Network Design Ltd., Cambridge, CB23 3UY, UK

Abstract

Mobile data traffic has been largely generated indoors. However, indoor cellular networks have been studied either on a two-dimensional (2D) plane or as an intractable optimization problem for a multi-storey building. In this paper, we develop a tractable three-dimensional (3D) small-cell network (SCN) model for a multi-storey building. On each storey, the small-cell base stations (BS) are distributed following a 2D homogeneous Poisson point process (PPP). We analytically derive the downlink coverage probability, spectral efficiency (SE) and area spectral efficiency (ASE) for the indoor network as functions of the storey height, the penetration loss of the ceiling and the BS density. Our tractable expressions show that a higher penetration loss of the ceiling leads to a higher coverage probability and a higher SE. Meanwhile, with the increase of the storey height or the BS density, the downlink coverage probability first decreases and then increases after reaching a minimum value, indicating that certain values of storey height and BS density should be avoided for good indoor wireless coverage.

1 Introduction

The fifth generation (5G) of mobile networks is predicted to support 1000× mobile data traffic in the next decade[1]. According to [2][3], approximately 80% of the mobile data is generated indoors, while over 70% of the indoor traffic is carried by the outdoor cellular networks. Since outdoor-to-indoor coverage is prone to suffer from the high penetration loss of walls and other physical obstacles, it is of high necessity to deploy indoor small-cell base stations (BS)[4][5].

While the modelling and analysis of outdoor networks has been widely studied in recent years [6–11], there are still open questions regarding the performance of indoor cellular networks. The existing works mainly focus on the modelling of blockages including walls and random blockages on two-dimensional (2D) planes [12–17]. However, the study of indoor cellular networks in multi-storey buildings should not be limited to a 2D BS deployment.

In this paper, we present for the first time a tractable three-dimensional (3D) small-cell network (SCN) model for the multi-storey indoor environment by incorporating the storey height and the penetration loss of the ceiling. Then we derive the expressions for the coverage probability, spectral efficiency (SE) and area spectral efficiency (ASE) where the user association and inter-cell interference are considered. We analyze the effects of the storey height and the penetration loss of the ceiling on the coverage probability and SE, and provide useful guidelines for the indoor small-cell deployment and the design of a new building from the perspective of wireless communications [37].

1.1 Related Works

Stochastic geometry has been widely used to analyze the performance of cellular networks due to its mathematical tractability [18–22]. It was also employed to model networks for the indoor built environment, e.g. in [14], where the authors modeled the BSs and the center points of the walls as two independent homogeneous Poisson point process (PPP). The results showed that higher interior-wall attenuation values can provide higher coverage probability due to the reduced inter-cell interference. In [13], a binomial point process was adopted to model a finite-sized indoor network. Considering the larger antenna arrays and shorter transmission distances of millimeter wave (mm-Wave) networks, the authors assumed a triangle transmitter-receiver radiation area involving the effects of random blockages and calculated the bit error rate and outage probability. However, these works only considered a 2D BS deployment.

The authors of [23] extended the 2D PPP distribution of BSs to the 3D space with BS density in BSs/m^3 and employed the free space path loss channel model. It was shown that the 3D cellular network achieved a lower coverage probability compared with the traditional 2D models, but the influence of the BS density was not analyzed. In [24], the dual-slope path

loss model was applied in a 3D PPP model. The asymptotic analysis showed that the coverage probability would diminish to zero when the density of BSs goes to infinity. In [25], a 3D Poisson building model was proposed to model the correlated indoor shadowing. However, these 3D models cannot be applied to SCNs in the multi-storey in-building scenarios, where BSs on the same storey usually have the same height for the sake of simple deployment.

Most existing works on multi-storey BS deployment focused on some specific optimization problems [26–28]. For instance, the authors of [26] optimized the BS placement taking into account the power control. After reformulating the mixed-integer nonconvex problem into a convex problem, the optimal number and locations of the BSs were obtained. Nevertheless, no tractable models have been proposed to analyze SCNs in the multi-storey building scenarios.

Dense deployment of SCN is considered as one of the key techniques of 5G networks [32]. The traditional understanding of network densification is that the increase of BS density does not change the coverage probability of the typical user in an interference limiting scenario [18][29]. This conclusion indicates that the area spectral efficiency scales linearly with the BS density, namely the capacity gain can always be obtained. However, it is worth noting that this result is based on the simplified free space propagation channel model. Considering the short-range propagation in dense SCNs, the authors in [30][31] proposed a bounded path loss model and showed that the ultra dense network degrades the spatial throughput. In [33], a multi-slope path loss model was employed to study the effect of non-line-of-sight (NLoS) transmission on the coverage probability. Their results showed that when the BS density increases above a certain value, the coverage probability starts to decrease and the increase in ASE slows down. In [34], the authors studied the effect of the height of BS antennas on the coverage probability and the ASE, which decrease to zero with the BS density when the BSs are higher than the users.

1.2 Contributions

In this paper, we study the performance of a 3D SCN in a multi-storey building. The main contributions of this paper are summarized as follows:

- We propose a novel 3D SCN model for a multi-storey building where BSs on each storey follow PPP distribution. Using tools from stochastic geometry, we derive the analytical expressions of coverage probability and SE for a building with $2M+1$ storeys, where $M \geq 1$.

- Based on the results above, the numerically tractable integral expressions for the $M = 1$ case are obtained and validated by simulation results. The numerical results show that the $M = 1$ case shows similar performance in terms of coverage probability and SE as the $M > 1$ cases, therefore our analytical expressions for the $M = 1$ case can be used to numerically predict the coverage probability and SE of a SCN in a building with $2M+1$ storeys, where $M \geq 1$.

- With our analytical results, we find that both the coverage probability and SE first decrease and then increase with the increasing storey height. Accordingly, we identify a range of storey heights associated with poor network performance that should be avoided in the design of a new building. Moreover, our results show that both the coverage probability and SE first decrease and then increase with the BS density on each storey. This new finding is different from previous results obtained under the 2D scenarios [18][19]. It indicates that the setting of BS density per storey in a multi-storey building should avoid the values that result in poor coverage.

1.3 Paper Organization

The remainder of this paper is structured as follows. Section 2 introduces the system model. Section 3 gives the analytical results on the coverage probability. Section 4 presents the analytical results on the spectral efficiency. The numerical results are discussed in Section 5, with remarks shedding some new light on the deployment of dense SCN. Finally, the conclusions are drawn in Section 6.

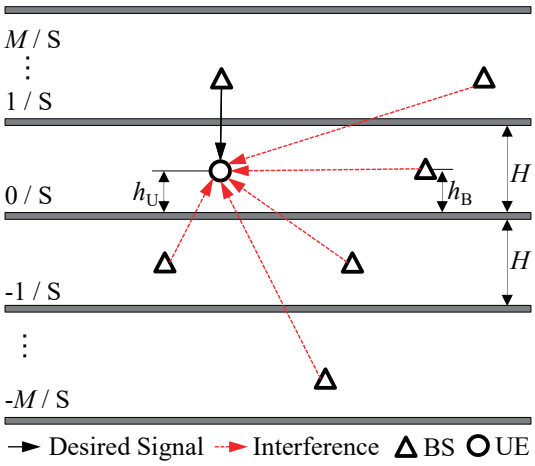

Fig. 1 An illustration of the small-cell network in a multi-storey building.

2 System Model

Consider $2M+1$ storeys of a multi-storey building, where $M \geq 1$. Table 1 presents a summary of notations used. As shown in Fig. 1, all the storeys from the ground storey to the top storey are numbered from $-M$ to M, respectively, and we assume that the typical user is located on the 0th storey. Assume that on each storey, BSs and users have the same height h and the height for each storey is H. Notice that H includes the ceiling height and the ceiling thickness. For the jth storey, the small-cell BSs are randomly distributed following a homogeneous PPP Φ_j with intensity λ BSs/m^2 and users are also PPP distributed with a density of ρ users/m^2. For simplicity, we assume that the values of λ and ρ do not change across different storeys. In this work, we adopt PPP to model the BSs on each storey mainly for its higher analytical tractability as compared with other point processes (such as binomial point process and Poisson cluster process).

For the downlink cellular network, we assume that the desired and interference signals experience the distance dependent path loss, where the same path loss exponent α is used for all the storeys. Small scale fading is modeled as Rayleigh fading with an unit average power for all the channels [33, 35].

The simulation results in Fig. 3 in Section 5 will show that the maximum coverage probability is obtained when the BS height is the same as the UE height. For analytical

Table 1 Summary of Notations

Notation	Meaning
m	Index of the storey where $m \in \{-M, \cdots, 0, \cdots, M\}$
Φ_j	Set of BSs on the jth storey
λ	Density of BSs on each storey
h	Height of BSs and users on each storey
H	Height of each storey
P	Transmit power of BSs
α	Path loss exponent of each storey
T	Coverage probability threshold
w	Penetration loss of one ceiling
N	Additive white Gaussian noise power
β_0	Path loss at the reference distance
R_m	Horizontal distance from the typical user to the nearest BS on the mth storey
l_m	Distance from the typical user to the nearest BS on the mth storey
$P_{r,m}$	Average power of the strongest received signal from a BS on the mth storey
B_m	Probability that the typical user is associated to a BS on the mth storey
C_m	Coverage probability when the typical user is served by a BS on the mth storey
A_m	Average ergodic rate when the typical user is served by a BS on the mth storey
$C, Rate$	Coverage probability and average ergodic rate

tractability in the following, we assume that on each storey, $h_{\mathrm{B}} = h_{\mathrm{U}}$. Note that under this assumption, the value of h_{B} and h_{U} has no effect on the coverage probability.

One user can only be associated to one BS. We use $m \in \{-M, -(M-1), \cdots, 0, 1, \cdots, M\}$ as the index of the storey that contains the serving BS for the typical user. Let R_m denote the horizontal distance from the nearest BS on the mth storey to the typical user, and then the distance from the nearest BS on the mth storey to the typical user is given by

$$l_m = \sqrt{(mH)^2 + R_m^2}. \tag{1}$$

The user is associated to the BS providing the strongest downlink received signal. The average power of the strongest received signal from a BS on the mth storey is given by [12][36]

$$P_{r,m} = P\beta_0 l_m^{-\alpha} w^{|m|}, \tag{2}$$

where P is the transmit power of a BS, β_0 is the path loss at the reference distance of 1 m, α is the path loss exponent , $w(0 < w < 1)$ is the penetration loss of one ceiling, and the power of the small scale fading is averaged to be 1.

We denote the probability that the typical user is associated to a BS on the mth storey as B_m, and denote the horizontal distance from the typical user to its serving BS as X_m. The following lemma gives the expression for the probability density function (PDF) of X_m, which will be useful for the derivations of the coverage probability in Section 3. In our system model as defined in Fig. 1, the PDF for the mth storey is the same as that for the $-m$th storey. In the following, we will focus on $0 \leq m \leq M$.

Lemma 1. *The PDF of the distance X_m between a typical user and its serving BS is*

$$f_{X_m}(x) = \begin{cases} f_{X_{m,m}}(x), & 0 < x \leq I_{m,(m+1)}, \\ \cdots \\ f_{X_{m,k}}(x), & I_{m,k} < x \leq I_{m,(k+1)}, \\ \cdots \\ f_{X_{m,M}}(x), & I_{m,M} < x < \infty, \end{cases} \tag{3}$$

where $I_{m,k}$ is formulated as

$$I_{m,k} = \begin{cases} \sqrt{(kH)^2 w^{\frac{2(m-k)}{\alpha}} - (mH)^2}, & m \leq k \leq M \\ \infty, & k = M+1 \end{cases} \tag{4}$$

and $f_{X_{m,k}}(x)$ is

$$f_{X_{m,k}}(x) = \frac{2\pi\lambda}{B_m} x \exp\Big\{ -\pi\lambda(F_m + F_{m,k}) \Big\}, \tag{5}$$

where F_m and $F_{m,k}$ are given in (6), (7).

$$F_m = 2\left(\left(m^2H^2+x^2\right)\frac{w^{-\frac{2}{\alpha}}\left(1-w^{-\frac{2(m-1)}{\alpha}}\right)}{1-w^{-\frac{2}{\alpha}}}-\frac{(m-1)m(2m-1)}{6}H^2\right)+\left(m^2H^2+x^2\right)w^{-\frac{2m}{\alpha}}+2x^2, \tag{6}$$

$$F_{m,k} = 2\left(\left(m^2H^2+x^2\right)\frac{w^{\frac{2}{\alpha}}\left(1-w^{\frac{2(k-m)}{\alpha}}\right)}{1-w^{\frac{2}{\alpha}}}-\frac{k(k+1)(2k+1)-m(m+1)(2m+1)}{6}H^2\right), \tag{7}$$

Proof. See Appendix A. □

3 Coverage Probability

The coverage probability C is the probability that the SINR of the typical user is higher than a target threshold. The typical user can be connected to at most one BS, so the coverage probability is given by

$$C = \sum_{m=-M}^{M} C_m B_m, \tag{8}$$

where B_m is the probability that the typical user associates to a BS on the mth storey, and C_m is the corresponding coverage probability. Since $C_m = C_{-m}$, for clarity, we consider $0 \leq m \leq M$, C will be

$$C = C_0B_0 + 2\sum_{m=1}^{M} C_m B_m. \tag{9}$$

The typical user is in coverage when its SINR from its associated BS is larger than the given threshold T, when the typical user associates to the BS on the mth storey, the coverage probability averaged over the plane is

$$C_m = \mathbb{E}_x\left[\mathbb{P}\left[\mathrm{SINR}_m(x) > T\right]\right], \tag{10}$$

where x is the horizontal distance from the typical user to its serving BS and SINR_m is denoted as

$$\mathrm{SINR}_m = \frac{Pg_{m,0}(m^2H^2+x^2)^{-\frac{\alpha}{2}}w^m}{\sum_{j=-M}^{M}\sum_{i\in\Phi_j\setminus \mathrm{B}_{m0}} Ph_{j,i}|Y_{ji}|^{-\alpha}w^{|j|}+\frac{N}{\beta_0}}, \tag{11}$$

where $g_{m,0}$ is the Raleigh fading with an unit average power, B_{m0} denotes the serving BS, $h_{j,i}$ is the Raleigh fading power gain with unit mean from the interfering BS i on the jth storey, and $|Y_{ji}|$ is the distance between the interfering BS i on the jth storey and the typical user, and N is the additive white Gaussian noise with a constant mean power.

3.1 General Case and Main Result

We first give the general result of the coverage probability and then analyze the special case of $M = 1$.

Theorem 1. *The coverage probability of the typical user associated to the BS on the mth storey C_m can be computed as*

$$C_m = \sum_{k=m}^{M} C_{m,k}, \tag{12}$$

where

$$C_{m,k} = \frac{2\pi\lambda}{B_m}\int_{I_{m,k}}^{I_{m,(k+1)}} x\exp\Big\{-\frac{T}{\mathrm{SNR}_m}-2\pi\lambda\left(m^2H^2+x^2\right)\sum_{n=1}^{M}\mathscr{Q}_{m,n,k}w^{\frac{2}{\alpha}(n-m)} - \pi\lambda\left(F_m+F_{m,k}\right)-\pi\lambda\mathscr{Q}\left(m^2H^2+x^2\right)w^{-\frac{2m}{\alpha}}\Big\}\mathrm{d}x, \tag{13}$$

in (13), $I_{m,k}$, F_m, $F_{m,k}$ are defined in (4), (6), (7), SNR_m is

$$\mathrm{SNR}_m = \frac{Pw^m\beta_0\left(m^2H^2+x^2\right)^{-\frac{\alpha}{2}}}{N}, \tag{14}$$

and

$$\mathscr{Q} = \frac{2T}{\alpha-2}\,{}_2F_1\left[1,1-\frac{2}{\alpha};2-\frac{2}{\alpha};-T\right], \tag{15}$$

$$\mathscr{Q}_{m,n,k}=\begin{cases}\mathscr{Q}, & n\leq k\\ \frac{2TB_{m,n,x}^{2/\alpha-1}}{\alpha-2}{}_2F_1\left[1,1-\frac{2}{\alpha};2-\frac{2}{\alpha};-\frac{T}{B_{m,n,x}}\right], & n>k\end{cases} \tag{16}$$

where $B_{m,n,x}=(nH)^{\alpha}w^{m-n}(m^2H^2+x^2)^{-\frac{\alpha}{2}}$.

Proof. See Appendix B. □

3.2 Special Case: M = 1

Fig.2 shows the coverage probability versus the SINR threshold under the setting of $\lambda=10^{-3}$ BS/m^2 and $H=3$ m, it can be observed that the difference between the coverage probability of the $M=1$ case and $M>1$ cases is negligible. Therefore, the coverage probability of the $M=1$ case can be used to predict that of cases with $M>1$.

Proposition 1. *When M=1, the coverage probability of the typical user is*

$$C^{M=1}=B_0C_0+2B_1C_1, \tag{17}$$

where B_1C_1 *and* B_0C_0 *are*

$$\begin{aligned}B_1C_1&=2\pi\lambda\int_0^{\infty}x\exp\left\{-\frac{T}{\mathrm{SNR}_1}-\pi\lambda\mathscr{Q}\left(H^2+x^2\right)\left(w^{-\frac{2}{\alpha}}+2\right)-\pi\lambda\left(\frac{H^2+x^2}{w^{\frac{2}{\alpha}}}+2x^2\right)\right\}\mathrm{d}x\\&=\frac{\exp\left\{-\frac{T}{\mathrm{SNR}_1}-\pi\lambda H^2\left(\mathscr{Q}w^{-\frac{2}{\alpha}}+2\mathscr{Q}+w^{-\frac{2}{\alpha}}\right)\right\}}{\left(w^{-\frac{2}{\alpha}}+2\right)(\mathscr{Q}+1)},\end{aligned} \tag{18}$$

$$
\begin{aligned}
B_0C_0 =& 2\pi\lambda \int_0^{Hw^{-\frac{1}{\alpha}}} x\exp\left\{-\frac{T}{\mathrm{SNR}_0} - \pi\lambda x^2\left(\mathscr{Q}+2\mathscr{Q}_{0,1}w^{\frac{2}{\alpha}}+1\right)\right\}\mathrm{d}x \\
&+ 2\pi\lambda \int_{Hw^{-\frac{1}{\alpha}}}^{\infty} x\exp\left\{-\frac{T}{\mathrm{SNR}_0} - \pi\lambda x^2\left(\mathscr{Q}+2\mathscr{Q}w^{\frac{2}{\alpha}}+2w^{\frac{2}{\alpha}}-2\frac{H^2}{x^2}+1\right)\right\}\mathrm{d}x \\
=& 2\pi\lambda \int_0^{Hw^{-\frac{1}{\alpha}}} x\exp\left\{-\frac{T}{\mathrm{SNR}_0} - \pi\lambda x^2\left(\mathscr{Q}+2\mathscr{Q}_{0,1}w^{\frac{2}{\alpha}}+1\right)\right\}\mathrm{d}x \\
&+ \frac{\exp\left\{-\frac{T}{\mathrm{SNR}_0} - \pi\lambda H^2\left(\mathscr{Q}w^{-\frac{2}{\alpha}}+2\mathscr{Q}+w^{-\frac{2}{\alpha}}\right)\right\}}{(\mathscr{Q}+1)\left(2w^{\frac{2}{\alpha}}+1\right)},
\end{aligned} \tag{19}
$$

where

$$
\mathscr{Q}_{0,1} = \frac{2TH^{-2}w^{\frac{2}{\alpha}}x^2}{\alpha-2}{}_2F_1\left[1,1-\frac{2}{\alpha};2-\frac{2}{\alpha};-\frac{T}{H^{\alpha}w^{-1}x^{-\alpha}}\right]. \tag{20}
$$

Proof. The expression can be easily obtained by plugging $M=1$ into (9). □

Lemma 2. *For an interference-limited network (where N=0), when $\lambda \to 0$, $C^{M=1} = C^{M=0}$, i.e., the coverage probability for a 3-storey 3D SCN will be identical to that for a single-storey 2D SCN.*

Proof. From (17), it is clear that when $\lambda \to 0$, $B_1C_1 = \frac{1}{\left(w^{-\frac{2}{\alpha}}+2\right)(\mathscr{Q}+1)}$, $B_0C_0 = \frac{1}{\left(2w^{\frac{2}{\alpha}}+1\right)(\mathscr{Q}+1)}$, and thus $C^{M=1} = B_0C_0 + 2B_1C_1 = \frac{1}{\mathscr{Q}+1} = C^{M=0}$. □

Lemma 3. *For an interference-limited network (where N=0), when $H \to 0$ or $H \to \infty$, $C^{M=1} = C^{M=0}$, i.e., the coverage probability for a 3-storey 3D SCN is identical to that for a single-storey 2D SCN.*

Proof. In (17), when $H \to 0$, $B_1C_1 = \frac{1}{\left(w^{-\frac{2}{\alpha}}+2\right)(\mathscr{Q}+1)}$, $B_0C_0 = \frac{1}{\left(2w^{\frac{2}{\alpha}}+1\right)(\mathscr{Q}+1)}$, and thus $C^{M=1} = \frac{1}{\mathscr{Q}+1} = C^{M=0}$. When $H \to \infty$, $B_0C_0 = 2\pi\lambda\int_0^{\infty} x\exp\left\{-\pi\lambda x^2(\mathscr{Q}+1)\right\}\mathrm{d}x = \frac{1}{\mathscr{Q}+1}$, $B_1C_1 = 0$, and thus $C^{M=1} = \frac{1}{\mathscr{Q}+1} = C^{M=0}$. □

4 Spectral Efficiency

The spectral efficiency can be calculated using the average ergodic rate of the typical user as follows

$$Rate = \sum_{m=-M}^{M} A_m B_m, \tag{21}$$

where B_m is the probability that the typical user is associated to the BS on the mth storey. Similar to (9), (21) can be further rewritten as

$$Rate = A_0 B_0 + 2 \sum_{m=1}^{M} A_m B_m, \tag{22}$$

A_m is the average ergodic rate when the typical user connects to the mth storey. A_m can be derived as

$$A_m = \mathbb{E}_{\mathrm{SINR}_m} \left[\log_2 \left(1 + \mathrm{SINR}_m \right) \right], \tag{23}$$

Theorem 2. *The average ergodic rate of the mth storey can be derived as*

$$A_m = \sum_{k=m}^{M} A_{m,k}, \tag{24}$$

where

$$A_{m,k} = \frac{2\pi\lambda}{B_m} \int_0^{\infty} \int_{I_{m,k}}^{I_{m,(k+1)}} x \exp\Big\{ - \frac{2^t - 1}{\mathrm{SNR}_m} - 2\pi\lambda \left(m^2 H^2 + x^2 \right) \sum_{n=1}^{M} \mathscr{Q}_{m,n,k,t} w^{\frac{2}{\alpha}(n-m)} - \pi\lambda \left(F_m + F_{m,k} \right) - \pi\lambda \mathscr{Q}_t \left(m^2 H^2 + x^2 \right) w^{-\frac{2m}{\alpha}} \Big\} \mathrm{d}x \mathrm{d}t, \tag{25}$$

in which

$$\mathscr{Q}_t = \frac{2(2^t - 1)}{\alpha - 2} \, {}_2F_1 \left[1, 1 - \frac{2}{\alpha}; 2 - \frac{2}{\alpha}; 1 - 2^t \right], \tag{26}$$

$$\mathscr{Q}_{m,n,k,t} = \begin{cases} \mathscr{Q}_t, & n \leq k \\ \frac{2(2^t-1)B_{m,n,x}^{2/\alpha-1}}{\alpha-2} {}_2F_1\left[1, 1-\frac{2}{\alpha}; 2-\frac{2}{\alpha}; \frac{1-2^t}{B_{m,n,x}}\right], & n > k \end{cases} \tag{27}$$

where $B_{m,n,x} = (nH)^{\alpha} w^{-n} (m^2H^2 + x^2)^{-\frac{\alpha}{2}}$.

Proof. See Appendix C. □

The area spectral efficiency in bps/Hz/m^2 can be computed as [34]

$$Rate^{\text{ASE}} = \lambda Rate, \tag{28}$$

where λ is the density of the BSs in BSs/m^2 and $Rate$ is given in (21).

Table 2 Values of Parameters

Parameter	Default Value
Path loss at reference distance β_0	-38.5 dB
AWGN average power N	-104 dBm
Coverage probability threshold T	0 dB
Transmit power of BSs P	33 dBm
Path loss exponent α	4
Height of BSs and users h	1.2 m
Storey height H	3 m
BS density on each storey λ	10^{-2} BS/m^2
Ceiling penetration loss w	-10 dB

5 Numerical Results

In this section, we evaluate the accuracy of our analytical expressions and further analyze the performance of our multi-storey SCN model.

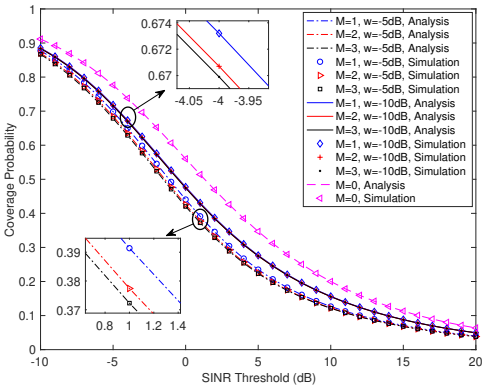

(a) For different values of w and $\alpha = 4$.

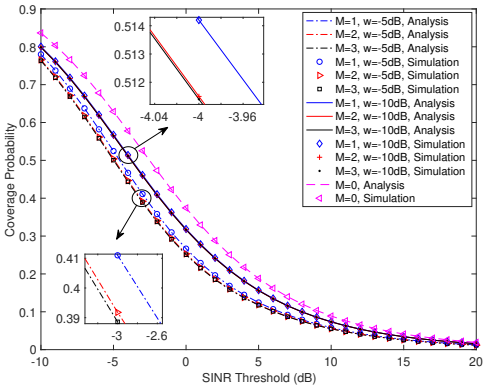

(b) For different values of w and $\alpha = 3$.

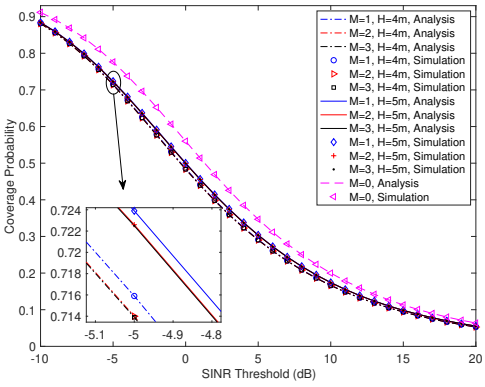

(c) For different values of H.

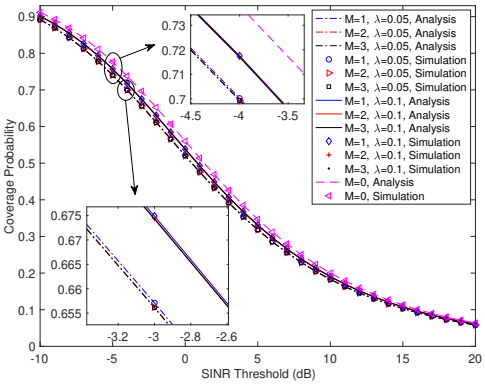

(d) For different values of λ (BS/m^2).

Fig. 2 Coverage probability vs. the SINR threshold for $M = 0, 1, 2$ and 3.

5.1 Validation of the Analytical Results

For numerical evaluation and simulations, the default values of parameters are listed in Table 2 [20] unless otherwise stated. We set $\alpha = 4$ as most indoor transmission links are in NLOS conditions. As shown in Table 3 of [36], the penetration loss of one ceiling ranges from -4 dB to -22 dB, depending on the carrier frequencies (0.9-5.8 GHz) and building environments. We set the default ceiling penetration loss as -10 dB. We verify the analytical results through 10^5 Monte Carlo simulations for a building with a floor area of 60m$\times$60m.

In Fig. 2, we compare the coverage probability of the proposed SCN model for $M = 0, 1, 2$ and 3. The analytic curves match well with those simulated by Monte Carlo methods, which demonstrates the accuracy of our mathematical derivations. In Fig. 2(a)-(d), we can observe that

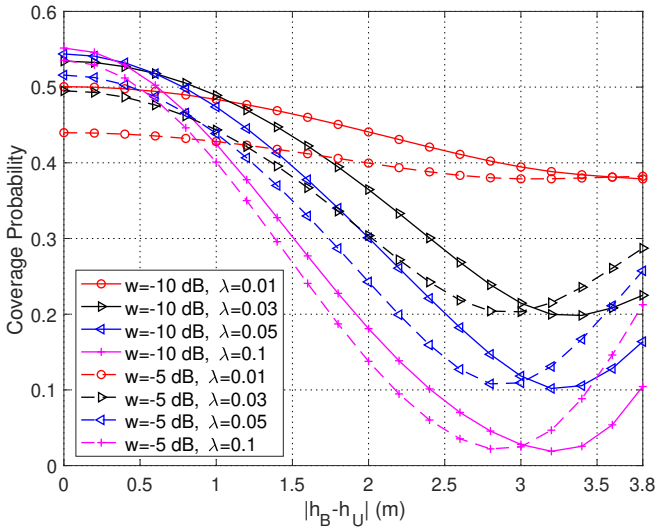

Fig. 3 Coverage probability vs. the absolute value of the height difference between BSs and UEs for different values of w and λ (BS/m^2).

the $M = 0$ case provides the upper bound of the coverage probability where the BS deployment follows the traditional 2D PPP distribution [18]. From Fig. 2(a) and Fig. 2(b), it is obvious that when $w = -5$ dB, the coverage probability of the $M = 0$ case is much higher than that of the $M \geq 1$ cases. However, the performance of the $M = 1$ case is close to $M = 2$ and $M = 3$ cases, the gap between them is up to 0.02 and thus negligible. Additionally, when $w = -10$ dB, the $M = 1$ case shows nearly the same coverage probability as the $M = 2$ and $M = 3$ cases. Similar phenomenon can be observed in Fig. 2(c) and Fig. 2(d), where different values of H and λ are included in the comparison.

Based on the results in Fig. 2, it is reasonable to approximate the proposed multi-storey SCN model for M = 2, 3 using the $M = 1$ case, the expressions of which can be found in Proposition 1. Accordingly, we will adopt the analytical results of the $M = 1$ case in the discussions hereafter.

In Fig. 3, we evaluate the impact of the absolute value of the height difference between BSs and UEs on the coverage probability for various values of the ceiling penetration loss and the BS density on each storey through Monte Carlo simulations. We fix the UE height as 1.2 m and set the maximum BS height as 5 m following a practical upper bound of storey height [38]. We can see that the maximum coverage probability is achieved when the BS height is the

same as the UE height. Therefore, in the following, we assume that the BS height and the UE height are identical to evaluate the optimal achievable network performance of our proposed multi-storey SCN model.

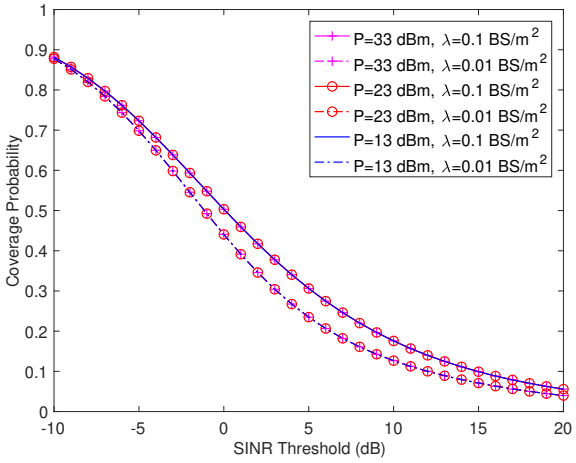

(a) $w = -5$ dB, $H = 3$ m.

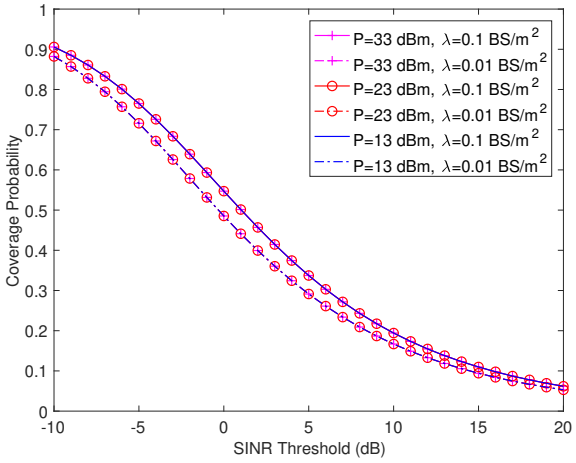

(b) $w = -10$ dB, $H = 4$ m.

Fig. 4 Coverage probability vs. the SINR threshold for different values of P and λ.

In Fig. 4, we plot the coverage probability versus the SINR threshold for different values of the BS transmit power, BS density on each storey, ceiling penetration loss, and height of each storey. We can see that the coverage probability does not change with the BS transmit power, for given BS density on each storey, ceiling penetration loss and height of each storey.

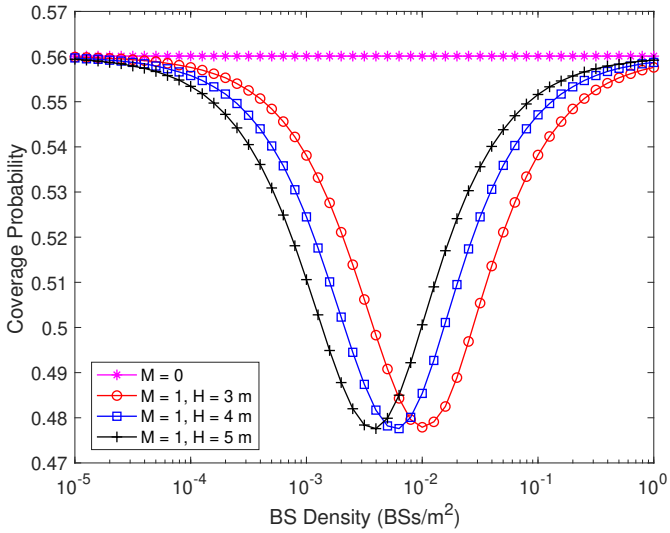

Fig. 5 The coverage probability vs. the BS density.

This is mainly due to the relatively high indoor BS density that leads to an interference-limited multi-storey SCN.

5.2 Effect of the BS density

To better demonstrate the performance of the multi-storey SCN, we ignore the thermal noise and set w as -10 dB. It is well-known that the BS density does not affect the network coverage probability in interference-limited networks and the area spectral efficiency scales linearly with the network densification [18]. This is because the increased interference can be compensated by the shrinked distance between the typical UE and the connected BS.

However, we observe a different scaling law in our proposed multi-storey SCN model. In Fig. 5, we analyze the influence of the BS density per storey to the coverage probability for $H = 3$ m, $H = 4$ m, $H = 5$ m [38, 39], respectively. Note that the $M = 0$ curve stands for the 2D scenario [18] and its coverage probability $C^{M=0}$ remains unchanged with the increase of the BS density. When $M = 1$, the coverage probability first decreases from $C^{M=0}$ and then increases back to $C^{M=0}$ with the network densification. This phenomenon is referred to as the *Coverage Probability Valley* hereafter. Intuitively, when λ approaches infinity, the typical UE will hardly associate with any storey other than the 0th storey, and thus the coverage probability

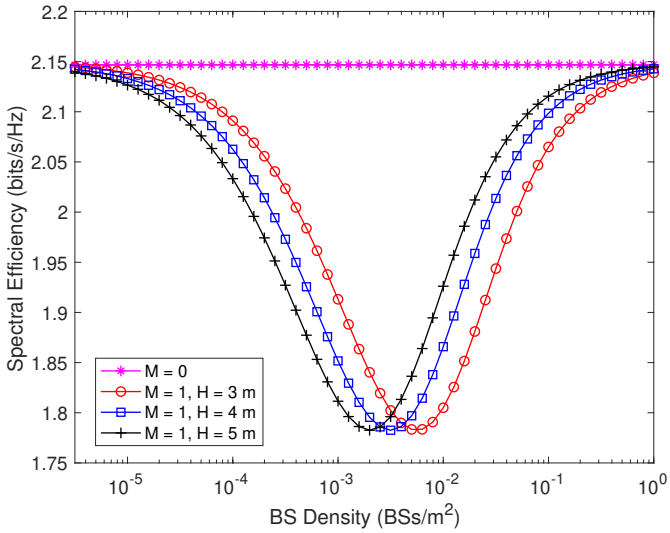

Fig. 6 The spectral efficiency vs. the BS density.

of the $M > 1$ cases is close to that of the $M = 0$ case. Moreover, the coverage probability as $\lambda \to 0$ is in accordance with Lemma 2. The minimum value of coverage probability and the corresponding BS density per storey λ^* can be obtained when $C^{M=1'}(\lambda^*) = 0$. The solution can be numerically found using Newton's method, and details are given in Appendix D. The numerical results are 10.476×10^{-3} BS/m^2, 5.9×10^{-3} BS/m^2, 3.8×10^{-3} BS/m^2 for $H = 3$ m, $H = 4$ m, $H = 5$ m, respectively, and the minimum coverage probability is 0.4775. The results reveal that the worst BS densities suffer from more than 8 percent loss of coverage probability compared with the 2D model. Since the spectral efficiency is the integral of the coverage probability, a *SE Valley* can also be found in Fig. 6, where the worst BS densities can be similarly obtained with Newton's method. The numerical results are 5.6×10^{-3} BSs/m^2, 3.1×10^{-3} BSs/m^2, 2×10^{-3} BSs/m^2 for $H = 3$ m, $H = 4$ m, $H = 5$ m, respectively, and the minimum spectral efficiency is 1.7826 bps/Hz/m^2. To alleviate the performance loss, it is necessary to avoid the Valley area in the practical deployment of BSs.

In Fig. 7, we show the area spectral efficiency of $M = 0$ and $M = 1$ cases. For the $M = 0$ scenario, the ASE increases linearly with network densification. Nevertheless, for the multi-storey case, the ASE first increases linearly when the BS density per storey is low and then exhibits a slowing-down in the ASE growth when the network becomes denser. When the

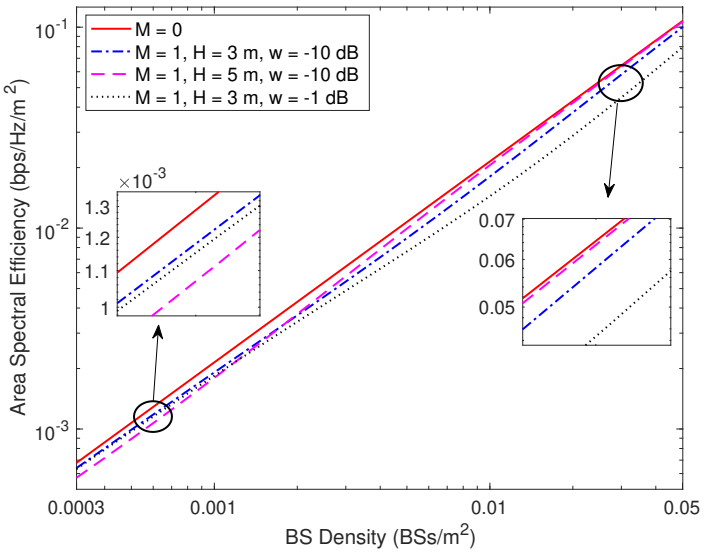

Fig. 7 The area spectral efficiency vs. the BS density.

network is ultra dense, the ASE returns to the linear growth again. Such a trend of the ASE performance is not difficult to explain according to the SE trend in Fig. 6. Moreover, we observe that for a given storey height, a higher penetration loss of the ceiling leads to a higher ASE.

5.3 Effect of the storey height

In Fig. 8, we assume that the penetration loss of the ceiling $w = -5$ dB, and the threshold of the coverage probability is 0 dB. We assume that the BS height and UE height are both 1.2 m, so the minimum storey height is 1.2 m. We plot the 3D figure to show the influence of the storey height with different BS densities, where a conspicuous *Coverage Probability Valley* can be observed. For most of the BS densities, the coverage probability of the typical UE first decreases and then increases with the increasing storey height. The red bold line shows the locations of the storey height H^* corresponding to the lowest coverage probability, which can be obtained by solving $C^{M=1'}(H^*) = 0$ and numerically found using a standard bisection searching [40]. Due to the existing of the *Coverage Probability Valley*, there is a worst storey height that leads to the lowest coverage probability. The worst storey height is affected by the

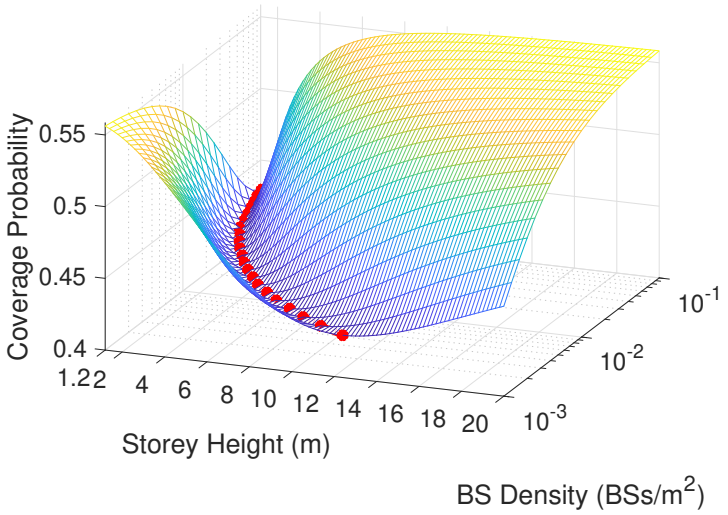

Fig. 8 Coverage probability vs. the storey height H and BS density for $w = -5$ dB. The red bold line shows the storey height and BS density corresponding to the lowest coverage probability.

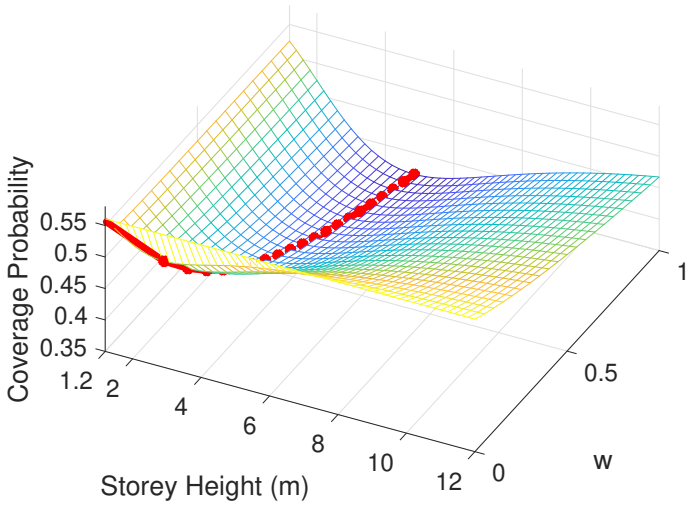

Fig. 9 Coverage probability vs. the storey height H and the ceiling penetration loss w. The red bold line shows the storey height and ceiling penetration loss corresponding to the lowest coverage probability.

BS density, as can be seen, when the BS density increases, the worst storey height decreases. It is worth noting that the coverage probability monotonously increases when the worst storey height is less than 1.2 m.

In Fig. 9, the BS density per storey is set to be 10^{-2} BS/m^2 and the threshold of the coverage probability is 0 dB. A similar *Coverage Probability Valley* can be observed. The coverage probability of the typical UE first decreases and then increases with the increasing storey height for a particular penetration loss of the ceiling. The red bold line also indicates the locations of the storey height H^* with lowest coverage probability. Note that a smaller value of w means a higher penetration loss of the ceiling, which indicates that the storey height corresponding to the lowest coverage probability is smaller when the penetration loss becomes higher.

In conclusion, the *Coverage Probability Valley* exists for any BS density and penetration loss of the ceiling, which is in accordance with the conclusion in Lemma 3. Intuitively, when the storey height is 0, all the BSs are on the same storey, that is the 2D BS deployment. When the storey height becomes large enough, the probability of the typical UE being connected to any storey other than the 0th storey is close to 0 and the coverage probability of the $M > 1$ cases is close to that of the 2D model. For the commercial success of future 5G networks, it is crucial to avoid the *Coverage Probability Valley* in the design of new buildings. Actually, with our tractable expressions, it is convenient to find the optimal storey height. With the acceptable range of storey height, e.g. $H_1 \leq H \leq H_2$, the maximum coverage probability can be obtained at either H_1 or H_2 due to the *Coverage Probability Valley*. Therefore, we only need to compute the coverage probability at H_1 and H_2 respectively and choose the higher one.

5.4 Effect of the penetration loss of the ceiling

In Fig. 10 and Fig. 11, we analyze the influence of the penetration loss of the ceiling (in linear scale). Larger w means smaller penetration loss. It is observed that the coverage probability and spectral efficiency increase with stronger penetration loss, which indicates that the cross-storey communication is harmful to the network performance when the BSs and UEs share the same height. When $w = 0$, the typical UE only connects to the BSs on the 0th storey, so the network performance is the same with the 2D model. According to this conclusion, we should choose the materials with higher penetration loss for the ceilings of a new building.

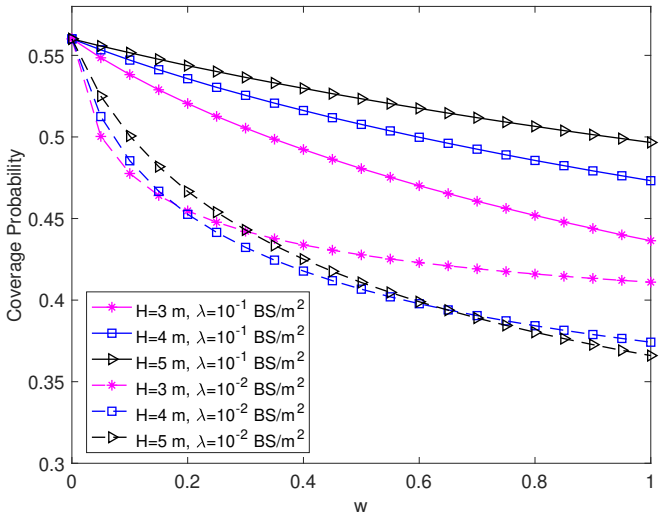

Fig. 10 The coverage probability vs. the ceiling penetration loss w.

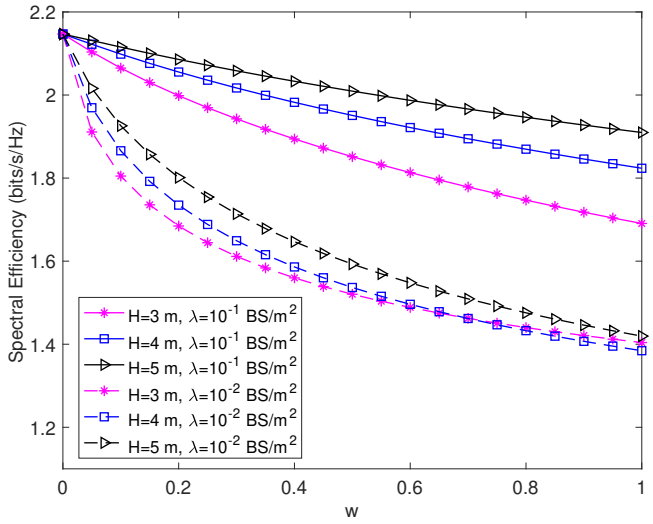

Fig. 11 The spectral efficiency vs. the ceiling penetration loss w.

6 Conclusions

In this paper, we have proposed a new 3D stochastic geometry model for the small-cell networks in the multi-storey built environment. A novel theoretical discovery has been presented, i.e., the *Coverage Probability Valley*. The coverage probability first decreases and then increases with the increase of the storey height and the network density. Moreover, we show that a ceilings

with a higher penetration loss can provide a better network performance. The contributions of this paper can shed insight on the design of new buildings and future indoor SCN deployments.

In the future, we will further consider a more practical indoor built environment with walls and stochastic blockages. In addition, interference management techniques such as dynamic power control, BS sleeping strategy, and directional antennas will be investigated.

Appendix A

Denote n as the index of the storey that the typical user connected to. Given the condition that the typical user is associated to the BS on the mth storey, $X_m > x$ is equal to $R_m > x$, the probability of $X_m > x$ can be computed as

$$\mathbb{P}[X_m > x] = \mathbb{P}[R_m > x | n = m] = \frac{\mathbb{P}[R_m > x, n = m]}{\mathbb{P}[n = m]}, \tag{29}$$

where

$$\mathbb{P}[n = m] = B_m = \mathbb{E}_{R_m}\left[\mathbb{P}\left[P_{r,m}(R_m) > \max_{j, j\neq m} P_{r,j}\right]\right], \tag{30}$$

the joint probability of $R_m > x$ and $n = m$ is

$$\begin{aligned}
&\mathbb{P}[R_m > x, n = m] \\
&= \mathbb{P}\left[R_m > x, P_{r,m}(R_m) > \max_{j, j\neq m} P_{r,j}\right] \\
&= \int_x^{\infty} \prod_{j=-M, j\neq m}^{M} \mathbb{P}\left[P_{r,m}(r) > P_{r,j}\right] f_{R_m}(r) \mathrm{d}r,
\end{aligned} \tag{31}$$

from (2), we have

$$\begin{aligned}
&\mathbb{P}\left[P_{r,m}(r) > P_{r,j}\right] \\
&= \mathbb{P}\left[\left(m^2H^2 + r^2\right)^{-\frac{\alpha}{2}} w^m > \left(j^2H^2 + R_j^2\right)^{-\frac{\alpha}{2}} w^{|j|}\right] \\
&= \mathbb{P}\left[R_j^2 > \left(m^2H^2 + r^2\right) w^{\frac{2(|j|-m)}{\alpha}} - j^2H^2\right],
\end{aligned} \tag{32}$$

when $|j| \leq m$, $\left((m^2H^2+r^2)w^{\frac{2(|j|-m)}{\alpha}} - j^2H^2\right)$ is non-negative, while when $|j| > m$, it could be a negative number. So $\mathbb{P}\left[P_{r,m}(r) > P_{r,j}\right]$ can be divided into two parts as

$$\mathbb{P}\left[P_{r,m}(r) > P_{r,j}\right] = \begin{cases} \mathbb{P}\left[P_{r,m}(r) > P_{r,j}\right], & |j| \leq m \\ \quad\quad |j|\leq m & \\ \mathbb{P}\left[P_{r,m}(r) > P_{r,j}\right], & |j| > m \\ \quad\quad |j|>m & \end{cases} \tag{33}$$

since R_j^2 is always non-negative, so in the case of $|j| > m$, when $(m^2H^2+r^2)w^{\frac{2(|j|-m)}{\alpha}} < j^2H^2$, $\mathbb{P}\left[P_{r,m}(r) > P_{r,j}\right]$ is 1. With these analysis, (33) can be further derived as (34), (35).

$$\begin{aligned} &\mathbb{P}\left[P_{r,m}(r) > P_{r,j}\right] \\ &\quad\quad |j|\leq m \\ &= \mathbb{P}\left[R_j > \sqrt{(m^2H^2+r^2)w^{\frac{2(|j|-m)}{\alpha}} - j^2H^2}\right] \\ &\overset{(a)}{=} \mathbb{P}\left[\text{No BS closer than } \sqrt{(m^2H^2+r^2)w^{\frac{2(|j|-m)}{\alpha}} - j^2H^2}\right] \\ &= \exp\Big\{-\pi\lambda\ \left((m^2H^2+r^2)w^{\frac{2(|j|-m)}{\alpha}} - j^2H^2\right)\Big\}, \end{aligned} \tag{34}$$

in (34), (a) can be derived from the null probability of a 2D Poisson point process in an area A is $\exp(-\lambda A)$ [18].

$$\begin{aligned} &\mathbb{P}\left[P_{r,m}(r) > P_{r,j}\right] \\ &\quad\quad |j|>m \\ &= \begin{cases} 1, & r < \sqrt{j^2H^2w^{\frac{2(m-|j|)}{\alpha}} - m^2H^2} \\ \mathbb{P}\left[R_j > \sqrt{(m^2H^2+r^2)w^{\frac{2(|j|-m)}{\alpha}} - j^2H^2}\right], & r \geq \sqrt{j^2H^2w^{\frac{2(m-|j|)}{\alpha}} - m^2H^2} \end{cases} \\ &= \begin{cases} 1, & r < \sqrt{j^2H^2w^{\frac{2(m-|j|)}{\alpha}} - m^2H^2} \\ \exp\Big\{-\pi\lambda\ \left((m^2H^2+r^2)w^{\frac{2(|j|-m)}{\alpha}} - j^2H^2\right)\Big\}, & r \geq \sqrt{j^2H^2w^{\frac{2(m-|j|)}{\alpha}} - m^2H^2} \end{cases} \end{aligned} \tag{35}$$

$f_{R_m}(r)$ is given from

$$f_{R_m}(r) = \frac{\mathrm{d}(1-\mathbb{P}[R_m > r])}{\mathrm{d}r} = e^{-\pi\lambda r^2}2\pi\lambda r. \tag{36}$$

Since $\mathbb{P}[X_m > x]$ is the CCDF of X_m, the PDF of X_m is

$$\begin{aligned} f_{X_m}(x) &= \frac{\mathrm{d}(1-\mathbb{P}[X_m > x])}{\mathrm{d}x} \\ &= \frac{1}{B_m} \prod_{j=-M, j\neq m}^{M} \mathbb{P}\left[P_{r,m}(x) > P_{r,j}\right] f_{R_m}(x), \end{aligned} \tag{37}$$

Combining (34), (35), (36), (37), we can obtain

$$\begin{aligned} f_{X_m}(x) &= \frac{2\pi\lambda}{B_m} x \exp\Big\{-\pi\lambda x^2\Big\} \prod_{-m\leq j<m} \mathbb{P}\left[P_{r,m}(x) > P_{r,j}\right] \prod_{\substack{m<|j|\leq M \\ |j|>m}} \mathbb{P}\left[P_{r,m}(x) > P_{r,j}\right] \\ &\overset{(a)}{=} \frac{2\pi\lambda}{B_m} x \exp\Big\{-\pi\lambda F_m\Big\} \prod_{\substack{m<|j|\leq M \\ |j|>m}} \mathbb{P}\left[P_{r,m}(x) > P_{r,j}\right] \\ &\overset{(b)}{=} \begin{cases} \frac{2\pi\lambda}{B_m} x \exp\Big\{-\pi\lambda\left(F_m + F_{m,m}\right)\Big\}, & 0 < x \leq I_{m,(m+1)} \\ \cdots \\ \frac{2\pi\lambda}{B_m} x \exp\Big\{-\pi\lambda\left(F_m + F_{m,k}\right)\Big\}, & I_{m,k} < x \leq I_{m,(k+1)} \\ \cdots \\ \frac{2\pi\lambda}{B_m} x \exp\Big\{-\pi\lambda\left(F_m + F_{m,M}\right)\Big\}, & I_{m,M} < x < \infty \end{cases} \end{aligned} \tag{38}$$

where (a), (b) can be computed using the sum of a geometric series, $I_{m,k}$, F_m, $F_{m,k}$ are defined in (4), (6), (7), which concludes our proof.

Appendix B

From (10), when the typical user is associated to the BS on the mth storey, the coverage probability is

$$C_m = \int_{x=0}^{\infty} \mathbb{P}\left[\mathrm{SINR}_m(x) > T\right] f_{X_m}(x)\mathrm{d}x, \tag{39}$$

where $f_{X_m}(x)$ is given in (38). Rewrite the $\mathrm{SINR}_m(x)$ as $\gamma_m(x) = \frac{g_{m,0}}{P^{-1}(m^2H^2+x^2)^{\frac{\alpha}{2}} w^{-m} Q}$, where $Q = \sum_{j=-M}^{M} I_j + N/\beta_0$. Then $\mathbb{P}[\mathrm{SINR}_m(x) > T]$ can be derived as

$$\begin{aligned}
&\mathbb{P}[\mathrm{SINR}_m(x) > T] \\
&= \mathbb{P}\left[g_{m,0} > P^{-1}\left(m^2H^2+x^2\right)^{\frac{\alpha}{2}} w^{-m} TQ\right] \\
&= \int_0^{\infty} \exp\left\{-P^{-1}\left(m^2H^2+x^2\right)^{\frac{\alpha}{2}} w^{-m} TQ\right\} f_Q(q)\mathrm{d}q \\
&= \mathbb{E}_Q\left[\exp\left\{-P^{-1}\left(m^2H^2+x^2\right)^{\frac{\alpha}{2}} w^{-m} TQ\right\}\right] \\
&= \exp\left\{-\frac{T}{\mathrm{SNR}_m}\right\} \prod_{j=-M}^{M} \mathscr{L}_{I_j}\left(P^{-1}\left(m^2H^2+x^2\right)^{\frac{\alpha}{2}} w^{-m} T\right),
\end{aligned} \tag{40}$$

where SNR_m is given in (14), define $l_{m,x} = \sqrt{m^2H^2+x^2}$, $l_{j,y} = \sqrt{j^2H^2+y^2}$,the Laplace transform of I_j is

$$\begin{aligned}
&\mathscr{L}_{I_j}\left(P^{-1} l_{m,x}^{\alpha} w^{-m} T\right) \\
&= \mathbb{E}_{I_j}\left[\exp\left\{-P^{-1} l_{m,x}^{\alpha} w^{-m} T I_j\right\}\right] \\
&= \mathbb{E}_{\Phi_j}\left[\exp\left\{-l_{m,x}^{\alpha} T \sum_{i\in\Phi_j} h_{j,i} l_{j,y}^{-\alpha} w^{|j|-m}\right\}\right] \\
&\overset{(a)}{=} \exp\left\{-2\pi\lambda \int_{z_j}^{\infty} \left(1 - \mathscr{L}_{h_j}\left(l_{m,x}^{\alpha} T l_{j,y}^{-\alpha} w^{|j|-m}\right)\right) y\mathrm{d}y\right\} \\
&\overset{(b)}{=} \exp\left\{-2\pi\lambda \int_{z_j}^{\infty} \left(1 - \frac{1}{1+l_{m,x}^{\alpha} T l_{j,y}^{-\alpha} w^{|j|-m}}\right) y\mathrm{d}y\right\} \\
&= \exp\left\{-2\pi\lambda \int_{z_j}^{\infty} \frac{y}{1+l_{m,x}^{-\alpha} T^{-1} w^{m-|j|} l_{j,y}^{\alpha}} \mathrm{d}y\right\},
\end{aligned} \tag{41}$$

where (a) comes from the probability generating functional (PGFL) of PPP [33], and (b) is because $h_j \sim \exp(1)$. z_j is the horizontal distance of the closest interfering BS on the jth storey, similar with (33), it is derived as

$$z_j = \begin{cases} \underset{|j|\le m}{z_j}, & |j| \le m \\ \underset{|j|>m}{z_j}, & |j| > m \end{cases} \tag{42}$$

where

$$\underset{|j|\leq m}{z_j} = \sqrt{(m^2H^2+x^2)w^{\frac{2(|j|-m)}{\alpha}} - j^2H^2}, \tag{43}$$

$$\underset{|j|>m}{z_j} = \begin{cases} 0, & x < I_{m,|j|} \\ \sqrt{(m^2H^2+x^2)w^{\frac{2(|j|-m)}{\alpha}} - j^2H^2}, & x \geq I_{m,|j|} \end{cases} \tag{44}$$

where $I_{m,|j|}$ can be computed using (4). Then $\mathscr{L}_{I_j}\left(P^{-1}l_{m,x}^{\alpha}w^{-m}T\right)$ can be derived as

$$\mathscr{L}_{I_j}\left(P^{-1}l_{m,x}^{\alpha}w^{-m}T\right) = \begin{cases} \underset{|j|\leq m}{\mathscr{L}_{I_j}\left(P^{-1}l_{m,x}^{\alpha}w^{-m}T\right)}, & |j| \leq m \\ \underset{|j|>m}{\mathscr{L}_{I_j}\left(P^{-1}l_{m,x}^{\alpha}w^{-m}T\right)}, & |j| > m \end{cases} \tag{45}$$

employ a change of variable $u = \left(l_{j,y}^{-\alpha}l_{m,x}^{\alpha}Tw^{|j|-m}\right)^{-2/\alpha}$, we can obtain

$$\underset{|j|\leq m}{\mathscr{L}_{I_j}\left(P^{-1}l_{m,x}^{\alpha}w^{-m}T\right)} = \exp\left\{-\pi\lambda\mathscr{Q}l_{m,x}^{2}w^{\frac{2(|j|-m)}{\alpha}}\right\}, \tag{46}$$

where

$$\begin{aligned} \mathscr{Q} &= T^{\frac{2}{\alpha}}\int_{T^{-\frac{2}{\alpha}}}^{\infty}\frac{1}{1+u^{\frac{\alpha}{2}}}\mathrm{d}u \\ &= \frac{2T}{\alpha-2}\,{}_2F_1\left[1,1-\frac{2}{\alpha};2-\frac{2}{\alpha};-T\right] for\ \alpha > 2 \end{aligned} \tag{47}$$

here ${}_2F_1[\cdot]$ denotes the Gauss hypergeometric function. For $|j| > m$,

$$\begin{aligned} &\underset{|j|>m}{\mathscr{L}_{I_j}\left(P^{-1}l_{m,x}^{\alpha}w^{-m}T\right)} \\ &= \begin{cases} \exp\left\{-\pi\lambda\mathscr{Q}_{m,|j|}l_{m,x}^{2}w^{\frac{2(|j|-m)}{\alpha}}\right\}, & x < I_{m,|j|} \\ \exp\left\{-\pi\lambda\mathscr{Q}l_{m,x}^{2}w^{\frac{2(|j|-m)}{\alpha}}\right\}, & x \geq I_{m,|j|} \end{cases} \end{aligned} \tag{48}$$

where

$$\begin{aligned}\mathscr{Q}_{m,|j|} &= T^{\frac{2}{\alpha}} \int_{\frac{(|j|H)^2}{w^{\frac{2(|j|-m)}{\alpha}}(m^2H^2+x^2)T^{\frac{2}{\alpha}}}}^{\infty} \frac{1}{1+u^{\frac{\alpha}{2}}} \mathrm{d}u, \\ &= \frac{2TB_{m,|j|,x}^{2/\alpha-1}}{\alpha-2} {}_2F_1\left[1, 1-\frac{2}{\alpha}; 2-\frac{2}{\alpha}; -\frac{T}{B_{m,|j|,x}}\right], \end{aligned} \tag{49}$$

where $B_{m,|j|,x} = (|j|H)^{\alpha} w^{m-|j|} (m^2H^2+x^2)^{-\frac{\alpha}{2}}$. Plug (46), (48) into (40), we have

$$\begin{aligned}&\mathbb{P}\left[\mathrm{SINR}_m(x) > T\right] \\ &= \exp\left\{-\frac{T}{\mathrm{SNR}_m}\right\} \prod_{|j|\le m} \mathscr{L}_{I_j}\left(P^{-1} l_{m,x}^{\alpha} w^{-m} T\right) \prod_{m<|j|\le M} \mathscr{L}_{I_j}\left(P^{-1} l_{m,x}^{\alpha} w^{-m} T\right) \\ &= \exp\left\{-\frac{T}{\mathrm{SNR}_m}\right\} \exp\left\{\sum_{j=-m}^{m} -\pi\lambda\mathscr{Q} l_{m,x}^2 w^{\frac{2(|j|-m)}{\alpha}}\right\} \prod_{m<|j|\le M} \mathscr{L}_{I_j}\left(P^{-1} l_{m,x}^{\alpha} w^{-m} T\right) \\ &= \begin{cases} \exp\left\{-\frac{T}{\mathrm{SNR}_m} - \pi\lambda\mathscr{Q}\left(m^2H^2+x^2\right) w^{-\frac{2m}{\alpha}} - 2\pi\lambda\left(m^2H^2+x^2\right) D_{m,m}\right\}, & 0 < x \le I_{m,(m+1)} \\ \cdots \\ \exp\left\{-\frac{T}{\mathrm{SNR}_m} - \pi\lambda\mathscr{Q}\left(m^2H^2+x^2\right) w^{-\frac{2m}{\alpha}} - 2\pi\lambda\left(m^2H^2+x^2\right) D_{m,k}\right\}, & I_{m,k} < x \le I_{m,(k+1)} \\ \cdots \\ \exp\left\{-\frac{T}{\mathrm{SNR}_m} - \pi\lambda\mathscr{Q}\left(m^2H^2+x^2\right) w^{-\frac{2m}{\alpha}} - 2\pi\lambda\left(m^2H^2+x^2\right) D_{m,M}\right\}, & I_{m,M} < x < \infty \end{cases} \end{aligned} \tag{50}$$

in which $D_{m,k} = \sum_{n=1}^{M} \mathscr{Q}_{m,n,k} w^{\frac{2}{\alpha}(n-m)}$, $\mathscr{Q}_{m,n,k}$ is given in (16). Combining (38), (39), (50), we can get the coverage probability for the mth storey in (12).

Appendix C

From (23), the average ergodic rate of the typical user when it is associated to the BS on the mth storey is

$$A_m = \int_0^{\infty} \mathbb{E}_{\mathrm{SINR}_m}\left[\log_2\left(1+\mathrm{SINR}_{\mathrm{m}}(x)\right)\right] f_{X_m}(x) \mathrm{d}x, \tag{51}$$

where $f_{X_m}(x)$ can be found in Lemma 1. For a positive random variable X, $\mathbb{E}[X] = \int_0^\infty \mathbb{P}[X > x]\,\mathrm{d}x$, define $l_{m,x} = \sqrt{m^2H^2 + x^2}$,we obtain

$$\begin{aligned}
&\mathbb{E}_{\mathrm{SINR}_m}\left[\log_2\left(1+\mathrm{SINR_m}(x)\right)\right] \\
&= \int_0^\infty \mathbb{P}\left[\log_2\left(1+\mathrm{SINR_m}(x)\right) > t\right]\mathrm{d}t \\
&\overset{(a)}{=} \int_0^\infty \mathbb{P}\left[g_{m,0} > P^{-1} l_{m,x}^{\alpha} w^{-m}(2^t-1)Q\right]\mathrm{d}t \\
&= \int_0^\infty e^{-\frac{2^t-1}{\mathrm{SNR}_m}} \prod_{j=-M}^{M} \mathscr{L}_{I_j}\left(P^{-1} l_{m,x}^{\alpha} w^{-m}(2^t-1)\right)\mathrm{d}t,
\end{aligned} \tag{52}$$

where (a) comes from employ $T = 2^t - 1$ in (40). Following the derivation in (50), (52) can be further derived as

$$\mathbb{E}_{\mathrm{SINR}_m}\left[\log_2\left(1+\mathrm{SINR_m}(x)\right)\right] =$$

$$\begin{cases}
\int_0^\infty \exp\left\{-\frac{2^t-1}{\mathrm{SNR}_m} - \pi\lambda\mathscr{Q}_t\left(m^2H^2+x^2\right)w^{\frac{-2m}{\alpha}} - 2\pi\lambda\left(m^2H^2+x^2\right)D_{m,m,t}\right\}\mathrm{d}t, & 0 < x \le I_{m,(m+1)} \\
\cdots \\
\int_0^\infty \exp\left\{-\frac{2^t-1}{\mathrm{SNR}_m} - \pi\lambda\mathscr{Q}_t\left(m^2H^2+x^2\right)w^{\frac{-2m}{\alpha}} - 2\pi\lambda\left(m^2H^2+x^2\right)D_{m,k,t}\right\}\mathrm{d}t, & I_{m,k} < x \le I_{m,(k+1)} \\
\cdots \\
\int_0^\infty \exp\left\{-\frac{2^t-1}{\mathrm{SNR}_m} - \pi\lambda\mathscr{Q}_t\left(m^2H^2+x^2\right)w^{\frac{-2m}{\alpha}} - 2\pi\lambda\left(m^2H^2+x^2\right)D_{m,M,t}\right\}\mathrm{d}t, & I_{m,M} < x < \infty
\end{cases} \tag{53}$$

in which

$$\begin{aligned}
\mathscr{Q}_t &= (2^t-1)^{\frac{2}{\alpha}} \int_{(2^t-1)^{-\frac{2}{\alpha}}}^\infty \frac{1}{1+u^{\frac{\alpha}{2}}}\mathrm{d}u \\
&= \frac{2(2^t-1)}{\alpha-2}\,{}_2F_1\left[1, 1-\frac{2}{\alpha}; 2-\frac{2}{\alpha}; 1-2^t\right],
\end{aligned} \tag{54}$$

and $D_{m,k,t} = \sum_{n=1}^{M} \mathscr{Q}_{m,n,k,t} w^{\frac{2}{\alpha}(n-m)}$, $\mathscr{Q}_{m,n,k,t}$ is given in (27). Plug (53) into (51), we can get the expression in (22).

Appendix D

To obtain the minimum value of coverage probability and the corresponding BS density per storey in (17), we employ the Newton's method. Assume that λ is the only variable, the coverage probability is

$$C^{M=1}(\lambda) = B_0C_0 + 2B_1C_1, \tag{55}$$

where B_0C_0 and B_1C_1 can be found in (18), (19). Take the first-order derivation of $C^{M=1}(\lambda)$ and we have

$$\begin{aligned} C^{M=1'}(\lambda) &= \frac{-\pi\mathscr{P}H^2}{1+\mathscr{Q}}\exp\left\{-\pi\lambda\mathscr{P}H^2\right\} \\ &+ \int_0^{Hw^{-\frac{1}{\alpha}}} 2\pi x\left(1-\pi\lambda Kx^2\right)\exp\left\{-\pi\lambda Kx^2\right\}, \end{aligned} \tag{56}$$

where $\mathscr{P} = \mathscr{Q}\left(2+w^{-\frac{2}{\alpha}}\right)+w^{-\frac{2}{\alpha}}$, $K = 1+\mathscr{Q}+2\mathscr{Q}_{0,1}w^{\frac{2}{\alpha}}$, $\mathscr{Q}$ and $\mathscr{Q}_{0,1}$ are defined in (15) and (20). Then take the second-order derivation of $C^{M=1}(\lambda)$ and we have

$$\begin{aligned} C^{M=1''}(\lambda) &= \frac{\pi^2\mathscr{P}^2H^4}{1+\mathscr{Q}}\exp\left\{-\pi\lambda\mathscr{P}H^2\right\} \\ &+ \int_0^{Hw^{-\frac{1}{\alpha}}} \left(2\lambda K^2\pi^3x^5 - 4K\pi^2x^3\right)\exp\left\{-\pi\lambda Kx^2\right\}. \end{aligned} \tag{57}$$

Our objective is to find the λ^* when $C^{M=1'}(\lambda^*) = 0$. Choose a threshold ε which is close to zero and an initial value λ_0. In our simulation, we set $\varepsilon = 10^{-6}$ and $\lambda_0 = 0$. Compute λ_1 according to

$$\lambda_{n+1} = \lambda_n - \frac{C^{M=1'}(\lambda_n)}{C^{M=1''}(\lambda_n)}, \tag{58}$$

and continue the iteration until $C^{M=1'}(\lambda_{n+1}) < \varepsilon$. Then we obtain the target BS density per storey $\lambda^* = \lambda_{n+1}$ and the minimum coverage probability $C^{M=1}(\lambda^*)$.

Acknowledgment

This project has received funding from the European Union Horizon 2020 research and innovation program under the Marie Sklodowska-Curie grant agreement No. 766231 WAVECOMBE H2020-MSCA-ITN-2017.

References

[1] J. G. Andrews *et al*., "What will 5G be?" *IEEE J. Sel. Areas Commun.*, vol. 32, no. 6, pp. 1065-1082, Jun. 2014.

[2] "Cisco visual networking index: global mobile data traffic forecast update, 2017-2022," Cisco, San Jose, CA, USA, White Paper, Feb. 2019.

[3] Huawei. (Feb. 2016). "Five trends to small cell 2020," [Online]. Available: http://www-file.huawei.com/~/media/CORPORATE/PDF/News/Five-Trends-To-Small-Cell-2020-en.pdf

[4] J. Zhang and G. d. l. Roche, "Femtocells: technologies and deployment," *John Wiley and Sons*, 2010.

[5] T. Nakamura *et al*., "Trends in small cell enhancements in LTE advanced," *IEEE Commun. Mag.,* vol. 51, no. 2, pp. 98-105, Feb. 2013.

[6] H. S. Dhillon, R. K. Ganti, F. Baccelli, and J. G. Andrews, "Modeling and analysis of K-tier downlink heterogeneous cellular networks," *IEEE J. Sel. Areas Commun.,* vol. 30, no. 3, pp. 550-560, Apr. 2012.

[7] T. Bai, R. Vaze, and R. W. Heath, "Analysis of blockage effects on urban cellular networks," *IEEE Trans. Wireless Commun.,* vol. 13, no. 9, pp. 5070-5083, Sep. 2014.

[8] A. Thornburg, T. Bai and R. W. Heath, "Performance analysis of outdoor mmWave ad hoc networks," *IEEE Trans. Signal Process.,* vol. 64, no. 15, pp. 4065-4079, Aug. 2016.

[9] B. Yang, G. Mao, M. Ding, X. Ge and X. Tao, "Dense small cell networks: from noise-limited to dense interference-limited," *IEEE Trans. Veh. Technol.,* vol. 67, no. 5, pp. 4262-4277, May. 2018.

[10] X. Wang, E. Turgut and M. C. Gursoy, "Coverage in downlink heterogeneous mmWave cellular networks with user-centric small cell deployment," *IEEE Trans. Veh. Technol.,* vol. 68, no. 4, pp. 3513-3533, Apr. 2019.

[11] J. Liu, M. Sheng and J. Li, "Improving network capacity scaling law in ultra-dense small cell networks," *IEEE Trans. Wireless Commun.,* vol. 17, no. 9, pp. 6218-6230, Sept. 2018.

[12] M. K. Muller, M. Taranetz, and M. Rupp, "Analyzing wireless indoor communications by blockage models," *IEEE Access*, vol. 5, pp. 2172-2186, 2017.

[13] S. Niknam, B. Natarajan and R. Barazideh, "Interference analysis for finite-area 5G mmWave networks considering blockage effect," *IEEE Access,* vol. 6, pp. 23470-23479, 2018.

[14] M. K. Müller, S. Schwarz and M. Rupp, "Investigation of area spectral efficiency in indoor wireless communications by blockage models," *International Symposium on Modeling and Optimization in Mobile, Ad Hoc, and Wireless Networks (WiOpt),* Shanghai, 2018, pp. 1-6.

[15] H. Zheng, J. Zhang, H. Li, Q. Hong, H. Hu and J. Zhang, "Exact line-of-sight probability for channel modeling in typical indoor environments," *IEEE Antennas Wireless Propag. Lett.,* vol. 17, no. 7, pp. 1359-1362, Jul. 2018.

[16] K. Venugopal and R. W. Heath, "Location based performance model for indoor mmWave wearable communication," *Proc. of International Conference on Communications (ICC)*, pp. 1-6, IEEE, 2016.

[17] R. Kovalchukov *et al.*, "Evaluating SIR in 3D millimeter-wave deployments: direct modeling and feasible approximations," *IEEE Trans. Wireless Commun.,* vol. 18, no. 2, pp. 879-896, Feb. 2019.

[18] J. G. Andrews, F. Baccelli, and R. K. Ganti, "A tractable approach to coverage and rate in cellular networks," *IEEE Trans. Commun.,* vol. 59, no. 11, pp. 3122-3134, Nov. 2011.

[19] T. Bai and R. W. Heath, Jr., "Coverage and rate analysis for millimeter-wave cellular networks," *IEEE Trans. Wireless Commun.*, vol. 14, no. 2, pp. 1100-1114, Feb. 2015.

[20] H. Jo, Y. J. Sang, P. Xia and J. G. Andrews, "Heterogeneous cellular networks with flexible cell association: a comprehensive downlink SINR analysis," *IEEE Trans. Wireless Commun.,* vol. 11, no. 10, pp. 3484-3495, Oct. 2012.

[21] H. Hu, J. Weng and J. Zhang, "Coverage performance analysis of FeICIC low-power subframes," *IEEE Trans. Wireless Commun.,* vol. 15, no. 8, pp. 5603-5614, Aug. 2016.

[22] H. Hu, Y. Gao, J. Zhang, X. Chu and J. Zhang, "Density analysis of LTE-LAA networks coexisting with WiFi sharing multiple unlicensed channels," *IEEE Access*, vol. 7, pp. 148004-148018, 2019.

[23] Z. Pan and Q. Zhu, "Modeling and analysis of coverage in 3-D cellular networks," *IEEE Commun. Lett.,* vol. 19, no. 5, pp. 831-834, May. 2015.

[24] A. K. Gupta, X. Zhang, and J. G. Andrews, "SINR and throughput scaling in ultradense urban cellular networks," *IEEE Wireless Commun. Lett.,* Aug. 2015.

[25] J. Lee, X. Zhang, and F. Baccelli, "A 3-D spatial model for in-building wireless networks with correlated shadowing," *IEEE Trans. Wireless Commun.,* vol. 15, no. 11, pp. 7778-7793, Nov. 2016.

[26] J. Liu, T. Kou, Q. Chen and H. D. Sherali, "Femtocell base station deployment in commercial buildings: a global optimization approach," *IEEE J. Sel. Areas Commun.,* vol. 30, no. 3, pp. 652-663, Apr. 2012.

[27] H.-Y. Hsieh, S.-E. Wei, and C.-P. Chien, "Optimizing small cell deployment in arbitrary wireless networks with minimum service rate constraints," *IEEE Trans. Mobile Comput.*, vol. 13, no. 8, pp. 1801-1815, Aug. 2014.

[28] M. Lin and T. L. Porta, "Energy-aware enterprise femtocell deployment," *2014 IEEE Wireless Communications and Networking Conference (WCNC)*, Istanbul, 2014, pp. 2312-2317.

[29] J. G. Andrews, X. Zhang, G. D. Durgin and A. K. Gupta, "Are we approaching the fundamental limits of wireless network densification?" *IEEE Commun. Mag.,* vol. 54, no. 10, pp. 184-190, Oct. 2016.

[30] J. Liu, M. Sheng, L. Liu and J. Li, "Network densification in 5G: from the short-range communications perspective," *IEEE Commun. Mag.,* vol. 55, no. 12, pp. 96-102, Dec. 2017.

[31] J. Liu, M. Sheng, L. Liu, and J. Li, "Effect of densification on cellular network performance with bounded pathloss model," *IEEE Commun. Lett.*, vol. 21, no. 2, pp. 346-349, Feb. 2017.

[32] M. Kamel, W. Hamouda and A. Youssef, "Ultra-dense networks: a survey," *IEEE Commun. Surveys Tut.,* vol. 18, no. 4, pp. 2522-2545, Fourthquarter 2016.

[33] M. Ding, P. Wang, D. López-Pérez, G. Mao, and Z. Lin, "Performance impact of LoS and NLoS transmissions in dense cellular networks," *IEEE Trans. Wireless Commun.,* vol. 15, no. 3, pp. 2365-2380, Mar. 2016.

[34] M. Ding and D. López-Pérez, "Performance impact of base station antenna heights in dense cellular networks," *IEEE Trans. Wireless Commun.,* vol. 16, no. 12, pp. 8147-8161, Dec. 2017.

[35] X. Zhang and J. G. Andrews, "Downlink cellular network analysis with multi-slope path loss models," *IEEE Trans. Commun.*, vol. 63, no. 5, pp. 1881-1894, May. 2015.

[36] ITU-R Recommendation P.1238-10, "Propagation data and prediction methods for the planning of indoor radio communication systems and radio local area networks in the frequency range 300 MHz to 450 GHz," 2019.

[37] J. Zhang, A. A. Glazunov and J. Zhang, "Wireless energy efficiency evaluation for buildings under design based on analysis of interference gain," *IEEE Trans. Veh. Tech.*, accepted for publication.

[38] J. Hygh, J. DeCarolis, D. Hill and R. Ranjithan, "Multivariate regression as anenergy assessment tool in early building design," *Build Environ*, vol. 57, pp. 165-175, 2012.

[39] M. Zhen, Y. Du, F. Hong and G. Bian, "Simulation analysis of natural lighting of residential buildings in Xi'an, China", *Sci Total Environ*, vol. 690, pp. 197-208, 2019.

[40] R. L. Burden and J. D. Faires, "Numerical analysis (3rd Ed.)," *PWS Publishers*, 1985.